Article:
Nicely, JM, Anderson, DC, Canty, TP et al. (34 more authors) (2016) An observationally constrained evaluation of the oxidative capacity in the tropical western Pacific troposphere. Journal of Geophysical Research: Atmospheres, 121 (12). pp. 7461-7488. ISSN 2169-897X

https://doi.org/10.1002/2016JD025067

An Observationally Constrained Evaluation of the Oxidative Capacity in the Tropical Western Pacific Troposphere

Julie M. Nicely[1,*], Daniel C. Anderson[1], Timothy P. Canty[1], Ross J. Salawitch[1], Glenn M. Wolfe[2,3], Eric C. Apel[4], Steve R. Arnold[5], Elliot L. Atlas[6], Nicola J. Blake[7], James F. Bresch[4], Teresa L. Campos[4], Russell R. Dickerson[1], Bryan Duncan[3], Louisa K. Emmons[4], Mathew J. Evans[8,9] , Rafael P. Fernandez[10,11], Johannes Flemming[12], Samuel R. Hall[4], Thomas F. Hanisco[3], Shawn B. Honomichl[4], Rebecca S. Hornbrook[4], Vincent Huijnen[13], Lisa Kaser[4], Douglas E. Kinnison[4], Jean-Francois Lamarque[4], Jingqiu Mao[14], Sarah A. Monks[5,**,***], Denise D. Montzka[4], Laura L. Pan[4], Daniel D. Riemer[6], Alfonso Saiz-Lopez[10], Stephen D. Steenrod[3,15], Meghan H. Stell[4,16], Simone Tilmes[4], Solene Turquety[17], Kirk Ullmann[4], Andrew J. Weinheimer[4]

1. University of Maryland, College Park, MD, USA.
2. University of Maryland Baltimore County, Baltimore, MD, USA.
3. NASA Goddard Space Flight Center, Atmospheric Chemistry and Dynamics Laboratory, Greenbelt, MD, USA.
4. National Center for Atmospheric Research, Boulder, CO, USA.
5. Institute for Climate and Atmospheric Science, University of Leeds, Leeds, UK.
6. University of Miami, Miami, FL, USA.
7. University of California, Irvine, CA, USA.
8. National Centre for Atmospheric Science, University of York, York, UK.
9. Department of Chemistry, University of York, York, UK.
10. Department of Atmospheric Chemistry and Climate, Institute of Physical Chemistry Rocasolano, CSIC, Madrid, Spain.
11. National Research Council (CONICET), Mendoza, Argentina.
12. European Centre for Medium-Range Weather Forecasts, Reading, UK.
13. Royal Netherlands Meteorological Institute, De Bilt, the Netherlands.
14. Princeton University, Princeton, NJ, USA.
15. Universities Space Research Association, Columbia, MD, USA.
16. Metropolitan State University of Denver, Denver, CO, USA.
17. Laboratoire de Météorologie Dynamique, IPSL, Sorbonne Universités, UPMC Univ Paris 06, Paris, France.

*now at: *NASA Goddard Space Flight Center, Atmospheric Chemistry and Dynamics Laboratory, Greenbelt, MD, USA.*
**now at: *Chemical Sciences Division, Earth System Research Laboratory, National Oceanic and Atmospheric Administration, Boulder, CO, USA.*
***now at: *Cooperative Institute for Research in Environmental Sciences, University of Colorado, Boulder, CO, USA*.

Key points:

- Observations from the CONTRAST campaign in the tropical Western Pacific are used to infer the concentration of tropospheric OH
- The empirically based value of tropospheric column OH is 0 to 20% larger than found within global models
- Underestimations of observed NO_x, CH_3CHO, & HCHO drive most differences between column OH within global models and empirically based value

Abstract

Hydroxyl radical (OH) is the main daytime oxidant in the troposphere and determines the atmospheric lifetimes of many compounds. We use aircraft measurements of O_3, H_2O, NO, and other species from the Convective Transport of Active Species in the Tropics (CONTRAST) field campaign, which occurred in the tropical western Pacific (TWP) during January–February 2014, to constrain a photochemical box model and estimate concentrations of OH throughout the troposphere. We find that tropospheric column OH (OH^{COL}) inferred from CONTRAST observations is 12 to 40% higher than found in chemical transport models (CTMs), including CAM-chem-SD run with 2014 meteorology as well as eight models that participated in POLMIP (2008 meteorology). Part of this discrepancy is due to a clear-sky sampling bias that affects CONTRAST observations; accounting for this bias and also for a small difference in chemical mechanism results in our empirically based value of OH^{COL} being 0 to 20% larger than found within global models. While these global models simulate observed O_3 reasonably well, they underestimate NO_x ($NO+NO_2$) by a factor of two, resulting in OH^{COL} ~30% lower than box model simulations constrained by observed NO. Underestimations by CTMs of observed CH_3CHO throughout the troposphere and of HCHO in the upper troposphere further contribute to differences between our constrained estimates of OH and those calculated by CTMs. Finally, our calculations do not support the prior suggestion of the existence of a tropospheric OH minimum in the TWP, because during January–February 2014 observed levels of O_3 and NO were considerably larger than previously reported values in the TWP.

1 Introduction

The hydroxyl radical (OH) is the most important oxidant in the troposphere. Abundances of many species, such as CH_4, CO, SO_2, and certain halocarbons are determined in part by the concentration of tropospheric OH. The lifetime of methane (CH_4), the second most important anthropogenic greenhouse gas, is primarily controlled by tropospheric OH [*Levy*, 1971; *Prather et al.*, 2012]. The geographic distribution of carbon monoxide (CO), a long-lived anthropogenic pollutant, in global chemistry models depends on the accuracy of tropospheric OH as well as CO emissions [*Levy,* 1971*; Shindell et al.*, 2006; *Monks et al.*, 2015; *Strode et al.*, 2015]. The lifetime of SO_2, a product of anthropogenic activities, is also sensitive to the concentration of OH [*Calvert et al.*, 1978]. Of the very short-lived (VSL) halocarbons, dibromomethane (CH_2Br_2), bromochloromethane (CH_2BrCl), and all chlorocarbons (CH_2Cl_2, $CHCl_3$, and higher order compounds) are lost predominantly by reaction with OH [*SPARC*, 2013]. Finally, the OH-initiated oxidation of volatile organic compounds (VOCs) is an important production mechanism for tropospheric ozone (O_3) [*Hough and Derwent*, 1987].

A primary motivation for improved understanding of tropical tropospheric OH arises from the considerable range in the global burden of OH that is estimated in global models. Concentrations of OH maximize near the surface in the tropical troposphere [*Spivakovsky et al.*, 2000], so the mean tropospheric abundance of OH and CH_4 lifetime within global models are largely influenced by the tropics [*Bloss et al.*, 2005]. The Atmospheric Chemistry and Climate Model Intercomparison Project (ACCMIP) analyzed 14 models and found a 62% spread (full range of values divided by the multi-model

98 mean) in global burdens of OH [*Voulgarakis et al.*, 2013]. Most of the models analyzed
99 were chemistry-climate models (CCMs), i.e., they were run using internally-generated
100 dynamics and atmospheric moisture. Other projects that compare output solely from
101 chemistry transport models (CTMs, in which model dynamics are based upon
102 meteorological reanalysis fields) might be expected to have better-constrained OH due to
103 the use of similar transport. Our analysis of one such project, the POLARCAT Model
104 Intercomparison Project (POLMIP) [*Emmons et al.*, 2015], suggests that the spread in
105 global mean OH across eight models is ~31%: a smaller range, but for fewer models (*J.*
106 *M. Nicely et al.*, manuscript in preparation). For POLMIP, effort was made to use the
107 same emissions of NO_x, CO, and VOCs among the various models, which also likely
108 explains the smaller range of OH in this CTM comparison. Other intercomparison
109 studies show large variations in computed OH: *Shindell et al.* [2006] reported a 65%
110 spread in global mean OH among 26 models and *Fiore et al.* [2009] found an 80% spread
111 among 12 models. Both of these studies examined OH from global models run as CTMs.
112 Furthermore, there is considerable spread in the computed difference in tropospheric
113 mean OH between pre-industrial and present, ranging from a 14% increase to a 14%
114 decrease, among 16 global models examined by *Naik et al.* [2013].

115 Considering these large spreads in OH burdens among various global models, it is
116 not surprising that models also disagree on the future evolution of OH concentrations.
117 *Voulgarakis et al.* [2013] found that the ACCMIP models do not agree on the sign of
118 change in the global burden of OH over the next century. Early estimates of the effect of
119 climate change on atmospheric chemistry predicted that global OH burdens would
120 decline with expected increases in global burdens of CH_4 and CO (e.g., *Houghton et al.*

121 [1996]). However, many facets of OH chemistry were simplified in these studies. It is
122 now believed that other factors, including increasing water vapor and NO_x [*Stevenson et*
123 *al.*, 2000; *Hauglustaine et al.*, 2005] as well as rising temperatures leading to faster CH_4
124 oxidation [*Johnson et al.*, 1999] could instead result in larger future burdens of OH
125 [*Stevenson et al.*, 2006]. Given that climate modelers seek to understand a wide range of
126 possible future conditions through consideration of many factors, the community should
127 define how well various models represent OH in the contemporary atmosphere as a first
128 step to assessing the reliability of projections of tropospheric OH.

129 Another issue confronting the modeling community is that global models [*Naik et*
130 *al.*, 2013] systematically underestimate τ_{CH4} by ~1.75 years (~16%) relative to the current
131 empirical best estimate of 11.2 years [*Prather et al.*, 2012; IPCC AR5, 2013]. Here and
132 throughout, we use τ_{CH4} to refer to the photochemical lifetime of CH_4 with respect to loss
133 by tropospheric OH. Measurements of methyl chloroform (MCF: CH_3CCl_3) decay rates
134 are most commonly used to empirically determine the mean tropospheric concentration
135 of OH as well as τ_{CH4} [*Singh*, 1977; *Prinn et al.*, 2005; *Montzka et al.*, 2011]. For
136 example, *Prinn et al*. [2005] reported τ_{CH4} of $10.2^{+0.9}_{-0.7}$ years in 2003 based on the
137 observed decay of MCF. More recently, *Prather et al.* [2012] reported a value for τ_{CH4} of
138 11.2 ± 1.3 years (uncertainty is one standard deviation (σ) confidence interval). The
139 *Prather et al.* [2012] analysis also included loss of CH_4 by soils, reactions in the
140 stratosphere, reaction with tropospheric atomic chlorine, as well as the reaction with
141 tropospheric OH, leading to an overall lifetime of 9.1 ± 0.9 years. The burden of
142 tropospheric OH from the ACCMIP CCMs and POLMIP CTMs discussed earlier yield
143 mean CH_4 lifetimes of 9.8 ± 1.6 [*Voulgarakis et al.*, 2013] and 8.1 ± 0.9 years (*J. M.*

144 *Nicely et al.*, manuscript in preparation), respectively, where the uncertainties are 1σ
145 about the multi-model mean. The discrepancy between MCF-based and model-based
146 estimates of τ_{CH4} could be resolved if the burden of tropospheric OH within global
147 models were shown to be too high, based on actual tropospheric abundances. Another
148 possible resolution to this discrepancy would be an error in the MCF-based estimate of
149 τ_{CH4}. *Krol and Lelieveld* [2003] pointed out that stockpiling and later release of MCF, as
150 the Montreal Protocol was being implemented, could lead to an uncertainty that during
151 the time of release of stockpiled MCF, if not considered, would lead to an overestimate of
152 τ_{CH4} via the MCF method and therefore could help resolve this discrepancy. *Wennberg et*
153 *al.* [2004] noted the importance of air-sea exchange of MCF, which during times of
154 oceanic release would similarly lead to an overestimate of τ_{CH4} by the MCF method.
155 Conversely, *Wang et al.* [2008] used three-dimensional model estimates of OH, together
156 with MCF abundance and emission data, to suggest the actual value of τ_{CH4} via the MCF
157 method is longer than found in other studies.

158 The short-lived, reactive nature of OH as well as its low mixing ratio (a fraction
159 of a part per trillion by volume, hereafter ppt) make OH a challenging compound to
160 measure accurately. As a result, observational constraints on OH are often restricted in
161 spatial and temporal coverage. In regions where air is convectively lofted to the
162 tropopause, such as the tropical Western Pacific (TWP) [*Newell and Gould-Stewart*,
163 1981; *Hatsushika and Yamazaki*, 2003; *Fueglistaler et al.*, 2004], quantification of the
164 abundance of OH is crucial to evaluating the composition of air at the base of the
165 stratosphere [*SPARC*, 2013]. Measurements of OH in the TWP are limited to several
166 campaigns, including the Pacific Exploratory Mission – Tropics B (PEM-Tropics B) [*Tan*

167 *et al.*, 2001], which sampled the upper troposphere over the Pacific in March–April 1999
168 but only skirted the warm pool region. Measurements of OH precursors from the
169 accompanying PEM-Tropics A campaign in September–October 1996 were also used to
170 calculate OH using a box model [*Olson et al.*, 2001]. The sampling from both PEM-
171 Tropics campaigns is representative of the pristine Southern Hemisphere Pacific and
172 relatively clean central Northern Hemisphere Pacific. Diurnally-averaged OH
173 concentrations from PEM-Tropics A and B maximize in the tropical lower troposphere,
174 peaking at a value of ~1.7×10^6 cm^{-3} [*Olson et al.*, 2001]. This peak value of OH is
175 similar to what we infer over the TWP warm pool. Similarly, the Mauna Loa
176 Observatory Photochemistry Experiment (MLOPEX 2) found that observations of free
177 tropospheric OH in the central Pacific at 10:00 AM during spring 1992 were ~4×10^6 cm^{-3}
178 [*Eisele et al.*, 1996], similar to values calculated in our study. The Transport and
179 Chemical Evolution over the Pacific (TRACE-P) campaign conducted measurements of
180 OH across the Pacific Ocean [*Jacob et al.*, 2003], though the only results noted for the
181 remote marine environment occurred at night [*Mauldin III et al.*, 2003]. The STRAT
182 campaign also provided observations of TWP OH when it sampled an upper tropospheric
183 air parcel under sunlit conditions near Hawaii that had originated from convective
184 outflow in the TWP. This air parcel had extremely low hydroxyl concentrations
185 (~0.5×10^6 cm^{-3}), which *Gao et al.* [2014] suggested could be indicative of the TWP
186 warm pool; the low number density of nitric oxide (i.e., [NO] < 1×10^8 cm^{-3}) suppressed
187 the normally rapid conversion of HO_2 to OH.

188 *Rex et al.* [2014] similarly found observational evidence of a marked OH
189 minimum throughout the TWP troposphere. In this case, the OH minimum was driven by

190 low mixing ratios of O_3 (< 15 ppb) measured by sondes during the TransBrom ship-based
191 campaign in October 2009 [*Kruger and Quack*, 2013]. Calculations conducted using the
192 GEOS-Chem model, which agreed well with the low O_3 measurements [*Ridder et al.*,
193 2012], resulted in low values of [OH] ($\leq 0.75\times10^6$ cm^{-3}) likely as a result of suppressed
194 primary production [*Rex et al.*, 2014]. While there are no direct measurements of OH in
195 the central region of the TWP, the suggestion of the existence of depressed OH as a result
196 of low concentrations of NO or O_3 (or a combination of these two factors), which *Rex et*
197 *al.* [2014] termed an "OH hole", motivates the need for increased observational
198 constraints to better quantify OH in the TWP.

199 The PEM-West A and B campaigns also provided measurements of many species
200 with the exception of OH in the TWP region for boreal autumn 1991 and spring 1994,
201 respectively [*Hoell et al.*, 1996; 1997]. Notably, during the springtime campaign,
202 bimodal distributions of NO_x and O_3 were observed frequently [*Crawford et al.*, 1997],
203 consistent with observations from the CONvective TRansport of Active Species in the
204 Tropics (CONTRAST) campaign [*Pan et al.*, 2015; *Anderson et al.*, 2016]. However, the
205 PEM-West B observations differ from CONTRAST observations in that elevated CO did
206 not accompany the high NO_x and O_3 measurements. As a result, *Crawford et al.* [1997]
207 attribute the elevated NO_x primarily to lightning occurring in conjunction with
208 continental deep convection. *Anderson et al*. [2016] finds high correlation of elevated O_3
209 with elevated tracers of biomass burning, so the higher values of NO_x presented here are
210 likely the result of burning activities over Africa and Southeast Asia in addition to
211 lightning NO_x generation. Data from the PEM-West A campaign in autumn, however,

showed primarily clean conditions corresponding to the low O_3, low NO_x regime that was sometimes present in the springtime campaign [*Crawford et al.*, 1997].

Very short-lived (VSL) halocarbons can contribute to O_3 loss in the lowermost stratosphere [*Salawitch et al*., 2005], a process facilitated by convective lofting in the TWP [*Aschmann et al.*, 2009; *Ashfold et al.*, 2012; *Hossaini et al.*, 2012; *Fernandez et al.*, 2014; *Liang et al.*, 2014]. We use the common convention that VSL refers to any species with a tropospheric lifetime of six months or less, such that the distribution within the troposphere is expected to be non-uniform [*Law et al.*, 2007]. With lifetimes on the order of days to months, the efficiency of these species passing into the stratosphere hinges on the concentration of OH in the TWP [*Rex et al*., 2014].

We use data collected during the CONTRAST aircraft campaign [*Pan et al.*, 2016], conducted during January and February 2014 from Guam (13.5°N, 144.8°E), to model the abundance of OH in the TWP. While OH was not observed during CONTRAST, a multitude of chemical species, radiative variables, and meteorological parameters needed to model the *in situ* production and loss of OH were measured. The DSMACC box model [*Emmerson and Evans*, 2009], constrained to observations of OH precursors and related species, is used to calculate instantaneous and 24-hour average OH. We then compare our results to values of OH computed by the CAM-chem-SD model, run in the specified dynamics mode for 2014 [*Lamarque et al.*, 2012; *Tilmes et al.*, 2015]. Additional box model runs were performed to determine which OH precursor species drive the differences between the modeled and observationally derived OH. We also assess the impact on OH of high-O_3, low-H_2O (HOLW) structures frequently observed in the mid-troposphere throughout CONTRAST [*Pan et al.*, 2015; *Anderson et*

235 *al.*, 2016]. Additionally, the local lifetime of CH_2Br_2 (τ_{CH2Br2}), a brominated VSL lost
236 primarily by reaction with OH, is evaluated and compared to previously published
237 estimates. Finally, we compare our observationally constrained OH distribution to output
238 from the POLMIP CTMs to highlight a few possible shortcomings in these global
239 models.

240

241 **2 Data and Methods**

242 **2.1 CONTRAST Campaign**

243 The CONTRAST campaign [*Pan et al.*, 2016] was based in Guam (13.5°N,
244 144.8°E) during January and February 2014. Observations were obtained by a suite of
245 chemical, meteorological, microphysical, and radiative instruments onboard the
246 NSF/NCAR Gulfstream V (GV) aircraft. The foci of various research flights (RFs)
247 consisted of either surveying the TWP, sampling convective outflow, or obtaining
248 observations across both the inter-tropical convergence zone as well as the subtropical jet
249 stream. Our study uses observations acquired over the portion of the TWP sampled
250 extensively during CONTRAST; i.e., the region bounded by latitudes 0°N to 20°N,
251 longitudes 132°E to 162°E (**Figure 1**). We further restrict our study to data collected
252 during times when measurements of O_3 and CO exist and solar zenith angle (SZA) < 60°
253 (i.e., mid-day or higher solar illumination). Within these constraints, we analyzed data
254 collected during the portions of RFs 04 to 15 that lie within the red box of Figure 1. Data
255 collected during the three transit flights (RF 01, 02, and 16) are excluded, as are data
256 collected during RF03 since measurements of CO are not available.

257 The CONTRAST measurements used in this study include O_3 and NO obtained
258 onboard the GV aircraft by chemiluminescence at a frequency of 1 Hz with 1σ precisions
259 of 0.5 ppb and 10 ppt, respectively, both with uncertainties of 5% [*Ridley and Grahek*,
260 1990]. CO measurements were obtained using an Aero-Laser 5002 vacuum ultraviolet
261 fluorescence instrument at a frequency of 1 Hz and with a 2σ uncertainty of 3 ppb ± 3%
262 [*Gerbig et al.*, 1999]. Water vapor mixing ratios were measured by an open-path laser
263 hygrometer at a frequency of 1 Hz and 2σ precision of < 3% [*Zondlo et al.*, 2010]. CH_4
264 measurements were made using a Picarro G2311-fm $CO_2/CH_4/H_2O$ cavity ring-down
265 spectrometer with output provided at 1 Hz with a 1σ precision of 3 ppb [*Crosson*, 2008].
266 Formaldehyde (HCHO) was measured via laser-induced fluorescence by the NASA *in*
267 *situ* airborne formaldehyde (ISAF) instrument with reported values at 1 Hz frequency and
268 2σ uncertainty of ± 20 ppt [*Cazorla et al.*, 2015]. A number of organic trace gas
269 measurements are used from the Trace Organic Gas Analyzer (TOGA) gas
270 chromatograph/mass spectrometer (GCMS) instrument [*Apel et al.*, 2015]. Acetone
271 (CH_3COCH_3), isoprene (C_5H_8), propane (C_3H_8), methanol (CH_3OH), and acetaldehyde
272 (CH_3CHO) were measured with a sampling time of 35 s and output every 2 min.
273 Additionally, HCHO from TOGA is sporadically used when data from ISAF are
274 unavailable. Limits of detection (uncertainties) for the TOGA species are: 20 ppt (20%
275 or 40 ppt) for CH_3COCH_3, 1 ppt (15% or 2 ppt) for C_5H_8, 10 ppt (30% or 20 ppt) for
276 C_3H_8, 20 ppt (30% or 40 ppt) for CH_3OH, 5 ppt (20% or 10 ppt) for CH_3CHO, and 20 ppt
277 (100% or 80 ppt) for HCHO. Finally, photolysis frequencies for the reactions:

278 $$O_3 + h\nu \rightarrow O_2 + O(^1D)$$ **R1**

279 $$NO_2 + h\nu \rightarrow NO + O(^3P)$$ **R2**

280 are provided every 6 s, calculated from measurements of up- and down-welling,
281 spectrally resolved actinic flux density by the HIAPER Airborne Radiation Package
282 (HARP) [*Shetter and Muller*, 1999]. Total 1σ uncertainties for the photolysis frequencies
283 of **R1** (hereafter denoted $J(O^1D)$) and **R2** (denoted $J(NO_2)$) are estimated to be 25% and
284 12%, respectively. These estimates account for calibration, instrumental, and spectral
285 (including cross section and quantum yield) uncertainties.

286 The data set described above was adapted to a variable time resolution for this
287 study because we conduct numerous box model simulations of observations collected
288 along each flight track. For level altitude flight legs a resolution of 10 min is used,
289 whereas a finer resolution of 30 s is implemented for aircraft ascent or descent. This
290 variable time resolution preserves fine-scale features, such as HOLW structures, often
291 observed within vertical profiles. Measurements are averaged (i.e., along either 30 sec or
292 10 min intervals) when valid data are present. This choice of variable temporal
293 resolution results in 2600 samples of atmospheric composition across the 12 flights.

294

295 **2.2 DSMACC Box Model**

296 We use the Dynamically Simple Model for Atmospheric Chemical Complexity
297 (DSMACC) to perform box model calculations of OH [*Emmerson and Evans*, 2009].
298 This box model uses the Kinetic PreProcessor (KPP) [*Damian et al.*, 2002], the
299 Tropospheric Ultraviolet and Visible radiation model version 4.2 (TUV) [*Palancar et al.*,
300 2011], and a subset (644 species; 2046 chemical reactions) of the Master Chemical
301 Mechanism (MCM) [*Jenkin et al.*, 1997; *Saunders et al.*, 2003] version 3.3 [*Jenkin et al.*,

2015]. The box model is constrained to CONTRAST measurements of meteorological variables, O_3, CO, NO, HCHO, H_2O, C_3H_8, CH_4, C_5H_8, CH_3COCH_3, CH_3OH, and CH_3CHO mixing ratios, as well as $J(O^1D)$ and $J(NO_2)$. Constraints for all non-radical chemical species (all chemicals listed above except NO) result in that variable being held fixed at the initial value for the duration of the model run. A box model simulation progresses through several solar cycles until diel steady state is achieved (i.e., the fractional change in concentrations of radical species from one solar cycle to the next is near zero). The sum of $NO+NO_2+NO_3+N_2O_5+HO_2NO_2+HONO$ is held constant throughout a simulated solar cycle, but the concentrations of the individual species vary with solar illumination. At the end of each solar cycle, each of the NO_y compounds listed above is scaled by the ratio of observed NO to modeled NO. This ensures that the total of the NO_y species in the model is internally self-consistent with the observed NO concentrations. Photolysis frequencies also vary diurnally. They are first calculated by the TUV module for the latitude, longitude, and pressure coordinates of the specific observation and for albedo (0.05) and overhead column O_3 (224 DU total column, 194 DU stratospheric column) values representative of the TWP for January/February. The photolysis frequencies are then scaled to the observed J-value at the time of observation via a multiplicative factor. This multiplicative factor is applied throughout the diurnal cycles simulated by the model. The J-values for other species are scaled according to a combination of the $J(NO_2)$ and $J(O^1D)$ scaling factors, determined by the wavelength range in which the species photolyze. The calculated J-values are insensitive to the chosen albedo and overhead column O_3 values chosen above due to subsequent scaling of the J-values to match the observations. Upon reaching diurnal steady state, the box

model outputs the final 24 hours (at 10 min intervals) of chemical concentrations, J-values, and reaction rates, enabling us to evaluate both instantaneous OH (at the time of observation) as well as 24-hour average OH.

For the analysis of OH during the CONTRAST campaign the box model is constrained to the 11 chemical measurements (noted above) obtained by instruments onboard the GV aircraft, plus $J(O^1D)$, $J(NO_2)$, temperature, pressure, latitude, longitude, and local solar time. These calculated OH values will hereafter be referred to as "GV OH". Additional box modeling calculations are performed, constrained to the output from the global models described below.

Given the variable temporal resolution of specific instruments, as well as occasional gaps due to instrument performance or routine calibrations, valid data are frequently unavailable. For example, only 311 of the aforementioned 2600 samples of atmospheric composition have valid measurements of all 13 GV parameters. To obtain a robust estimate of GV OH (i.e., representative of the mean state of the TWP during January and February 2014), we have developed a method to fill in missing data values. Given the importance and atmospheric variability of O_3, all atmospheric samples used here must include a valid measurement of O_3. For other species as well as $J(O^1D)$ and $J(NO_2)$, if missing data occur before measurements of a particular variable have been made (i.e., during the initial leg) or after an instrument has stopped sampling, missing data are filled in by averaging all other valid measurements that exist within 0.5° latitude, 0.5° longitude, and 2000 m altitude for the specific flight. This helps ensure that the substitute value is from a similar air mass sampled close in location to where missing data are reported. For missing data that occur when measurements exist both earlier and

later in the current flight, a value is found by linearly interpolating between the two closest valid data points. An exception is made for H_2O when altitude is varying; in these cases, gaps in the H_2O mixing ratio are either filled using the latitude/longitude/altitude binning method (if available) or the sampling interval is excluded from the analysis. For HCHO, we use measurements from the ISAF instrument whenever valid data points exist. When HCHO from ISAF is unavailable, observations from the TOGA instrument are used. In this case, regression of ISAF against TOGA HCHO is used on a flight-by-flight basis to account for instrument differences. The effect of this method for filling in missing data on our results is further examined in Section 3.2.

Because the GV aircraft was sampling in the remote TWP, the mixing ratios of the organic trace gases measured by TOGA used in this analysis (C_3H_8, C_5H_8, CH_3COCH_3, CH_3OH, CH_3CHO) were at times below the limit of detection (LOD) of the instrument. When the abundance of a compound was below the LOD, we specified abundance based on the number of "below LOD" data points reported in succession. Mixing ratio equal to 50% of the LOD was specified when fewer than 10 "below LOD" data points occurred in succession; conversely, a mixing ratio equal to 20% of the LOD was used when 10 or more "below LOD" data points occurred in succession. Isoprene (C_5H_8) is the species most commonly affected by the TOGA LOD. Our scientific results are unaffected by any reasonable assumption for $[C_5H_8]$ and the other organics when below the TOGA LOD, including specification of $[C_5H_8]=0$ within the model.

We have tagged each of the 13 GV variables, to assess for all 2600 samples whether and how data gaps were filled. The scientific results shown below are the same whether the analysis is based on the 300 sampling intervals when valid data exist for all

371 species, or the 2600 intervals considered below. We have chosen to show results for the
372 2600 intervals, since this provides more complete sampling of the TWP.

373

374 **2.3 CAM-chem-SD (Winter 2014)**

375 The Community Atmosphere Model version 4.0 (CAM4) is the atmospheric
376 component of the global chemistry-climate Community Earth System Model (CESM)
377 [*Lamarque et al.*, 2012; *Tilmes et al.*, 2015]. The model can be run with active
378 chemistry, a configuration referred to as CAM-chem. For the winter 2014 calculations
379 conducted for the CONTRAST campaign, the internally derived meteorological fields
380 were nudged using NASA GEOS5 analysis fields [*Tilmes et al.*, 2015] with a horizontal
381 resolution of 0.94° latitude × 1.25° longitude and 56 vertical levels, which we denote
382 CAM-chem-SD (SD for specified dynamics). The model chemistry scheme includes a
383 detailed representation of tropospheric and stratospheric chemistry (~180 species; ~500
384 chemical reactions), including brominated [*Fernandez et al.*, 2014] and iodinated [*Saiz-*
385 *Lopez et al.*, 2014] very short-lived organic compounds. Anthropogenic emissions of O_3
386 and aerosol precursors are from RCP 6.0 for year 2014 [*Meinshausen et al.*, 2011; *van*
387 *Vuuren et al.*, 2011], and biomass burning emissions are from the Fire INventory for
388 NCAR (FINN) [*Wiedinmyer et al.*, 2011].

389 Output from CAM-chem-SD includes all the species and variables used to
390 constrain and initialize the box model, as described in Section 2.2. The model output is
391 linearly interpolated to the aircraft latitude, longitude and local solar time for all flights in
392 the campaign, providing us with "curtains", or output at all model vertical levels along

393 the space/time coordinate of each research flight. The curtain file model output allows
394 for quantitative comparison of GV OH to CAM-chem-SD OH, for GV OH to be
395 visualized in the context of surrounding atmospheric features, and for the causes of
396 differences between GV OH and CAM-chem-SD OH to be assessed.

397 Variations between observationally-constrained box model OH and global model
398 OH may result from a number of factors, including differences in the chemical
399 mechanism within the two models. The importance of the chemical mechanism can be
400 assessed by examining whether the box model can reproduce CAM-chem-SD OH, when
401 constrained to the 13 precursor species output from CAM-chem-SD. We therefore
402 perform box model calculations of OH based on inputs from CAM-chem-SD for each
403 flight. Additionally, differences between GV OH and CAM-chem-SD OH may arise
404 from differences in the OH precursor fields. This effect is examined by performing
405 variable "swaps", in which the box model is constrained by OH precursor fields from
406 CAM-chem-SD except for a single input field taken instead from the GV observations.
407 The resulting difference in OH between the "all CAM-chem-SD" box model run and the
408 "all CAM-chem-SD + GV [variable]" run can then be ascribed to that precursor field. In
409 this work, swap runs are performed using GV O_3, H_2O, NO_x ($NO+NO_2$), CO, C_5H_8,
410 HCHO, CH_3CHO, $J(O^1D)$, and $J(NO_2)$. These swap runs are performed for all flights.

411 The differences between GV OH and CAM-chem-SD OH are further quantified
412 by calculating tropospheric column OH values. We integrate the 24-hour mean OH
413 number density ($[OH_{24\ HR}]$) vertical profile, averaged for all flights, for each simulation
414 of OH: GV OH, CAM-chem-SD OH (produced by the box model constrained to CAM-
415 chem-SD precursors), and the swaps of the nine variables listed above. We also perform

one additional simulation to examine the effect of a possible clear-sky sampling bias that occurred during aircraft sampling, discussed in Section 3.1. In this simulation, we constrained the box model to $J(NO_2)$ and $J(O^1D)$ from CAM-chem-SD and GV observations for all other inputs. Columns are based on an integration from the surface to 13 km to match the vertical extent of columns calculated for the POLMIP CTM swap simulations (see Section 3.3).

2.4 POLMIP CTMs (2008)

POLMIP was conducted to utilize the Polar Study using Aircraft, Remote Sensing, Surface Measurements and Models, of Climate, Chemistry, Aerosols, and Transport (POLARCAT) [*Law et al.*, 2014] suite of observations acquired in 2008 for the purpose of evaluating global chemistry models [*Emmons et al.*, 2015]. While the POLARCAT aircraft campaigns focused on the Arctic troposphere, POLMIP consists of global model simulations. These simulations were performed for January to December, 2008, using a common emissions inventory, with the exception of GEOS-Chem (see *Emmons et al.* [2015] for further detail). All participating models were run in CTM mode, meaning wind and temperature inputs are based on assimilated meteorological fields. Accordingly, meteorological variables are roughly consistent among the models. Each model was also run with its standard chemistry and deposition schemes. Models provided monthly mean output for many chemical, physical, and radiative variables, including OH. All models that provided a global field of OH – CAM4-chem [*Lamarque et al.,* 2012*; Tilmes et al.,* 2015], C-IFS [*Flemming et al.*, 2015], GEOS-Chem [*Bey et al.*,

2001; *Mao et al.*, 2010], GMI-GEOS5 [*Duncan et al.*, 2007; *Strahan et al.*, 2007], LMDZ-INCA [*Hauglustaine et al.*, 2004; *Hourdin et al.*, 2006], MOZART-4 [*Emmons et al.*, 2010], TM5 [*Huijnen et al.*, 2010; *Williams et al.*, 2013], and TOMCAT [*Chipperfield,* 2006] – are analyzed here. The POLMIP simulation of CAM4-chem does not include halogenated very short-lived organic chemistry, as is included in CAM-chem-SD.

The POLMIP project and the CONTRAST campaign focused on different years, 2008 and 2014, respectively. The Multivariate El Niño – Southern Oscillation (ENSO) Index for January/February 2008 was in a moderate negative phase while the same months in 2014 were neutral [*Wolter and Timlin*, 2011]. Hence, the westward shift of the Pacific warm pool in 2008 and associated changes in locations of active convection, biomass burning, and the northern subtropical jet stream could account for some of the differences between the POLMIP CTMs and CONTRAST observations. Variations in biomass burning, whether due to ENSO effects or other factors, could also account for differences in chemical species associated with fire emissions. However, fire count data obtained from the MODIS instrument on board the NASA Terra satellite indicate biomass burning magnitude and distribution were similar in 2008 and 2014 (**Figure S1**). Furthermore, differences between the POLMIP multi-model mean of OH precursors and CONTRAST observations of these species are nearly identical to the differences between CAM-chem-SD (2014 meteorology) and CONTRAST. By extending our analysis to the POLMIP simulations, we are able to assess the strengths and a few shortcomings of a suite of CTMs. Finally, POLMIP output is available for all 12 months, allowing us to

examine conditions in October, the month for which *Rex et al.* [2014] suggested extremely low values of OH would be present in the TWP.

2.5 CH_2Br_2 Lifetime

We use the 24-hour average values of OH output from the box model constrained by GV observations and by the CAM-chem-SD model run performed for CONTRAST, as well as monthly mean OH from the POLMIP models, to evaluate the tropospheric lifetime of CH_2Br_2. This VSL bromocarbon is lost nearly exclusively by reaction with tropospheric OH. Here we use:

$$k_{OH+CH2Br2} = 2.0\times10^{-12} \exp(-840/\mathrm{T})\ \mathrm{cm}^3\ \mathrm{s}^{-1} \quad \textbf{(1)}$$

for the rate constant of reaction between OH and CH_2Br_2 [*Sander et al.*, 2011] and the local lifetime (as a function of altitude) is found using:

$$\tau_{CH2Br2}(z) = \frac{1}{k_{OH+CH2Br2}(z)\times[OH(z)]} \quad \textbf{(2)}$$

where [OH] is the number density of OH (units cm^{-3}).

According to the WMO Scientific Assessment of Ozone Depletion [2011], the global tropospheric mean lifetime of CH_2Br_2 is 123 days. *Rex et al.* [2014] suggested τ_{CH2Br2} was ~188 days at 500 hPa in the TWP during October 2009, due to an OH minimum. We highlight the lifetime of CH_2Br_2 below in order to further compare to the results of *Rex et al.* [2014].

2.6 HOLW Structures

We also evaluate the impact of high-O_3, low-H_2O (HOLW) structures on OH concentrations in the TWP. Many air parcels exhibiting high O_3 (defined as $O_3 > 40$ ppb) and low relative humidity (RH < 20%) were observed in the mid-troposphere [*Pan et al.*, 2015; *Anderson et al.*, 2016]. Relative humidity is calculated from observed H_2O and temperature (T), with respect to liquid water for T > 0°C and with respect to ice for T < 0°C. Primary production of OH occurs via **R1** followed by:

$$O(^1D) + H_2O \rightarrow 2\ OH\ . \qquad \textbf{R3}$$

The presence of HOLW structures, therefore, leads to competing effects on [OH]; low H_2O tends to suppress [OH] while elevated O_3 drives production of $O(^1D)$ and OH. We use the box model to investigate the net effect on [OH] of HOLW structures and compare to the OH concentrations found in background conditions, defined here as $O_3 < 25$ ppb and RH > 70%.

3 Results and Discussion

3.1 GV and CAM-chem-SD OH, Research Flight 07

The GV run of the box model, in which all model inputs are taken directly from measurements made during CONTRAST, reveals OH mixing ratios that are generally higher than those calculated by the 2014 CAM-chem-SD simulation. **Figures 2a** and **2b**

499 show results from RF07, which occurred entirely within our latitude/longitude/SZA
500 thresholds, conducted extensive vertical profiling, and provided mostly uninterrupted
501 measurements of all chemical species and variables used to constrain the box model (see
502 figure 5 of *Pan et al.*, [2016]). Figure 2a shows GV OH values calculated by the box
503 model as circles over-plotted on a "curtain" of OH values from CAM-chem-SD, in time
504 and altitude. Figure 2b shows the correlation of GV OH against the OH value from
505 CAM-chem-SD, extracted for the altitude of the observation. Based on the mean ratio of
506 GV OH to CAM-chem-SD OH, CAM-chem-SD underestimates OH by about 60%.
507 Considerable spread about the 1:1 line (r^2 = 0.12, Figure 2b) shows the global model is
508 not able to represent the variability of box modeled OH along the aircraft flight track.

509 To understand whether differences between the chemical mechanisms within
510 DSMACC and CAM-chem-SD are contributing to the difference in OH shown in Figures
511 2a and 2b, we constrain the box model using inputs of OH precursors from CAM-chem-
512 SD. As shown in **Figures 2c** and **2d,** the box model using CAM-chem-SD inputs does a
513 much better job of matching CAM-chem-SD OH. The OH mixing ratios do not lie
514 perfectly along the 1:1 line, suggesting some differences in chemical mechanism may
515 exist. However, the respective values of OH exhibit strong correlation (r^2 = 0.92) and a
516 mean ratio of 1.03 ± 0.19, demonstrating the chemical mechanism does not drive the
517 differences in OH seen in Figures **2a** and **2b**. A similar analysis for RF11, which
518 sampled convective outflow to the south and southwest of Guam, is given in Supplement
519 (**Figure S2**). The results are very similar to those presented above for RF07.

520 Next we investigate each OH precursor using the box model "swap" method. Six
521 variables, O_3, H_2O, $J(O^1D)$, NO_x, HCHO and CH_3CHO, account for the majority of the

522 difference between GV and CAM-chem-SD OH for RF07. **Figure 3** shows box model
523 results for swaps of these six variables: i.e., the box model is constrained by the GV
524 observation of the stated variable while all other constraints are taken from CAM-chem-
525 SD. Any deviation in the scatter plot from the tight linear correlation shown in the "all
526 CAM-chem-SD" run (Figure 2d and grey points in Figure 3) results from differences in
527 the swapped variable. The farther the new OH distribution (red points) is from the grey
528 points, the larger the role of that variable in explaining the difference between GV and
529 CAM-chem-SD OH. Also, the mean ratio of box model to CAM-chem-SD OH reported
530 for each variable conveys the difference in OH resulting from the swap of the specified
531 variable. In order of largest to smallest absolute difference, relative to CAM-chem-SD
532 OH, we find that NO_x, $J(O^1D)$, H_2O, HCHO, O_3, and CH_3CHO drive the largest
533 variations in OH. The variables CO, C_5H_8, and $J(NO_2)$ do not have an appreciable effect
534 on the difference between GV and CAM-chem-SD OH (**Figure S3**).

535 **Figure 4** compares vertical profiles of NO_x, $J(O^1D)$, H_2O, HCHO, O_3, and
536 CH_3CHO measured by the GV on RF07 to profiles along the GV flight track calculated
537 using CAM-chem-SD. All panels represent mean and standard deviation of measured
538 (GV, black) or modeled (CAM-chem-SD, red) profiles, except the NO_x panel. Here, we
539 have added observed NO and modeled NO_2 found using the DSMACC model
540 constrained to observed NO, O_3, $J(NO_2)$, etc., to facilitate the evaluation of NO_x within
541 CAM-chem-SD.

542 The abundance of NO_x is the most important driver of differences in GV and
543 CAM-chem-SD OH. When the box model is constrained to observed NO, calculated OH
544 is 61% higher than CAM-chem-SD OH (Figure 3d). The profile of NO_x inferred from

545 observed NO on RF07 is significantly larger than CAM-chem-SD NO_x throughout the
546 troposphere (Figure 4d). As shown in Section 3.2, the difference between measured and
547 modeled NO_x is pervasive throughout the campaign. During CONTRAST,
548 measurements of NO_y and reservoir species that link NO_x to NO_y were not obtained. As
549 a result, it is not possible to ascertain whether the discrepancy between measured and
550 modeled NO_x shown in Figure 4d would be reflected in a similar discrepancy for NO_y.
551 Future observational campaigns in the TWP would benefit from observations of NO_y and
552 a suite of nitrogen reservoir species.

553 The box model swaps indicate $J(O^1D)$ has the second most important influence on
554 OH for RF07. The mean ratio of OH calculated using GV $J(O^1D)$ to OH from CAM-
555 chem-SD is 1.33 (Figure 3c). The distribution of OH found using $J(O^1D)$ from the GV
556 and all other variables from CAM-chem-SD shows a clear elevation relative to CAM-
557 chem-SD OH. Values of $J(O^1D)$ observed during RF07 exceed values within CAM-
558 chem-SD below ~8 km (Figure 4c). This difference is due to the tendency of the GV to
559 preferentially sample during clear-sky conditions: even though a primary goal of
560 CONTRAST was the sampling of the outflow of active convection, the GV generally
561 avoided flying either within or beneath active convection. This tendency for clear-sky
562 sampling is evaluated further in Section 3.2.

563 Differences in O_3 and H_2O, related to the precise geographical location of HOLW
564 structures in CAM-chem-SD, also drive the spread between GV and CAM-chem-SD OH
565 (Figures 3a and 3b). The location and vertical extent of HOLW structures are determined
566 by the interplay of biomass burning, long-range transport, and precipitation [*Anderson et*
567 *al.*, 2016]. Mean profiles of O_3 and H_2O from CAM-chem-SD agree well with mean

568 profiles from the GV for RF07, especially in the mid-troposphere around 3 to 5 km
569 (Figures 4a and b). However, the model does not reproduce fine structure in O_3 and H_2O
570 along this flight track, which is not surprising given CAM-chem-SD is a global model.
571 This structure results in scatter when comparing OH from CAM-chem-SD to
572 observations on a point-by-point basis (Figures 3a and 3b).

573 The remaining differences in OH for RF07, after accounting for the four variables
574 above, are almost entirely explained by formaldehyde (HCHO) and acetaldehyde
575 (CH_3CHO). Constraining the box model to observations of HCHO results in a 14%
576 increase above CAM-chem-SD OH (Figure 3e). While HCHO concentrations are
577 underestimated by CAM-chem-SD throughout the troposphere (Figure 4e), most of the
578 difference in OH resulting from the HCHO swap occurs in the upper troposphere, where
579 OH mixing ratios are lowest. At the highest altitudes of GV sampling (~14 km),
580 photolysis of HCHO constitutes one of the main sources of HO_x ($OH+HO_2$) [*Jaeglé et*
581 *al.*, 1998]. The larger concentrations of HCHO in the upper troposphere drive production
582 of more OH than is calculated by CAM-chem-SD. Constraining the box model to GV
583 CH_3CHO, on the other hand, results in an 8% decrease in OH (Figure 3f). CAM-chem-
584 SD drastically underestimates observed concentrations of CH_3CHO (Figure 4f).

585 The underestimation of CH_3CHO in global models is a long-standing problem
586 that could be due, in part, to the lack of oceanic emissions of this compound [*Millet et al.*,
587 2010; *Read et al.*, 2012]. None of the global models considered here represent oceanic
588 emission of CH_3CHO. The inclusion of oceanic emission of this compound in global
589 models has been shown to primarily effect abundances of CH_3CHO in the marine
590 boundary layer, due to its short lifetime [*Millet et al.*, 2010; *Read et al.*, 2012]. The

591 model underestimation of CH_3CHO throughout the troposphere shown in Figure 4f could
592 also be due to underestimated primary emissions by biomass burning or
593 misrepresentation of secondary production from the oxidation of VOC sources, such as
594 ethane (C_2H_6) and propane (C_3H_8) [*Millet et al.*, 2010; *Read et al.*, 2012].

595 In addition to the six OH precursors discussed above, observed values of CO,
596 C_5H_8, and $J(NO_2)$, were also analyzed using the box model swap method. These
597 variables exhibit little influence on modeled OH. Swaps for each of these variables for
598 RF07 show structures and correlations similar to the box model simulation constrained
599 only to inputs from CAM-chem-SD (Figure S3). When each observed OH precursor is
600 considered as a constraint in isolation, the sum of the effects on box modeled OH (as
601 examined through the mean ratio statistic) does not exactly match the effect on OH found
602 by constraining the box model to observations of all OH precursors simultaneously. The
603 chemical impacts of these variables on OH are coupled to some extent. The linear
604 combination of individual effects suggests an even larger increase in the ratio of GV OH
605 to CAM-chem-SD OH than is found by the simulation that considers simultaneous
606 variable swaps.

607 To put these results in context, we have evaluated the effect of measurement
608 uncertainties of OH precursors on the box model calculation of GV OH. Details are
609 shown in **Figure S4**. The 1σ uncertainty in GV OH found using a root sum of squares
610 propagation of measurement uncertainties in the OH precursors is ±14%. Uncertainty in
611 the measurement of NO is the largest single contributor, ±10%, to the total uncertainty.
612 This uncertainty is much smaller than the difference in GV and CAM-chem-SD OH
613 (Figure 2b), as well as the variability in OH mixing ratio driven by geophysically

614 plausible variations in the precursor fields. Consequently, the error bars used below are
615 based on standard deviation about the mean (i.e., when binning the data with respect to
616 altitude).

617

618 **3.2 GV and CAM-chem-SD OH, Campaign-wide Results**

619 Consideration of GV and CAM-chem-SD OH for all CONTRAST flights
620 produces results similar to those shown above for RF07. **Figure 5** shows scatter plots of
621 GV OH versus CAM-chem-SD OH (Figure 5a) as well as OH calculated by the box
622 model constrained to all precursors from CAM-chem-SD versus CAM-chem-SD OH
623 (Figure 5b). Figures 5c and 5d show corresponding plots, for [OH] in units of number
624 density. Results in this figure and those to follow are subject to the latitude, longitude
625 and SZA filter described in Section 2.1 (i.e., sunlit measurements in the TWP). **Figure 6**
626 compares vertical profiles of NO_x, $J(O^1D)$, H_2O, HCHO, O_3, and CH_3CHO measured by
627 the GV for the entire CONTRAST campaign, RFs 04-15, to profiles found using CAM-
628 chem-SD, sampled along the GV flight track. Finally, **Table 1** summarizes the effect of
629 variable swaps on tropospheric column OH (OH^{COL}) for the entire campaign. We have
630 chosen to tabulate OH^{COL} because this is the most important quantity for the oxidative
631 capacity of the tropical troposphere. Tropospheric column OH is integrated from the
632 surface to 13 km, because this is the altitude range extensively sampled by the GV
633 aircraft. The profile of $[OH_{24\ HR}]$ falls off between 13 km and the tropopause, so this
634 definition captures most of the oxidative capacity of the tropical troposphere.

635 The mean ratio of GV OH to CAM-chem-SD OH mixing ratio for the entire
636 campaign is 1.40 ± 0.58, indicating that OH constrained by the CONTRAST observations
637 is on average 40% higher than CAM-chem-SD OH (Figure 5a). We test the effect of
638 filling in missing data (Section 2.2) by restricting this analysis to GV OH calculated only
639 for the 311 data points where observations of all box model inputs are available (not
640 shown). The resulting mean ratio of GV OH to CAM-chem-SD OH is 1.52 ± 0.59,
641 suggesting that our findings are not influenced by our treatment of the data. Constraining
642 the box model to OH precursors from CAM-chem-SD results in a mean ratio of 1.03 ±
643 0.19 (Figure 5b). The comparison shown in Figure 5b demonstrates similarity of the
644 chemical mechanism for representation of tropospheric OH between DSMACC and
645 CAM-chem-SD. The most notable differences are at high OH mixing ratios, which occur
646 in the mid-troposphere.

647 It is important to also examine OH number density ([OH]). Even though many
648 studies of tropospheric OH rely on mixing ratio [e.g., *Brune et al.,* 1998; *Jaeglé et al.*,
649 1998; *Olson et al.*, 2004], the lifetime of species lost by reaction with OH is determined
650 by [OH]. Figure 5c shows the ratio of GV and CAM-chem-SD [OH] is slightly less than
651 found for the OH mixing ratio, because number density places a higher weight on
652 observations in the middle and lower troposphere. Constraining the box model to
653 precursors from CAM-chem-SD also results in a mean ratio of 1.03 ± 0.19 for [OH]
654 (Figure 5d). However, this ratio is weighted heavily toward the lowest values of [OH]
655 (between 1×10^6 and 5×10^6 cm^{-2}) due to more frequent aircraft sampling at high altitudes.
656 Recalculating this ratio using a binning approach (grey points, Figure 5d) places equal
657 weight on all values of [OH]. The ratio of the grey points is 1.13 ± 0.15, which is

658 consistent with the visual interpretation of Figure 5d. The slope of a linear fit forced to
659 go through the origin is 1.15 (we use this approach since negative OH is nonphysical).
660 We conclude the effect of differences between the DSMACC and CAM-chem-SD
661 chemical mechanisms on [OH] lies between 3% and 15%. In the POLMIP section, we
662 make an adjustment to the box model based on the 1.13 ratio, because this is the most
663 reliable measure of the difference in the chemical mechanism between DSMACC and
664 CAM-chem-SD.

665 The first two rows of Table 1 show that OH^{COL} based on the mean vertical profile
666 campaign-wide GV OH is 12% higher than OH^{COL} found using CAM-chem-SD inputs
667 within the box model. The other rows of Table 1 show the impact on OH^{COL} of the
668 various precursors. The first numerical entry shows OH^{COL} resulting from using the GV
669 measurement of the specific OH precursor within the box model, with all other precursors
670 based on CAM-chem-SD. The other numerical entry shows the ratio of OH^{COL} resulting
671 from the variable swap divided by 1.94×10^{12} cm^{-2}, the value of OH^{COL} from CAM-chem-
672 SD.

673 As noted above, the GV tended to sample in clear-sky conditions during
674 CONTRAST. This tendency accounts for nearly all of the difference between OH^{COL}
675 found using GV OH precursors and those from CAM-chem-SD. Use of $J(O^1D)$ and
676 $J(NO_2)$ from CAM-chem-SD, and all other precursors from GV, results in OH^{COL} =
677 1.92×10^{12} cm^{-2} (last entry, Table 1), which is nearly identical to OH^{COL} based on use of
678 precursors exclusively from CAM-chem-SD. Hence, OH^{COL} inferred from campaign-
679 wide sampling of the TWP is in remarkably good agreement with that of CAM-chem-SD.

680 Nonetheless, there are important differences for the various precursors that tend to cancel
681 out. Next, we examine the effect of individual precursors on OH^{COL}.

682 Vertical profiles of O_3, H_2O, $J(O^1D)$, NO_x, HCHO, and CH_3CHO for the entire
683 campaign compared to CAM-chem-SD (Figure 6) exhibit similar differences as shown
684 for RF07 (Figure 4). Measured and modeled profiles of O_3 agree very well throughout
685 the campaign (Figure 6a) even though a considerable portion of the scatter in Figure 5 is
686 due to O_3. CAM-chem-SD accurately represents the impact on O_3 of biomass burning
687 and transport processes on the synoptic scale. However, the model cannot be expected to
688 reproduce atmospheric O_3 on the convective scale, so structures in O_3 are offset in space
689 and time relative to aircraft observations. Use of GV O_3 results in a 6% increase of
690 OH^{COL} compared to the baseline simulation (all precursors from CAM-chem-SD).

691 The measured profile of H_2O throughout the campaign tends to be ~20% lower
692 than the profile of H_2O within CAM-chem-SD (Figure 6b), resulting in a 17% decrease in
693 OH^{COL} (Table 1) compared to the baseline. Relative humidity in the TWP exhibits a
694 bimodal distribution, with high RH (> 70%) characterizing air masses recently influenced
695 by local convection and low RH (< 20%) for aged air parcels [*Anderson et al.*, 2016].
696 The differences in H_2O shown in Figure 6b could either reflect the treatment of RH upon
697 detrainment from deep convection within CAM-chem-SD, or the representation of aged
698 air parcels. Regardless, substitution of GV O_3 and H_2O for CAM-chem-SD O_3 and H_2O
699 within the DSMACC box model results in only an 11% decline in OH^{COL}.

700 The measured profile of NO_x is more than a factor of two larger than found within
701 CAM-chem-SD (Figure 6d). Use of observed NO within the box model results in a 35%

rise in OH^{COL} relative to baseline. As shown in Section 3.3, the POLMIP CTMs also underestimate observed NO_x by a similar amount. A possible explanation is that emissions of NO_x from biomass burning regions are underestimated by the FINN emission inventory used to drive CAM-chem-SD. If so, the various emission inventories used to drive the POLMIP CTMs likely suffer from the same deficit. Additionally, lightning over Africa is responsible for a large source of NO_x in the upper troposphere that is likely transported to the TWP following the same pathway as biomass burning plumes [*Jacob et al.*, 1996; *Murray et al.*, 2013; *Anderson et al.*, 2016]. Also, NO_x is converted to peroxyacetyl nitrate (PAN) during transit from Africa and Southeast Asia to the TWP [*Singh and Hanst*, 1981]. Biomass burning plumes descend as they transit from Africa and Southeast Asia to the TWP [*Anderson et al.*, 2016]. As an air parcel descends, NO_x is regenerated upon thermal decomposition of PAN. The GV payload during CONTRAST only measured NO within the NO_y family, so it is not possible to assess whether the NO_x deficit within CAM-chem-SD (and the POLMIP CTMs) is due to speciation of reactive nitrogen compounds. The NO_x deficit is important to resolve because low NO_x is the largest driver of differences between GV OH and OH found by global models.

As noted for RF07, the campaign-wide mean vertical profile of acetaldehyde (CH_3CHO) within CAM-chem-SD is much lower than observed (Figure 6f). Analysis of the atmospheric budget of CH_3CHO indicates the deficit may result from missing oceanic sources [*Singh et al.*, 2003; *Singh et al.*, 2004; *Millet et al.*, 2010; *Read et al.*, 2012] and poor representation of primary and secondary production of CH_3CHO [*Millet et al.*, 2010; *Read et al.*, 2012] as noted previously. Use of observed CH_3CHO within the box model

results in a 9% decline in OH^{COL} relative to baseline, because this compound is a sink for OH. The effect on OH is largest in the lower troposphere. However, CH_3CHO is a source of HCHO [*Singh et al.*, 2004] and this may explain some of the under-prediction of HCHO by CAM-chem-SD. Constraining the calculation of OH^{COL} to observed HCHO results in a 4% rise. The production and loss processes of HCHO observed during CONTRAST will be published separately (*D. C. Anderson et al.*, manuscript in preparation).

The entries in Table 1 for CO and isoprene (C_5H_8) confirm, as found for RF07, that these two compounds have a small effect on differences between CAM-chem-SD and GV OH^{COL} in the TWP. Use of observed CO within the box model results in a 6% decline in OH^{COL} relative to baseline, while use of observed C_5H_8 causes a 1% increase in OH^{COL}. Although CAM-chem-SD significantly underestimates the observed mean vertical profile of CO (**Figure S5a**), the response of OH to this difference is small. The response of OH to differences in C_5H_8 is negligible due to the near-zero concentrations of the compound, evident in GV observations and CAM-chem-SD output (Figure S5b).

We now transition to analyzing 24-hour average OH values calculated as vertical profiles of the campaign-wide results. Vertical distributions of 24-hour average OH provide the context for interpreting our results in a manner that is meaningful for examining the oxidizing capacity of the troposphere. Our calculations of vertical, 24-hour mean GV OH and CAM-chem-SD indicate that the largest differences occur in the lower (below ~4 km) and upper (above ~10 km) troposphere (**Figure 7a**, **b**). Figure 7a shows 24-hour average mixing ratios of OH ($OH_{24\ HR}$), and Figure 7b shows 24-hour average [OH] ($[OH_{24\ HR}]$). We show both mixing ratio and number density for the

748 convenience of the atmospheric chemistry community, since both measures are
749 commonly used. Here, CAM-chem-SD $OH_{24\ HR}$ and $[OH_{24\ HR}]$ is based on the diel steady
750 state output of the DSMACC box model, constrained to OH precursors from CAM-chem-
751 SD, because 24-hour average OH was not available from CAM-chem-SD. We make no
752 attempt to adjust for the possible difference in chemical mechanism between DSMACC
753 and CAM-chem-SD. Since DSMACC overestimates daytime [OH] by 3 to 13%
754 compared to CAM-chem-SD (Figure 5d), it is possible that CAM-chem-SD $[OH_{24\ HR}]$ is
755 1.5 to 6.5% higher than actual 24-hour average OH from CAM-chem-SD (because values
756 of daytime [OH] are roughly twice values of $[OH_{24\ HR}]$). This difference is smaller than
757 the standard deviation about the mean of the various profiles.

758 Figure 7b shows that most of the 12% difference in OH^{COL} between GV and
759 CAM-chem-SD is due to the tendency for $[OH_{24\ HR}]$ from GV to exceed that from CAM-
760 chem-SD below ~5 km. This $[OH_{24\ HR}]$ difference at low altitudes is primarily a result of
761 the observation of much higher levels of NO_x than found by CAM-chem-SD (Figure 6d).
762 The tendency for $J(O^1D)$ from the GV to exceed that within CAM-chem-SD (Figure 6c)
763 also contributes to the low altitude difference. The good agreement between GV and
764 CAM-chem-SD $[OH_{24\ HR}]$ in the mid-troposphere occurs despite the CAM-chem-SD
765 underestimation of NO_x; the effects of underestimated H_2O compensate by decreasing
766 OH in the 5 to 10 km range. Interestingly, as detailed in the Supplement (**Figure S6**), we
767 calculate less $OH_{24\ HR}$ within high O_3/low H_2O (HOLW) structures relative to
768 background between 3 and 10 km, because low H_2O (suppresses primary production of
769 HO_x) has a larger effect on $OH_{24\ HR}$ than the combination of high O_3 (increases primary
770 production of HO_x) and elevated NO_x (increases secondary production OH). While this

771 is true in the mid-troposphere, the effect of HOLW structures on OH above ~10 km
772 switches to increase radical concentrations over background. This occurs with a sharp
773 increase in concentrations of NO_x (Figure S6b).

774 *Crawford et al.* [1997] also noted a sharp increase in NO_x at ~10 km in the TWP
775 during the PEM-West B campaign (February and March 1994), where maximum
776 concentrations of NO_x of ~70 ppt were observed at the highest sampled altitude bin of 8-
777 10 km. Concentrations of NO_x from CONTRAST reach values nearly double the value
778 from *Crawford et al.* [1997]. We attribute enhanced NO_x in the HOLW structures to
779 tropical biomass burning [*Anderson et al.*, 2016], whereas *Crawford et al.* [1997]
780 concluded that lightning was the primary source of enhanced NO_x. Increases in biomass
781 burning between 1994 and 2014 may explain the differences in NO_x between these two
782 studies.

783 Figure 7a shows considerable differences in $OH_{24\ HR}$ mixing ratio in the upper
784 troposphere. As expected, the upper troposphere exhibits smaller absolute differences for
785 $[OH_{24\ HR}]$ (Figure 7b) and makes only a small contribution to OH^{COL}. This upper
786 tropospheric difference is a result of the observation of considerably higher levels of
787 HCHO (Figure 6e) and NO_x (Figure 6d) compared to CAM-chem-SD. The upper
788 troposphere is extremely important, even though there is a small effect on OH^{COL},
789 because energetic convection in the TWP often detrains at this level (e.g., figure 9 of *Pan*
790 *et al.* [2016]).

791 Figure 7c shows vertical profiles of τ_{CH2Br2} found using equation (2) as well as the
792 value for τ_{CH2Br2} at 500 hPa (~5.3 km) of 188 days given by *Rex et al.* [2014]. We also

793 show values of $OH_{24\,HR}$ mixing ratio (Figure 7a) and [$OH_{24\,HR}$] (Figure 7b) at this vertical
794 level from *Rex et al.* [2014]. The values from *Rex et al.* [2014] are based on model
795 calculations and ozonesonde observations in the TWP conducted during October 2009.
796 In Section 3.3, we show comparisons to POLMIP results for October 2008.

797 *Rex et al.* [2014] suggested the occurrence of very low OH in the TWP (black
798 circle in Figure 7a, b) was driven by mixing ratios of O_3 lying close to zero and well
799 below 20 ppbv, based on ozonesonde observations and supported by output from GEOS-
800 Chem [*Ridder et al.*, 2012]. *Newton et al*. [2016] focused on details of ozonesonde
801 calibration as a possible explanation for the near-zero levels of O_3 reported by *Rex et al*.
802 [2014]. However, it is unclear why GEOS-Chem v8-02-04, used by *Ridder et al.*,
803 demonstrates good agreement with the ozonesonde measurements. Calculations of
804 tropospheric O_3 columns from the v9-01-03 simulation of GEOS-Chem conducted for
805 POLMIP, as well as tropospheric column O_3 from the other POLMIP CTMs, do not
806 support the values of <15 DU of this quantity from GEOS-Chem near Guam shown by
807 *Rex et al.* [2014] (**Figure S7a**). The one exception is the TOMCAT model, which
808 reaches tropospheric O_3 column values of ~13.5 DU in the months of August and
809 September near Guam. One change implemented in the version of GEOS-Chem used in
810 our study is improved treatment of the yield of isoprene nitrates in the isoprene oxidation
811 mechanism [*Mao et al.,* 2013a]. The downward revision of the isoprene nitrate yield
812 results in an increase in the ozone production efficiency, which could be responsible for a
813 small part of the difference for O_3 in the TWP found here, compared to the GEOS-Chem
814 results of *Ridder et al.* and *Rex et al*. The GEOS-Chem group maintains a benchmark of
815 model output for year 2005 found using various versions of this model. As shown in

816 **Figure S7b**, tropospheric column O_3 in the TWP during October 2005 is quite similar for
817 v8-02-04 and v9-01-03 of GEOS-Chem. All of these values are much higher than
818 tropospheric column O_3 in the TWP during October 2008 reported by *Ridder et al.* and
819 *Rex et al*.

820 Another explanation for low OH in the TWP offered by *Gao et al.* [2014] and *Rex*
821 *et al.* [2014] is very small abundance of NO_x. Low NO_x can suppress OH, as HO_x tends
822 to preferentially exist as HO_2 rather than OH under this condition. However,
823 concentrations of NO observed during CONTRAST rarely reached the extremely low
824 values reported by *Gao et al.* [2014] and noted by *Rex et al.* [2014] (CONTRAST [NO]
825 was less than 1×10^8 cm^{-3} only 3.5% of the time for the altitude range 9 to 15 km; **Figure**
826 **S8**).

827 The GV observations of OH precursors suggest the lifetime of CH_2Br_2 at 500 hPa
828 (~5.3 km) is ~66 days, nearly a factor of three lower than the *Rex et al.* [2014] estimate of
829 ~188 days. Consequently, loss of CH_2Br_2 could occur in the middle troposphere for air
830 masses that detrain at this level. Observations of the vertical profile of CH_2Br_2 observed
831 by the TOGA instrument show a slight local minimum in the middle troposphere,
832 possibly suggesting local photochemical loss (**Figure S9**). However, the lifetime of
833 CH_2Br_2 based on CONTRAST observations rises to ~200 days at 10 km and exceeds 400
834 days above 14 km, due to the falloff of [$OH_{24\ HR}$] (Figure 7). Since convection driven by
835 the TWP warm pool often detrains above 10 km, significant injection of CH_2Br_2 to the
836 lowermost stratosphere is expected, as was observed during the NASA Airborne Tropical
837 Tropopause Experiment campaign [*Navarro et al.*, 2015].

838

839 **3.3 Comparison to POLMIP models**

840 We extend our analysis of OH in the TWP to the POLMIP simulations, since
841 output from these CTMs is available for all 12 months. These comparisons allow us to
842 examine conditions in October, the month for which *Rex et al.* [2014] suggested
843 extremely low values of OH would be present in the TWP. The POLMIP runs used
844 meteorology and emissions for 2008 and the archive consists of monthly mean fields
845 [*Emmons et al.*, 2015]. As detailed below, conclusions drawn from the POLMIP
846 comparisons are consistent with the findings based on the comparison to CAM-chem-SD
847 run for winter 2014 (Sections 3.1 and 3.2).

848 **Figures 8** and **9** show comparisons of POLMIP monthly mean OH mixing ratio,
849 OH number density ([OH]), as well as OH precursors and related species to 24-hour
850 average values of these quantities inferred from GV measurements during CONTRAST.
851 The top row of Figures 8 and 9 show results from individual CTMs, whereas the bottom
852 row shows results from the POLMIP multi-model mean (POL MMM). All POLMIP
853 results shown in these two figures use the average of January and February 2008 monthly
854 means for all model output that lies within the TWP boundary region shown in Figure 1;
855 i.e., the 2008 POLMIP archive is sampled at the same season and location as the
856 CONTRAST campaign. The vertical coordinate of pressure is used because the POLMIP
857 archive only provided output on a pressure grid. For the diurnally varying quantities OH,
858 NO_x, $J(O^1D)$, and $J(NO_2)$, the 24-hour average value from CONTRAST are campaign-
859 wide averages of the 24-hour average output of DSMACC box model runs constrained to

860 aircraft observations, whereas for HCHO the estimate of 24-hour average value is based
861 on scaling factors from the University of Washington Chemical Model (UWCM) model
862 [*Wolfe and Thornton*, 2011] in which HCHO concentrations vary diurnally (which is not
863 the case for the DSMACC box model). Additionally, POLMIP values of isoprene (C_5H_8)
864 are represented in Figure 8e as the median C_5H_8 concentrations from the individual
865 models, and in Figure 8j as the multi-model mean of those median values. This is done
866 to prevent the non-Gaussian distribution of C_5H_8 concentrations, influenced by transport
867 of air with high C_5H_8 from nearby landmasses, from exerting an artificial high bias.

868 The profiles of monthly mean OH in the TWP for boreal winter 2008 from the
869 individual POLMIP models (Figures 8a and b) all lie below the campaign wide GV-based
870 $OH_{24\ HR}$ profile, from the surface to ~500 hPa (about 5 km). There is considerable
871 variation in monthly mean OH in the TWP among the POLMIP models, which is
872 consistent with the results of other model intercomparison studies [*Shindell et al.*, 2006;
873 *Fiore et al.*, 2009; *Voulgarakis et al.*, 2013]. We also show the *Rex et al.* [2014] estimate
874 of $OH_{24\ HR}$ mixing ratio and [$OH_{24\ HR}$] at 500 hPa (circle, Figures 8a, b, f, and g), even
875 though this estimate is for October 2009 (later, we compare POLMIP output for October
876 2008 to these *Rex et al.* [2014] estimates). The OH profile for winter 2008 from the
877 LMDZ-INCA CTM is in close agreement with OH from *Rex et al.* [2014] due to low
878 NO_x, O_3, and $J(O^1D)$ (Figures 8c, 9a, and 9c); all other CTMs calculate OH considerably
879 higher than the *Rex et al.* [2014] value.

880 The comparison of OH precursors and related species from the POLMIP archive
881 (winter 2008) to GV observations reveals similar tendencies as found for CAM-chem-SD
882 (winter 2014, Section 3.2) (Figures 8c to 8e; Figures 9a to 9e). Observed mixing ratios of

883 NO_x (Figure 8c) and HCHO (Figure 8d) between the surface and 500 hPa are much larger
884 than found in any of the POLMIP CTMs, similar to the discrepancy between the GV
885 observations and output of CAM-chem-SD (Section 3.2). There is considerable spread in
886 the profile of O_3 among the CTMs (Figure 9a). For most of the troposphere the observed
887 profile of O_3 lies within the distribution of CTM profiles; however, between 100 and 200
888 hPa, observed O_3 is consistently lower than all of the CTM values. The lowest values of
889 O_3 for much of the TWP troposphere are reported by LMDZ-INCA, which is consistent
890 with the small values of OH from this CTM. Similarly, the observed profile of H_2O is
891 within the range of CTM values for altitudes below ~200 hPa (Figure 9b). Between 100
892 and 200 hPa, observed H_2O is consistently higher than all of the CTM values. These
893 comparisons suggest that the mean state of O_3 and H_2O in the TWP, from the surface to
894 ~200 hPa, is represented well within most of the POLMIP CTMs. The comparisons of
895 O_3 and H_2O between 100 and 200 hPa suggest a stronger influence of active convection
896 (with O_3-deficient, H_2O-saturated air) in the TWP during January and February 2014 than
897 simulated by the POLMIP CTMs for winter 2008.

898 We examine the effect of OH precursor differences between CONTRAST and the
899 POLMIP CTMs by performing box model swap simulations, as were performed with
900 CAM-chem-SD (described in Section 2.3). The multi-model mean of each monthly OH
901 precursor (O_3, H_2O, CO, C_5H_8, HCHO, CH_3CHO, NO_x, $J(O^1D)$, and $J(NO_2)$) are input
902 individually to the DSMACC box model, which is otherwise constrained to GV
903 observations. As in Figure 8j, C_5H_8 is calculated as the median value within the POLMIP
904 models rather than the mean. Scaling factors are applied to those species with significant
905 diurnal variations. Since this configuration of the DSMACC box model requires

906 constraints be specified at a specific local solar time, the monthly mean values of
907 POLMIP HCHO, NO_x, $J(O^1D)$, and $J(NO_2)$ have been scaled to represent values for local
908 solar noon. Scaling factors for NO, $J(O^1D)$, and $J(NO_2)$ are derived from all GV box
909 model runs for observations that occurred within one hour of local solar noon and are
910 calculated as $[NO]_{INST}/[NO]_{24\ HR}$, $[J(O^1D)]_{INST}/[J(O^1D)]_{24\ HR}$, and $[J(NO_2)]_{INST}/[J(NO_2)]_{24}$
911 $_{HR}$, respectively. All scaling factors are averaged within 100 hPa pressure bins and
912 applied to the likewise pressure-binned POLMIP multi-model mean, for input to the box
913 model. Because calculation of these scaling factors relies on the availability of GV
914 observations that occurred close to noon, column integration is restricted to 1000 to 200
915 hPa (i.e. only this pressure range was sampled at enough times to allow empirical scaling
916 factors to be found). **Figures S10-12**, respectively, show the NO, $J(O^1D)$, and $J(NO_2)$
917 scaling factors calculated by the box model as well as scaling factors calculated from
918 hourly output of the POLMIP CTMs, noted in the caption, that provided fields of each
919 species. This latter comparison provides confidence our method of scaling monthly mean
920 concentrations to instantaneous noontime values is handled correctly.

921 The scaling factor for HCHO is calculated from the same output of the UWCM
922 model used to generate 24-hour average values of HCHO shown in Figures 8d and 8i.
923 The same method is used to calculate the scaling factor, $[HCHO]_{INST}/[HCHO]_{24\ HR}$, but
924 for all measurements that occurred within two hours of solar noon, due to the coarser
925 time resolution of the UWCM box model run. The HCHO scaling factor is shown in
926 **Figure S13**.

927 The difference between the OH resulting from individual variable swaps and OH
928 calculated from the baseline run of the DSMACC box model, constrained only to GV

observations, **Figure 10a**, shows that NO_x is the dominant factor driving large negative differences in [$OH_{24\ HR}$] (negative indicates the POLMIP precursor is responsible for a low value of CTM OH), particularly for pressures greater than ~400 hPa. The highest values of observed NO_x in the mid-troposphere during CONTRAST coincide with HOLW structures [*Anderson et al.*, 2016]. **Figure 11c** shows NO_x values calculated from observed NO and modeled steady-state NO_2, separated by our categorization of HOLW and background conditions (Section 2.6). Figures 11a and 11b show the bimodal distributions of O_3 and H_2O, respectively, observed during CONTRAST. Previous work suggests the source of these HOLW structures is biomass burning emissions from Africa and Southeast Asia [*Anderson et al.*, 2016]. It is interesting that the monthly mean values of both O_3 and H_2O from POLMIP fall in between the extremes of the respective modes related to background conditions in the remote Pacific (solid black lines) and biomass burning structures (dotted black lines), whereas NO_x from most POLMIP CTMs lies close to that of the background TWP. Therefore, as noted in Section 3.2, the underestimates of NO_x by the POLMIP CTMs is likely related to model treatment of nitrogen emissions, chemistry and/or transport from distant landmasses.

Both $J(O^1D)$ and $J(NO_2)$ contribute to the tendency for lower values of [$OH_{24\ HR}$] within POLMIP CTMs compared to GV OH, with $J(O^1D)$ driving the larger differences (Figure 10a). The most significant influence of $J(NO_2)$ on [$OH_{24\ HR}$] occurs at low altitudes. As noted above, this finding results from the predominantly clear-sky sampling during CONTRAST. Ozone and H_2O from the POLMIP models also drive large differences in [$OH_{24\ HR}$]. The changes in [$OH_{24\ HR}$] derived from POLMIP H_2O fluctuate and are generally centered about zero, while those due to POLMIP O_3 account for a high

952 tendency in POLMIP OH. Indeed, multi-model mean O_3 found for the POLMIP CTMs is
953 higher than the mean O_3 vertical profile from CONTRAST (Figure 9f), though the
954 individual CTMs are either close to or spread about the observations except at the lowest
955 and pressures (Figure 9a). The tendency of POLMIP CTMs to overestimate observed O_3
956 for pressures below 200 hPa could be indicative of convection within the models
957 stopping at higher pressure (lower altitude) than in the actual TWP troposphere.
958 Alternatively, the coarse vertical resolution of the models in the upper troposphere/lower
959 stratosphere region could result in diffusion of more O_3-rich stratospheric air into the
960 modeled upper troposphere than is realistic.

961 The OH precursors HCHO and CH_3CHO also influence [$OH_{24\ HR}$] (Figure 10a) in
962 a manner similar to that seen for the CAM-chem-SD comparison. Use of HCHO from
963 the POLMIP CTMs within the box model causes a decrease in [$OH_{24\ HR}$] at lower
964 pressures (≤ ~200 hPa), where HCHO is an important source of HO_x [*Jaeglé et al.*, 1998].
965 Conversely, constraining to the lower abundance of CH_3CHO from POLMIP causes an
966 increase in OH near the ocean surface. As for CAM-chem-SD, oceanic emissions of
967 CH_3CHO are absent from all POLMIP CTMs. This factor, possibly in combination with
968 the other potential model misrepresentations of CH_3CHO production (Section 3.1),
969 results in an enormous gap between observed and modeled profiles of CH_3CHO (**Figure**
970 **12**). This comparison is shown using a linear scale (Figure 12a) to properly represent the
971 difference between observed and modeled CH_3CHO, and a logarithmic scale (Figure 12b)
972 so that differences in CH_3CHO between the various POLMIP CTMs can be visualized.
973 Since CH_3CHO is a sink for OH, the addition of an ocean source within CTMs will lower
974 OH in the marine boundary layer [*Read et al.*, 2012].

975 Carbon monoxide exhibits a small effect on [$OH_{24\ HR}$] despite considerable
976 differences in CO among the POLMIP models (Figure 9e) and the tendency of the
977 POLMIP multi-model mean value of CO to be 10 to 15% lower than CONTRAST CO
978 throughout the troposphere (Figure 9j). Many modeling studies have identified and
979 sought to understand low biases in model CO (e.g. [*Shindell et al.*, 2006; *Mao et al.*,
980 2013b; *Naik et al.*, 2013; *Monks et al.*, 2015; *Strode et al.*, 2015]), with explanations
981 ranging from underestimated CO from fossil fuel and biomass burning in emissions
982 inventories [*Shindell et al.*, 2006] to overestimated OH (the main sink for CO) in the
983 northern hemisphere [*Strode et al.*, 2015]. Whatever the cause, underestimation of the
984 CO sink in the POLMIP CTMs leads to a small positive perturbation in [$OH_{24\ HR}$], much
985 less in magnitude than the perturbations due to NO_x, $J(O^1D)$, and CH_3CHO.

986 Finally, C_5H_8 drives near-zero differences in [$OH_{24\ HR}$] throughout the
987 troposphere. Isoprene in the mid- to upper troposphere, at pressures lower than ~800
988 hPa, was almost always below the detection limit of the TOGA instrument (1 ppt). This
989 is not surprising, given the remote region of the observations and the short lifetime of
990 C_5H_8.

991 One additional box model simulation is performed in which all nine POLMIP OH
992 precursors (O_3, H_2O, CO, C_5H_8, HCHO, CH_3CHO, NO_x, $J(O^1D)$, and $J(NO_2)$) are
993 simultaneously used as constraints. The difference in [$OH_{24\ HR}$] between the baseline run
994 of the box model, constrained only to CONTRAST observations of the precursors, and
995 this simulation ($\Delta[OH_{24\ HR}]$) is nearly identical to the sum of the [$OH_{24\ HR}$] differences
996 due to each species from Figure 10a (**Figure S14**). The total $\Delta[OH_{24\ HR}]$ is added to the
997 campaign-wide [$OH_{24\ HR}$] vertical profile to determine whether these nine factors

describe the difference between GV and POLMIP OH. The result of this analysis (solid green line, Figure 10b) generally matches the OH from the POLMIP MMM (red line) in the upper troposphere, though values in the low to mid-troposphere overestimate those from POLMIP. Subsequently, τ_{CH2Br2} derived from these [$OH_{24\ HR}$] values shows that switching to box model constraint of the nine POLMIP OH precursors matches the POLMIP τ_{CH2Br2} values in the upper troposphere (solid green line, Figure 10c) but underestimates τ_{CH2Br2} in the lower and mid-troposphere. However, recall from Section 3.2 that the box model chemical mechanism could contribute a difference in calculated [$OH_{24\ HR}$] as high as 6.5%. When adjusted to account for this difference, our simulations agree quite well with values of [$OH_{24\ HR}$] and τ_{CH2Br2} from the POLMIP MMM (dashed green lines, Figures 10b and 10c). We infer from this result that the offset in OH driven by the box model chemical mechanism is consistent when compared to both CAM-chem-SD and the POLMIP suite of CTMs.

We also tabulate quantitative analysis of OH^{COL} values modeled by replacing, individually, GV observations of OH precursors with POLMIP multi-model mean (MMM) values. Values of OH^{COL} for each simulation are shown in **Table 2**. Overall, the GV-based value of OH^{COL} is 41% larger than the POLMIP MMM value OH^{COL}. The analysis shows that use of NO_x from observations results in a 28% increase in OH^{COL}, due to the increase in secondary production of OH. Observed fields of $J(O^1D)$ and $J(NO_2)$ result in 11% and 4% increases, respectively, in OH^{COL} relative to the POLMIP OH^{COL}. This supports the conclusion that primarily clear-sky sampling during CONTRAST leads to a ~15% overestimate of OH^{COL}. Acetaldehyde is the next important individual precursor; use of the observed profile results in a 9% underestimate

1021 of OH^{COL}, since the observed concentrations of CH_3CHO act as a fairly strong OH sink.
1022 All of the other precursors make minor contributions to the difference between GV and
1023 POLMIP OH^{COL}. If we attribute 15% of the 41% difference in these two quantities to the
1024 clear-sky sampling bias of CONTRAST, and another 6.5% to the tendency of the
1025 DSMACC chemical mechanism to overestimate OH relative to the mechanisms within
1026 global models, then we conclude that precursor conditions in the TWP observed during
1027 January and February 2014 led to OH^{COL} being ~20% larger than the POLMIP MMM
1028 value for January and February 2008.

1029 Finally, we use the POLMIP archive to determine the extent to which seasonal
1030 differences in OH precursors could explain the difference between inferred OH from the
1031 CONTRAST campaign and from *Rex et al.* [2014]. We compare values of $OH_{24\ HR}$
1032 calculated for the CONTRAST campaign for January–February 2014, $OH_{24\ HR}$ simulated
1033 by GEOS-Chem in *Rex et al.* [2014] for October 2009, and monthly mean OH mixing
1034 ratios simulated by the POLMIP models for each month in 2008, all at 500 hPa (**Figure**
1035 **13**). At this pressure level, for the corresponding months, no POLMIP model simulates
1036 mean TWP $OH_{24\ HR}$ as high as our estimate; nor does any model simulate a mean $OH_{24\ HR}$
1037 as low as the *Rex et al.* [2014] value. None of the POLMIP CTMs exhibit seasonal
1038 variation in OH or O_3 anywhere close to that which would be necessary to explain both
1039 the GV and *Rex et al.* [2014] based values. Both the box model-based estimate of OH_{24}
1040 $_{HR}$ and the *Rex et al.* [2014] CTM-based estimate of $OH_{24\ HR}$ are grounded in observations
1041 of O_3 (along with other chemical species and radiative variables, for our estimate). As
1042 discussed in Section 3.2, the ozonesonde data collected during the TransBrom cruise in
1043 *Rex et al.* [2014] may exhibit a low bias as a result of calibration technique [*Newton et*

1044 *al.*, 2016]; their reported O_3 mixing ratios often fell below 15 ppb as indicated by the
1045 shaded region in Figure 13b. None of the POLMIP CTMs produce values of O_3 as low as
1046 those reported by *Rex et al.* [2014]. On the other hand, the campaign-wide mixing ratio
1047 of O_3 at 500 hPa from CONTRAST lies in the middle of the range of O_3 from the
1048 POLMIP CTMs.

1049 Interannual variations in tropospheric composition may play a role in explaining
1050 the large discrepancy in $OH_{24\ HR}$ reported here compared to that of *Rex et al.* [2014].
1051 Biomass burning differences between the *Rex et al.* [2014] study period (October 2009)
1052 and that of CONTRAST (January/February 2014) are large (Figures S1a and c). The
1053 number of fires per month in Africa, north of the equator, for October 2009 is only ~8%
1054 of that observed by MODIS for January/February 2014. This difference is a result of
1055 seasonal shifts in the location of biomass burning. This shift should, however, be
1056 represented within the POLMIP CTMs (albeit, for one year after the *Rex et al.* [2014]
1057 cruise). Differences in the ENSO conditions between 2008 and 2014 must also be
1058 considered. The Multivariate ENSO Index for CONTRAST during January/February
1059 2014 was neutral, whereas the *Rex et al.* [2014] study took place during a moderately
1060 strong El Niño event at the end of 2009 [*Wolter and Timlin*, 2011]. The expected ENSO-
1061 induced changes in O_3 are counter to what we would expect to explain this discrepancy.
1062 Suppressed convection in the TWP during an El Niño event would enable O_3 to build to
1063 higher concentrations than normal [*Ziemke et al.*, 2010]. Furthermore, increased
1064 stratosphere-to-troposphere exchange following an El Niño event should increase O_3 in
1065 the upper troposphere [*Zeng and Pyle*, 2009]. However, *Rex et al.* [2014] observed much
1066 lower O_3 during October 2009 than we observed during the neutral ENSO conditions in

2014. Hence, interannual effects most commonly associated with tropospheric composition do not readily explain the differences in observed O_3 and calculated $OH_{24\ HR}$ between *Rex et al.* [2014] and this study.

4 Conclusions

Box model calculations of OH were performed for the CONTRAST campaign that occurred in the TWP during January–February 2014 using the NSF/NCAR GV aircraft. The DSMACC box model was constrained to measurements of O_3, CO, NO, HCHO, H_2O, C_3H_8, CH_4, C_5H_8, CH_3COCH_3, CH_3OH, CH_3CHO, $J(O^1D)$, and $J(NO_2)$. Comparisons and additional box model simulations were conducted to understand the differences between the measurement-inferred GV OH and OH from CAM-chem-SD and POLMIP CTM simulations.

We find that OH^{COL} calculated by the CAM-chem-SD model using 2014 meteorology agrees remarkably well – to within 1% – with OH^{COL} inferred from the GV observations after accounting for the tendency to sample clear-sky conditions during the CONTRAST campaign. However, compensating factors lead to this good agreement. A 26% low bias in CAM-chem-SD OH^{COL} results from underestimates in NO_x throughout the troposphere, relative to observations. Additionally, CAM-chem-SD overestimates OH^{COL} by 10% due to underestimated CH_3CHO in the lower troposphere, overestimates OH^{COL} by 6% due to underestimated CO throughout the troposphere, and underestimates OH^{COL} by 4% due to underestimated HCHO. Variations in OH^{COL} due to O_3 and H_2O arise from differences in the precise geographical location of high O_3/low H_2O (HOLW) structures [*Pan et al.*, 2015; *Anderson et al.*, 2016], which cannot be perfectly reproduced by global models.

An analysis of chemical fields within the POLMIP CTM archive (using 2008 meteorology) [*Emmons et al.*, 2015] and GV OH revealed observationally based GV

1092 OH^{COL} was 40% larger than the POLMIP multi-model mean. About 15% of this
1093 difference was attributed to a clear-sky sampling bias of the CONTRAST GV, and
1094 another 6.5% may be due to the tendency of the DSMACC chemical mechanism to report
1095 higher levels of OH than found within CAM-chem-SD. As a result, differences in
1096 precursor fields lead to GV OH^{COL} being ~20% larger than the POLMIP multi-model
1097 mean value. As with the CAM-chem-SD analysis, NO_x is the single most important
1098 precursor field for OH. Observed NO_x was nearly a factor of two larger than found
1099 within POLMIP CTMs for the middle and lower troposphere, resulting in higher levels of
1100 OH when constrained to GV observations due to secondary production of OH. All of the
1101 POLMIP CTMs severely underestimate the observed profile of acetaldehyde (CH_3CHO),
1102 due either to the neglect of ocean emission of this compound or a misrepresentation of
1103 either primary or secondary atmospheric production. Consistent with the analysis of
1104 tropical ground-based observations from Cape Verde [*Read et al.,* 2012], we show the
1105 improvement of model representation of CH_3CHO will likely suppress OH in the lower
1106 troposphere, due to the highly reactive nature of this compound.

1107 We find no evidence for suppressed levels of OH in the TWP. Mean values of
1108 $[OH_{24\ HR}]$ remain above 2×10^6 cm^{-3} (mixing ratio of ~0.1 ppt) throughout the TWP
1109 troposphere. Our measurements of O_3 reached a minimum of ~20 ppb and, as a result,
1110 the primary production of HO_x was not anomalously low in the TWP. A possible
1111 explanation for the marked difference in $[OH_{24\ HR}]$ at the 500 hPa level of the TWP
1112 reported here and that given by *Rex et al.* [2014] is that the O_3 mixing ratio minimum of
1113 *Rex et al.* [2014] was biased low, due to their ozonesonde calibration procedure [*Newton*
1114 *et al.*, 2016]. Finally, the extremely low concentrations of NO tied to the TWP by *Gao et*

1115 *al.* [2014] were rarely observed during CONTRAST. Rather, the abundance of NO_x
1116 inferred from CONTRAST NO was more than a factor of 2 higher than found within
1117 either CAM-chem-SD or the POLMIP CTMs, perhaps due to improper representation of
1118 outflow from regions of active biomass burning [*Anderson et al.*, 2016] in these global
1119 models. The high levels of NO observed in the tropical troposphere during CONTRAST
1120 sustain larger values of OH than found within global models, due to the recycling of HO_2.

1121 While this new observationally constrained estimate of OH may help global
1122 models that run active chemistry evaluate their simulations of OH, it should be noted that
1123 our study does not resolve a present dilemma regarding the oxidative capacity of the
1124 troposphere. The majority of global models calculate values of τ_{CH4} about 1.75 years
1125 smaller [*Naik et al.*, 2013] than the current best empirical estimate of τ_{CH4} (11.2 ± 1.3
1126 years, due to loss by reaction with tropospheric OH only) [*Prather et al.*, 2012]. If our
1127 finding that [OH] within global models is too low due to an underestimate of observed
1128 NO_x happens to hold for other regions of the tropics, then the discrepancy between τ_{CH4}
1129 found by global models and that inferred from measurements of CH_3CCl_3 could grow.
1130 However, our results are representative of a small region of the globe. While they are
1131 positioned within the crucial tropical band, they may not be representative of global
1132 model calculations of OH. The planned airborne measurements of OH, NO_x, NO_y, H_2O,
1133 CH_4, O_3, HCHO, actinic flux, and many other species of interest by the upcoming NASA
1134 Atmospheric Tomography Mission (ATom) over numerous tropical oceanic regions
1135 [*NOAA*, 2014] will shed important new light on the oxidative capacity of the tropical
1136 troposphere.

1137

Acknowledgements

We thank T. Robinson and O. Shieh for providing meteorology forecasts in the field and the pilots and crew of the CONTRAST Gulfstream V aircraft for their dedication and professionalism. We thank the three anonymous reviewers for constructive comments that improved this manuscript. CONTRAST was funded by the National Science Foundation. We would like to acknowledge high-performance computing support from Yellowstone (ark:/85065/d7wd3xhc) provided by NCAR's Computational and Information Systems Laboratory. The National Center for Atmospheric Research is sponsored by the National Science Foundation. Work conducted at the University of Maryland was supported, in part, by the NASA Modeling and Analysis Program. G.M.W., D.C.A., and T.F.H. received support for the NASA Upper Atmospheric Research Program under NNH12ZDA001N-UACO. CONTRAST data are publicly available for all researchers and can be obtained at http://data.eol.ucar.edu/master_list/?project=CONTRAST. The CAM-Chem-SD and POLMIP model simulations are available upon request to the authors (julie.m.nicely@nasa.gov).

1154 **References**

1155 Anderson, D., et al. (2016), A Pervasive Role for Biomass Burning in Tropical High
1156 Ozone/Low Water Structures, *Nature Commun.*, *7*, doi:10.1038/ncomms10267

1157 Apel, E. C., et al. (2015), Upper tropospheric ozone production from lightning NO_x-
1158 impacted convection: Smoke ingestion case study from the DC3 campaign, *J.*
1159 *Geophys. Res.*, *120*(6), 2505-2523, doi:10.1002/2014jd022121.

1160 Aschmann, J., B. M. Sinnhuber, E. L. Atlas, and S. M. Schauffler (2009), Modeling the
1161 transport of very short-lived substances into the tropical upper troposphere and lower
1162 stratosphere, *Atmos. Chem. Phys.*, *9*(23), 9237-9247, doi:10.5194/acp-9-9237-2009.

1163 Ashfold, M. J., N. R. P. Harris, E. L. Atlas, A. J. Manning, and J. A. Pyle (2012),
1164 Transport of short-lived species into the Tropical Tropopause Layer, *Atmos. Chem.*
1165 *Phys.*, *12*(14), 6309-6322, doi:10.5194/acp-12-6309-2012.

1166 Bey, I., et al. (2001), Global modeling of tropospheric chemistry with assimilated
1167 meteorology: model description and evaluation, *J. Geophys. Res.*, *106*, 23073–23095,
1168 doi:10.1029/2001JD000807.

1169 Bloss, W. J., M. J. Evans, R. Sommariva, D. E. Heard, and M. J. Pilling (2005), The
1170 oxidative capacity of the troposphere: Coupling of field measurements of OH and a
1171 global chemistry transport model, *Faraday Discuss.*, *130*, 425-436,
1172 doi:10.1039/B419090D.

1173 Brune, W. H., et al. (1998), Airborne in-situ OH and HO_2 observations in the cloud-free
1174 troposphere and lower stratosphere during SUCCESS, *Geophys. Res. Lett.*, *25*(10),
1175 1701-1704, doi:10.1029/97GL03098.

1176 Calvert, J. G., F. Su, J. W. Bottenheim, and O. P. Strausz (1978), Mechanism of
1177 homogeneous oxidation of sulfur-dioxide in troposphere, *Atmos. Environ.*, *12*(1-3),
1178 197-226, doi:10.1016/0004-6981(78)90201-9.

1179 Cazorla, M., G. M. Wolfe, S. A. Bailey, A. K. Swanson, H. L. Arkinson, and T. F.
1180 Hanisco (2015), A new airborne laser-induced fluorescence instrument for in situ
1181 detection of formaldehyde throughout the troposphere and lower stratosphere, *Atmos.*
1182 *Meas. Tech.*, *8*(2), 541-552, doi:10.5194/amt-8-541-2015.

1183 Chipperfield, M. P. (2006), New version of the TOMCAT/SLIMCAT off-line chemical
1184 transport model: intercomparison of stratospheric tracer experiments, *Q. J. Roy.*
1185 *Meteor. Soc.*, *132*, 1179–1203, doi:10.1256/qj.05.51.

1186 Crawford, J. H., et al. (1997), Implications of large scale shifts in tropospheric NO_x levels
1187 in the remote tropical Pacific, *J. Geophys. Res.*, *102*(D23), 28447-28468, doi:
1188 10.1029/97JD00011.

1189 Crosson, E. R. (2008), A cavity ring-down analyzer for measuring atmospheric levels of
1190 methane, carbon dioxide, and water vapor, *Appl. Phys. B-Lasers O.*, *92*(3), 403-408,
1191 doi:10.1007/s00340-008-3135-y.

1192 Damian, V., A. Sandu, M. Damian, F. Potra, and G. R. Carmichael (2002), The Kinetic
1193 PreProcessor KPP–A Software Environment for Solving Chemical Kinetics, *Comput.*
1194 *Chem. Eng.*, *26*(11), 1567-1579, doi:10.1016/S0098-1354(02)00128-X.

1195 Duncan, B. N., S. E. Strahan, Y. Yoshida, S. D. Steenrod, and N. Livesey (2007), Model
1196 study of the cross-tropopause transport of biomass burning pollution, *Atmos. Chem.*
1197 *Phys.*, *7*, 3713–3736, doi:10.5194/acp-7-3713-2007.

1198 Eisele, F. L., D. J. Tanner, C. A. Cantrell, and J. G. Calvert (1996), Measurements and
1199 steady state calculations of OH concentrations at Mauna Loa Observatory, *J.*
1200 *Geophys. Res.*, *101*(D9), 14665-14679, doi: 10.1029/95JD03654.

1201 Emmerson, K. M., and M. J. Evans (2009), Comparison of tropospheric gas-phase
1202 chemistry schemes for use within global models, *Atmos. Chem. Phys.*, *9*(5), 1831-
1203 1845, doi:10.5194/acp-9-1831-2009.

1204 Emmons, L. K., et al. (2010), Description and evaluation of the Model for Ozone and
1205 Related chemical Tracers, version 4 (MOZART-4), *Geosci. Model Dev.*, *3*, 43–67,
1206 doi:10.5194/gmd-3-43-2010.

1207 Emmons, L. K., et al. (2015), The POLARCAT Model Intercomparison Project
1208 (POLMIP): overview and evaluation with observations, *Atmos. Chem. Phys.*, *15*(12),
1209 6721-6744, doi:10.5194/acp-15-6721-2015.

1210 Fernandez, R. P., R. J. Salawitch, D. E. Kinnison, J.-F. Lamarque, and A. Saiz-Lopez
1211 (2014), Bromine partitioning in the tropical tropopause layer: implications for
1212 stratospheric injection, *Atmos. Chem. Phys.*, *14*(24), 13391-13410, doi:10.5194/acp-
1213 14-13391-2014.

1214 Fiore, A. M., et al. (2009), Multimodel estimates of intercontinental source-receptor
1215 relationships for ozone pollution, *J. Geophys. Res.*, *114*(D4),
1216 doi:10.1029/2008jd010816.

1217 Flemming, J., et al. (2015), Tropospheric chemistry in the Integrated Forecasting System
1218 of ECMWF, *Geosci. Model Dev.*, *8*, 975-1003, doi:10.5194/gmd-8-975-2015.

1219 Fueglistaler, S., H. Wernli, and T. Peter (2004), Tropical troposphere-to-stratosphere
1220 transport inferred from trajectory calculations, *J. Geophys. Res.*, *109*(D3),
1221 doi:10.1029/2003jd004069.

1222 Gao, R. S., K. H. Rosenlof, D. W. Fahey, P. O. Wennberg, E. J. Hintsa, and T. F. Hanisco
1223 (2014), OH in the tropical upper troposphere and its relationships to solar radiation
1224 and reactive nitrogen, *J. Atmos. Chem.*, *71*(1), 55-64, doi:10.1007/s10874-014-9280-
1225 2.

1226 Gerbig, C., S. Schmitgen, D. Kley, A. Volz-Thomas, K. Dewey, and D. Haaks (1999),
1227 An improved fast-response vacuum-UV resonance fluorescence CO instrument, *J.*
1228 *Geophys. Res.*, *104*(D1), 1699-1704, doi:10.1029/1998jd100031.

1229 Hatsushika, H., and K. Yamazaki (2003), Stratospheric drain over Indonesia and
1230 dehydration within the tropical tropopause layer diagnosed by air parcel trajectories,
1231 *J. Geophys. Res.*, *108*(D19), doi:10.1029/2002jd002986.

1232 Hauglustaine, D. A., F. Hourdin, L. Jourdain, M.-A. Filiberti, S. Walters, J.-F. Lamarque,
1233 and E. A. Holland (2004), Interactive chemistry in the Laboratoire de Météorologie
1234 Dynamique general circulation model: description and background tropospheric
1235 chemistry evaluation, *J. Geophys. Res.*, *109*, D04314, doi:10.1029/2003JD003957.

1236 Hauglustaine, D. A., J. Lathiere, S. Szopa, and G. A. Folberth (2005), Future tropospheric
1237 ozone simulated with a climate-chemistry-biosphere model, *Geophys. Res. Lett.*,
1238 *32*(24), L24807, doi:10.1029/2005gl024031.

1239 Hoell, J. M., D. D. Davis, S. C. Liu, R. Newell, M. Shipham, H. Akimoto, R. J. McNeal,
1240 R. J. Bendura, and J. W. Drewry (1996), Pacific Exploratory Mission-West A (PEM-
1241 West A): September-October 1991, *J. Geophys. Res.*, *101*(D1), 1641-1653, doi:
1242 10.1029/95JD00622.

1243 Hoell, J. M., D. D. Davis, S. C. Liu, R. Newell, H. Akimoto, R. J. McNeal, and R. J.
1244 Bendura (1997), The Pacific Exploratory Mission-West Phase B: February-March,
1245 1994, *J. Geophys. Res.*, *102*(D23), 28223-28239, doi: 10.1029/97JD02581.

1246 Hossaini, R., M. P. Chipperfield, W. Feng, T. J. Breider, E. Atlas, S. A. Montzka, B. R.
1247 Miller, F. Moore, and J. Elkins (2012), The contribution of natural and anthropogenic
1248 very short-lived species to stratospheric bromine, *Atmos. Chem. Phys.*, *12*(1), 371-
1249 380, doi:10.5194/acp-12-371-2012.

1250 Hough, A. M., and R. G. Derwent (1987), Computer modeling studies of the distribution
1251 of photochemical ozone production between different hydrocarbons, *Atmos. Environ.*,
1252 *21*(9), 2015-2033, doi: 10.1016/0004-6981(87)90163-6.

1253 Houghton, J. T., et al., and (Eds.) (1996), Climate Change 1995. The science of climate
1254 change, *Cambridge University Press, UK*, 572.

1255 Hourdin, F., et al. (2006), The LMDZ4 general circulation model: climate performance
1256 and sensitivity to parametrized physics with emphasis on tropical convection, *Clim.*
1257 *Dynam.*, *27*, 787–813, doi:10.1007/s00382- 006-0158-0.

1258 Huijnen, V., et al. (2010), The global chemistry transport model TM5: description and
1259 evaluation of the tropospheric chemistry version 3.0, *Geosci. Model Dev.*, *3*, 445–
1260 473, doi:10.5194/gmd-3-445-2010.

1261 IPCC (2013), Climate Change 2013: The Physical Science Basis. Contribution of
1262 Working Group I to the Fifth Assessment Report of the Intergovernmental Panel on

1263 Climate Change, 1535 pp, Cambridge University Press, Cambridge, United Kingdom
1264 and New York, NY, USA.

1265 Jacob, D. J., et al. (1996), Origin of ozone and NO_x in the tropical troposphere: A
1266 photochemical analysis of aircraft observations over the South Atlantic basin, *J.*
1267 *Geophys. Res.*, *101*(D19), 24235-24250, doi:10.1029/96jd00336.

1268 Jacob, D. J., J. H. Crawford, M. M. Kleb, V. S. Connors, R. J. Bendura, J. L. Raper, G.
1269 W. Sachse, J. C. Gille, L. Emmons, and C. L. Heald (2003), Transport and Chemical
1270 Evolution over the Pacific (TRACE-P) aircraft mission: Design, execution, and first
1271 results, *J. Geophys. Res.*, *108*(D20), 9000, doi: 10.1029/2002JD003276.

1272 Jaeglé, L., D. J. Jacob, W. H. Brune, D. Tan, I. C. Faloona, A. J. Weinheimer, B. A.
1273 Ridley, T. L. Campos, and G. W. Sachse (1998), Sources of HO_x and production of
1274 ozone in the upper troposphere over the United States, *Geophys. Res. Lett.*, *25*(10),
1275 1709-1712, doi:10.1029/98GL00041.

1276 Jenkin, M. E., S. M. Saunders, and M. J. Pilling (1997), The tropospheric degradation of
1277 volatile organic compounds: A protocol for mechanism development, *Atmos.*
1278 *Environ.*, *31*(1), 81-104, doi:10.1016/s1352-2310(96)00105-7.

1279 Jenkin, M. E., J. C. Young, and A. R. Rickard (2015), The MCM v3.3 degradation
1280 scheme for isoprene, *Atmos. Chem. Phys. Discuss.*, *15*(6), 9709-9766,
1281 doi:10.5194/acpd-15-9709-2015.

1282 Johnson, C. E., W. J. Collins, D. S. Stevenson, and R. G. Derwent (1999), Relative roles
1283 of climate and emissions changes on future tropospheric oxidant concentrations, *J.*
1284 *Geophys. Res.*, *104*(D15), 18631-18645, doi:10.1029/1999jd900204.

1285 Krol, M., and J. Lelieveld (2003), Can the variability in tropospheric OH be deduced
1286 from measurements of 1,1,1-trichloroethane (methyl chloroform)? *J. Geophys. Res.,*
1287 *108*(D3), 4125, doi:10.1029/2002JD002423.

1288 Kruger, K., and B. Quack (2013), Introduction to special issue: the TransBrom Sonne
1289 expedition in the tropical West Pacific, *Atmos. Chem. Phys.*, *13*(18), 9439-9446,
1290 doi:10.5194/acp-13-9439-2013.

1291 Lamarque, J.-F., et al. (2012), CAM-chem: description and evaluation of interactive
1292 atmospheric chemistry in the Community Earth System Model, *Geosci. Model Dev.*,
1293 *5*(2), 369-411, doi:10.5194/gmd-5-369-2012.

1294 Law, K. S., et al. (2007), Halogenated Very Short-Lived Substances, Chapter 2 in
1295 *Scientific Assessment of Ozone Depletion: 2006,* Global Ozone Research and
1296 Monitoring Project—Report No. 50, 572 pp., World Meteorological Organization,
1297 Geneva, Switzerland.

1298 Law, K., et al. (2014), Arctic Air Pollution: New Insights From POLARCAT-IPY, *Bull.*
1299 *Amer. Meteor. Soc.*, *95*(12), 1873-1895, doi:10.1175/BAMS-D-13-00017.1.

1300 Levy, H. (1971), Normal atmosphere: large radical and formaldehyde concentrations
1301 predicted, *Science*, *173*(3992), 141-143, doi:10.1126/science.173.3992.141.

1302 Liang, Q., E. Atlas, D. Blake, M. Dorf, K. Pfeilsticker, and S. Schauffler (2014),
1303 Convective transport of very short lived bromocarbons to the stratosphere, *Atmos.*
1304 *Chem. Phys.*, *14*(11), 5781-5792, doi:10.5194/acp-14-5781-2014.

1305 Mao, J., et al. (2010), Chemistry of hydrogen oxide radicals (HO_x) in the Arctic
1306 troposphere in spring, *Atmos. Chem. Phys.*, *10*(13), 5823–5838, doi:10.5194/acp-10-
1307 5823-2010.

1308 Mao, J., F. Paulot, D. J. Jacob, R. C. Cohen, J. D. Crounse, P. O. Wennberg, C. A. Keller,
1309 R. C. Hudman, M. P. Barkley, and L. W. Horowitz (2013a), Ozone and organic
1310 nitrates over the eastern United States: Sensitivity to isoprene chemistry, *J. Geophys.*
1311 *Res.*, *118*(19), 11256–11268, doi:10.1002/jgrd.50817.

1312 Mao, J., S. Fan, D. J. Jacob, and K. R. Travis (2013b), Radical loss in the atmosphere
1313 from Cu-Fe redox coupling in aerosols, *Atmos. Chem. Phys.*, *13*(2), 509-519,
1314 doi:10.5194/acp-13-509-2013.

1315 Mauldin III, R. L., et al. (2003), Highlights of OH, H_2SO_4, and methane sulfonic acid
1316 measurements made aboard the NASA P-3B during Transport and Chemical
1317 Evolution over the Pacific, *J. Geophys. Res.*, *108*(D20), 8796, doi:
1318 10.1029/2003JD003410.

1319 Meinshausen, M., et al. (2011), The RCP greenhouse gas concentrations and their
1320 extensions from 1765 to 2300, *Climatic Change*, *109*(1-2), 213-241,
1321 doi:10.1007/s10584-011-0156-z.

1322 Millet, D. B., et al. (2010), Global atmospheric budget of acetaldehyde: 3-D model
1323 analysis and constraints from in-situ and satellite observations, *Atmos. Chem. Phys.*,
1324 *10*(7), 3405-3425, doi:10.5194/acp-10-3405-2010.

1325 Monks, S. A., et al. (2015), Multi-model study of chemical and physical controls on
1326 transport of anthropogenic and biomass burning pollution to the Arctic, *Atmos. Chem.*
1327 *Phys.*, *15*(6), 3575-3603, doi:10.5194/acp-15-3575-2015.

1328 Montzka, S. A., M. Krol, E. Dlugokencky, B. Hall, P. Jockel, and J. Lelieveld (2011),
1329 Small Interannual Variability of Global Atmospheric Hydroxyl, *Science*, *331*(6013),
1330 67-69, doi:10.1126/science.1197640.

1331 Murray, L. T., J. A. Logan, and D. J. Jacob (2013), Interannual variability in tropical
1332 tropospheric ozone and OH: The role of lightning, *J. Geophys. Res.*, *118*(19), 11468-
1333 11480, doi:10.1002/jgrd.50857.

1334 Naik, V., et al. (2013), Preindustrial to present-day changes in tropospheric hydroxyl
1335 radical and methane lifetime from the Atmospheric Chemistry and Climate Model

1336 Intercomparison Project (ACCMIP), *Atmos. Chem. Phys.*, *13*(10), 5277-5298,
1337 doi:10.5194/acp-13-5277-2013.

1338 Navarro, M. A., et al. (2015), Airborne measurements of organic bromine compounds in
1339 the Pacific tropical tropopause layer, *112*, 13789, *P. Natl. Acad. Sci. U.S.A.*, *112*(45),
1340 13789-13793, doi:10.1073/pnas.1511463112.

1341 Newell, R. E., and S. Gould-Stewart (1981), A Stratospheric Fountain?, *J. Atmos. Sci.*,
1342 *38*(12), 2789-2796, doi:10.1175/1520-0469(1981)038<2789:asf>2.0.co;2.

1343 Newton, R., G. Vaughan, H. M. A. Ricketts, L. L. Pan, A. J. Weinheimer, and C. Chemel
1344 (2016), Ozonesonde profiles from the West Pacific Warm Pool: measurements and
1345 validation, *Atmos. Chem. Phys.*, *16*, 619-634, doi:10.5194/acp-16-619-2016.

1346 NOAA (2014), ATom selected for funding under the NASA EVS-2 program, edited,
1347 NOAA Earth System Research Laboratory News and Events, available at
1348 http://www.esrl.noaa.gov/csd/news/2014/160_1125.html

1349 Olson, J. R., et al. (2001), Seasonal differences in the photochemistry of the South
1350 Pacific: A comparison of observations and model results from PEM-Tropics A and B,
1351 *J. Geophys. Res.*, *106*(D23), 32749-32766, doi: 10.1029/2001JD900077.

1352 Olson, J. R., et al. (2004), Testing fast photochemical theory during TRACE-P based on
1353 measurements of OH, HO_2, and CH_2O, *J. Geophys. Res.*, *109*(D15), D15S10,
1354 doi:10.1029/2003JD004278.

1355 Palancar, G. G., R. E. Shetter, S. R. Hall, B. M. Toselli, and S. Madronich (2011),
1356 Ultraviolet actinic flux in clear and cloudy atmospheres: model calculations and
1357 aircraft-based measurements, *Atmos. Chem. Phys.*, *11*(11), 5457-5469,
1358 doi:10.5194/acp-11-5457-2011.

1359 Pan, L. L., et al. (2015), Bimodal distribution of free tropospheric ozone over the tropical
1360 western Pacific revealed by airborne observations, *Geophys. Res. Lett.*, *42*(18), 7844-
1361 7851, doi:10.1002/2015gl065562.

1362 Pan, L. L., et al., *accepted* (2016), The CONvective TRansport of Active Species in the
1363 Tropics (CONTRAST) Experiment, *B. Am. Meteorol. Soc*., doi:10.1175/BAMS-D-
1364 14-00272.1.

1365 Prather, M. J., C. D. Holmes, and J. Hsu (2012), Reactive greenhouse gas scenarios:
1366 Systematic exploration of uncertainties and the role of atmospheric chemistry,
1367 *Geophys. Res. Lett.*, *39*(9), L09803, doi:10.1029/2012GL051440.

1368 Prinn, R. G., et al. (2005), Evidence for variability of atmospheric hydroxyl radicals over
1369 the past quarter century, *Geophys. Res. Lett.*, *32*(7), L07809,
1370 doi:10.1029/2004gl022228.

1371 Read, K. A., L. J. Carpenter, S. R. Arnold, R. Beale, P. D. Nightingale, J. R. Hopkins, A.
1372 C. Lewis, J. D. Lee, L. Mendes, and S. J. Pickering (2012), Multiannual Observations
1373 of Acetone, Methanol, and Acetaldehyde in Remote Tropical Atlantic Air:
1374 Implications for Atmospheric OVOC Budgets and Oxidative Capacity, *Environ. Sci.*
1375 *Tech.*, *46*, 11028-11039, doi:10.1021/es302082p.

1376 Rex, M., et al. (2014), A tropical West Pacific OH minimum and implications for
1377 stratospheric composition, *Atmos. Chem. Phys.*, *14*(9), 4827-4841, doi:10.5194/acp-
1378 14-4827-2014.

1379 Ridder, T., C. Gerbig, J. Notholt, M. Rex, O. Schrems, T. Warneke, and L. Zhang (2012),
1380 Ship-borne FTIR measurements of CO and O_3 in the Western Pacific from 43° N to
1381 35° S: an evaluation of the sources, *Atmos. Chem. Phys.*, *12*, 815-828,
1382 doi:10.5194/acp-12-815-2012.

1383 Ridley, B. A., and F. E. Grahek (1990), A small, low flow, high-sensitivity reaction
1384 vessel for NO chemiluminescence detectors, *J. Atmos. Ocean. Tech.*, *7*(2), 307-311,
1385 doi:10.1175/1520-0426(1990)007<0307:aslfhs>2.0.co;2.

1386 Saiz-Lopez, A., R. P. Fernandez, C. Ordóñez, D. E. Kinnison, J. C. Gómez Martín, J.-F.
1387 Lamarque, and S. Tilmes (2014), Iodine chemistry in the troposphere and its effect on
1388 ozone, *Atmos. Chem. Phys.*, *14*, 13119-13143, doi:10.5194/acp-14-13119-2014.

1389 Salawitch, R. J., D. K. Weisenstein, L. J. Kovalenko, C. E. Sioris, P. O. Wennberg, K.
1390 Chance, M. K. W. Ko, and C. A. McLinden (2005), Sensitivity of ozone to bromine
1391 in the lower stratosphere, *Geophys. Res. Lett.*, *32*(5), L05811,
1392 doi:10.1029/2004gl021504.

1393 Sander, S. P., et al. (2011), Chemical Kinetics and Photochemical Data for Use in
1394 Atmospheric Studies, Evaluation No. 17, *Rep.*, Jet Propulsion Laboratory, Pasadena,
1395 CA.

1396 Saunders, S. M., M. E. Jenkin, R. G. Derwent, and M. J. Pilling (2003), Protocol for the
1397 development of the Master Chemical Mechanism, MCM v3 (Part A): tropospheric
1398 degradation of non-aromatic volatile organic compounds, *Atmos. Chem. Phys.*, *3*(1),
1399 161-180, doi:10.5194/acp-3-161-2003.

1400 Shetter, R. E., and M. Muller (1999), Photolysis frequency measurements using actinic
1401 flux spectroradiometry during the PEM-Tropics mission: Instrumentation description
1402 and some results, *J. Geophys. Res.*, *104*(D5), 5647-5661, doi:10.1029/98jd01381.

1403 Shindell, D. T., et al. (2006), Multimodel simulations of carbon monoxide: Comparison
1404 with observations and projected near-future changes, *J. Geophys. Res.*, *111*(D19),
1405 D19306, doi:10.1029/2006jd007100.

1406 Singh, H. B. (1977), Atmospheric halocarbons - evidence in favor of reduced average
1407 hydroxyl radical concentration in troposphere, *Geophys. Res. Lett.*, *4*(3), 101-104,
1408 doi:10.1029/GL004i003p00101.

1409 Singh, H. B. and P. L. Hanst (1981), Peroxyacetyl Nitrate (PAN) in the Unpolluted
1410 Atmosphere: An Important Reservoir for Nitrogen Oxides, *Geophys. Res. Lett.*, *8*(8),
1411 941-944, doi:10.1029/GL008i008p00941.

1412 Singh, H. B., A. Tabazadeh, M. J. Evans, B. D. Field, D. J. Jacob, G. Sachse, J. H.
1413 Crawford, R. Shetter, and W. H. Brune (2003), Oxygenated volatile organic
1414 chemicals in the oceans: Inferences and implications based on atmospheric
1415 observations and air-sea exchange models, *Geophys. Res. Lett.*, *30*(16), 1862,
1416 doi:10.1029/2003gl017933.

1417 Singh, H. B., et al. (2004), Analysis of the atmospheric distribution, sources, and sinks of
1418 oxygenated volatile organic chemicals based on measurements over the Pacific during
1419 TRACE-P, *J. Geophys. Res.*, *109*(D15), D15S07, doi:10.1029/2003jd003883.

1420 SPARC (2013), SPARC Report on Lifetimes of Stratospheric Ozone-Depleting
1421 Substances, Their Replacements, and Related Species, M. K. W. Ko, P. A. Newman,
1422 S. Reimann, S. E. Strahan (Eds.), SPARC Report No. 6, WCRP-15/2013, available at
1423 www.sparc-climate.org/publications/sparc-reports/.

1424 Spivakovsky, C. M., et al. (2000), Three-dimensional climatological distribution of
1425 tropospheric OH: Update and evaluation, *J. Geophys. Res.*, *105*(D7), 8931-8980,
1426 doi:10.1029/1999JD901006.

1427 Stevenson, D. S., C. E. Johnson, W. J. Collins, R. G. Derwent, and J. M. Edwards (2000),
1428 Future estimates of tropospheric ozone radiative forcing and methane turnover - the
1429 impact of climate change, *Geophys. Res. Lett.*, *27*(14), 2073-2076,
1430 doi:10.1029/1999gl010887.

1431 Stevenson, D. S., et al. (2006), Multimodel ensemble simulations of present-day and
1432 near-future tropospheric ozone, *J. Geophys. Res.*, *111*(D8), D08301,
1433 doi:10.1029/2005jd006338.

1434 Strahan, S. E., B. N. Duncan, and P. Hoor (2007), Observationally derived transport
1435 diagnostics for the lowermost stratosphere and their application to the GMI chemistry
1436 and transport model, *Atmos. Chem. Phys.*, *7*, 2435–2445, doi:10.5194/acp-7-2435-
1437 2007.

1438 Strode, S. A., B. N. Duncan, E. A. Yegorova, J. Kouatchou, J. R. Ziemke, and A. R.
1439 Douglass (2015), Implications of carbon monoxide bias for methane lifetime and
1440 atmospheric composition in chemistry climate models, *Atmos. Chem. Phys.*, *15*(20),
1441 11789-11805, doi:10.5194/acp-15-11789-2015.

1442 Tan, D., et al. (2001), OH and HO_2 in the tropical Pacific: Results from PEM-Tropics B,
1443 *J. Geophys. Res.*, *106*(D23), 32667-32681, doi:10.1029/2001jd900002.

1444 Tilmes, S., et al. (2015), Description and evaluation of tropospheric chemistry and
1445 aerosols in the Community Earth System Model (CESM1.2), *Geosci. Model Dev.*,
1446 *8*(5), 1395-1426, doi:10.5194/gmd-8-1395-2015.

van Vuuren, D. P., et al. (2011), The representative concentration pathways: an overview, *Climatic Change*, *109*(1-2), 5-31, doi:10.1007/s10584-011-0148-z.

Voulgarakis, A., et al. (2013), Analysis of present day and future OH and methane lifetime in the ACCMIP simulations, *Atmos. Chem. Phys.*, *13*(5), 2563-2587, doi:10.5194/acp-13-2563-2013.

Wang, J. S., M. B. McElroy, J. A. Logan, P. I. Palmer, W. L. Chameides, Y. Wang, and I. A. Megretskaia (2008), A quantitative assessment of uncertainties affecting estimates of global mean OH derived from methyl chloroform observations, *J. Geophys. Res., 113*(D12), D12302, doi:10.1029/2007JD008496.

Wennberg, P. O., S. Peacock, J. T. Randerson, and R. Bleck (2004), Recent changes in the air-sea gas exchange of methyl chloroform, *Geophys. Res. Lett., 31*(16), L16112, doi:10.1029/2004GL020476.

Wiedinmyer, C., S. K. Akagi, R. J. Yokelson, L. K. Emmons, J. A. Al-Saadi, J. J. Orlando, and A. J. Soja (2011), The Fire INventory from NCAR (FINN): a high resolution global model to estimate the emissions from open burning, *Geosci. Model Dev.*, *4*(3), 625-641, doi:10.5194/gmd-4-625-2011.

Williams, J. E., P. F. J. van Velthoven, and C. A. M. Brenninkmeijer (2013), Quantifying the uncertainty in simulating global tropospheric composition due to the variability in global emission estimates of Biogenic Volatile Organic Compounds, *Atmos. Chem. Phys.*, *13*, 2857–2891, doi:10.5194/acp-13-2857-2013.

WMO (2011), Scientific Assessment of Ozone Depletion: 2010, *Rep.*, 516 pp, Global Ozone Research and Monitoring Project, Geneva, Switzerland.

Wolfe, G. M., and J. A. Thornton (2011), The Chemistry of Atmosphere-Forest Exchange (CAFE) Model - Part 1: Model description and characterization, *Atmos. Chem. Phys.*, *11*(1), 77-101, doi:10.5194/acp-11-77-2011.

Wolter, K., and M. S. Timlin (2011), El Niño/Southern Oscillation behaviour since 1871 as diagnosed in an extended multivariate ENSO index (MEI.ext), *Int. J. Climatol.*, *31*(7), 1074-1087, doi:10.1002/joc.2336.

Zeng, G., and J. A. Pyle (2005), Influence of El Niño Southern Oscillation on stratosphere/troposphere exchange and the global tropospheric ozone budget, *Geophys. Res. Lett.*, *32*(1), L01814, doi:10.1029/2004GL021353.

Ziemke, J. R., S. Chandra, L. D. Oman, and P. K. Bhartia (2010), A new ENSO index derived from satellite measurements of column ozone, *Atmos. Chem. Phys.*, *10*(8), 3711-3721, doi:10.5194/acp-10-3711-2010.

Zondlo, M. A., M. E. Paige, S. M. Massick, and J. A. Silver (2010), Vertical cavity laser hygrometer for the National Science Foundation Gulfstream-V aircraft, *J. Geophys. Res.*, *115*, D20309, doi:10.1029/2010jd014445.

Table 1. Tropospheric OH Columns Calculated for the CONTRAST Mean OH Vertical Profile and CAM-Chem Model Simulations

C-C Box Model Run	OH Column (10^{12} cm^{-2})[a]	Ratio (Run X / C-C)
GV	2.17	1.12
C-C (CONTRAST)	1.94	---
C-C, GV NO_x	2.61	1.35
C-C, GV H_2O	1.61	0.83
C-C, GV J(O^1D)	2.16	1.11
C-C, GV CH_3CHO	1.77	0.91
C-C, GV O_3	2.06	1.06
C-C, GV CO	1.83	0.94
C-C, GV HCHO	2.01	1.04
C-C, GV J(NO_2)	1.97	1.02
C-C, GV C_5H_8	1.95	1.01
GV, C-C J(O^1D)+J(NO_2)	1.92	0.99

[a]Columns are integrated from the surface to 13 km (~200 hPa)

Table 2. Tropospheric OH Columns Calculated for the CONTRAST Mean OH Vertical Profile and POLMIP Model Simulations

POLMIP Box Model Run	OH Column[a] (10^{12} cm^{-2})	Ratio (GV / Run X)
GV	2.17	---
C-C (POLMIP)	1.56	1.39
POLMIP MMM	1.54	1.41
GV, POL NO_x	1.70	1.28
GV, POL J(O^1D)	1.96	1.11
GV, POL CH_3CHO	2.38	0.91
GV, POL O_3	2.30	0.94
GV, POL CO	2.26	0.96
GV, POL J(NO_2)	2.09	1.04
GV, POL HCHO	2.11	1.03
GV, POL H_2O	2.12	1.02
GV, POL C_5H_8	2.17	1.00

[a]Columns are integrated from the surface to 200 hPa (~13 km)

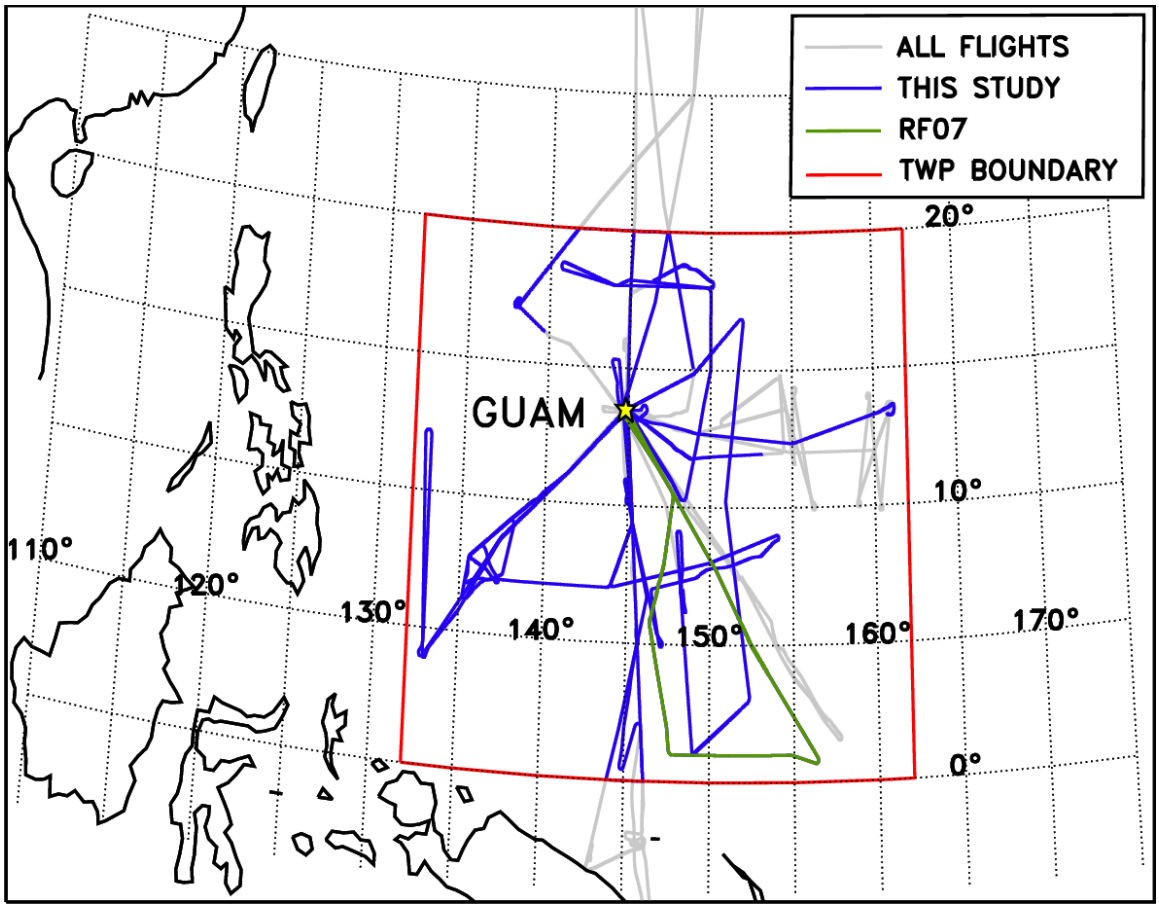

Figure 1. Flight tracks of the GV aircraft during the CONTRAST campaign, January – February 2014. Portions of flight tracks used in this study are shown in blue; criteria for including aircraft data are SZA ≤ 60°, latitude between 0°N and 20°N, and longitude between 132°E and 162°E (latitude/longitude bounds indicated by red box), and presence of valid data for O_3 and CO at the time and location of observation. Portions of flight tracks not included in this study are shown in grey. Research Flight (RF) 07 is highlighted in green.

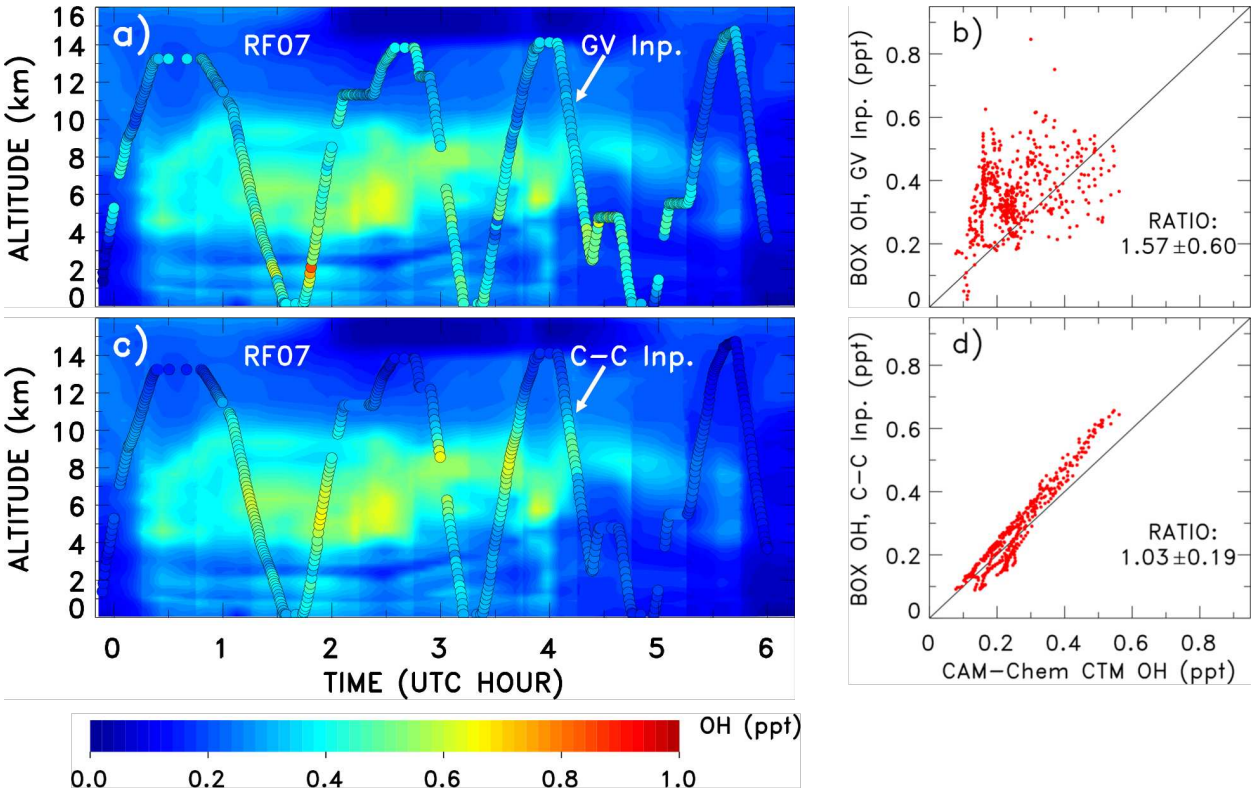

Figure 2. Box modeled OH compared to OH output from the CAM-Chem CTM run using meteorology for the CONTRAST campaign; results here are for RF07 (29 January 2014): (a) the background "curtain" shows profiles of OH mixing ratios from the CAM-Chem CTM calculated for the latitude, longitude and SZA of the GV aircraft; the over-plotted circles (GV Inp.) show OH output from the DSMACC box model constrained to CONTRAST observations; (b) scatter plot of box modeled OH versus CAM-Chem OH for the altitude of the GV; (c) same as a) but with box model (C-C Inp.) now constrained to OH precursors (Section 2.2) from CAM-Chem; (d) same as b) but with box model constrained to OH precursors from CAM-Chem. The black line on the scatter plots is the 1:1 line. The mean and standard deviation of the ratio (BOX OH)/(CAM-Chem OH) are indicated.

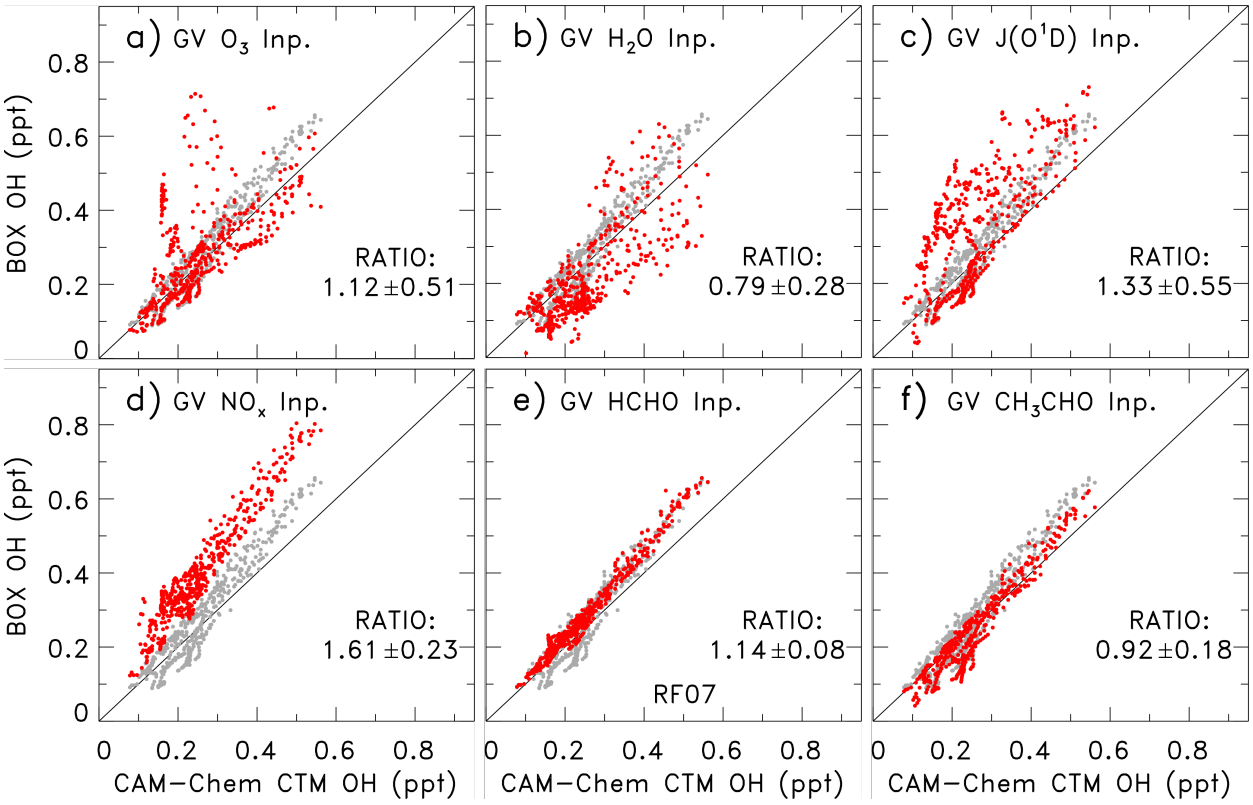

Figure 3. Same as scatter plots in Fig. 2, except box model is constrained to output from the CAM-Chem CTM for all OH precursors with the exception of the precursor indicated by the label on each plot. Values for the labeled precursor are from CONTRAST (GV) observations obtained on RF07. The OH precursors constrained by measurements are: O_3 (panel a), H_2O (b), $J(O^1D)$ (c), NO (with steady-state NO_2 calculated by the box model to give NO_x) (d), HCHO (e), and CH_3CHO (f). Grey points in the background are the same as the red points in Fig. 2d, for the sake of visual comparison. The mean and standard deviation of the ratio (BOX OH)/(CAM-Chem OH) are indicated.

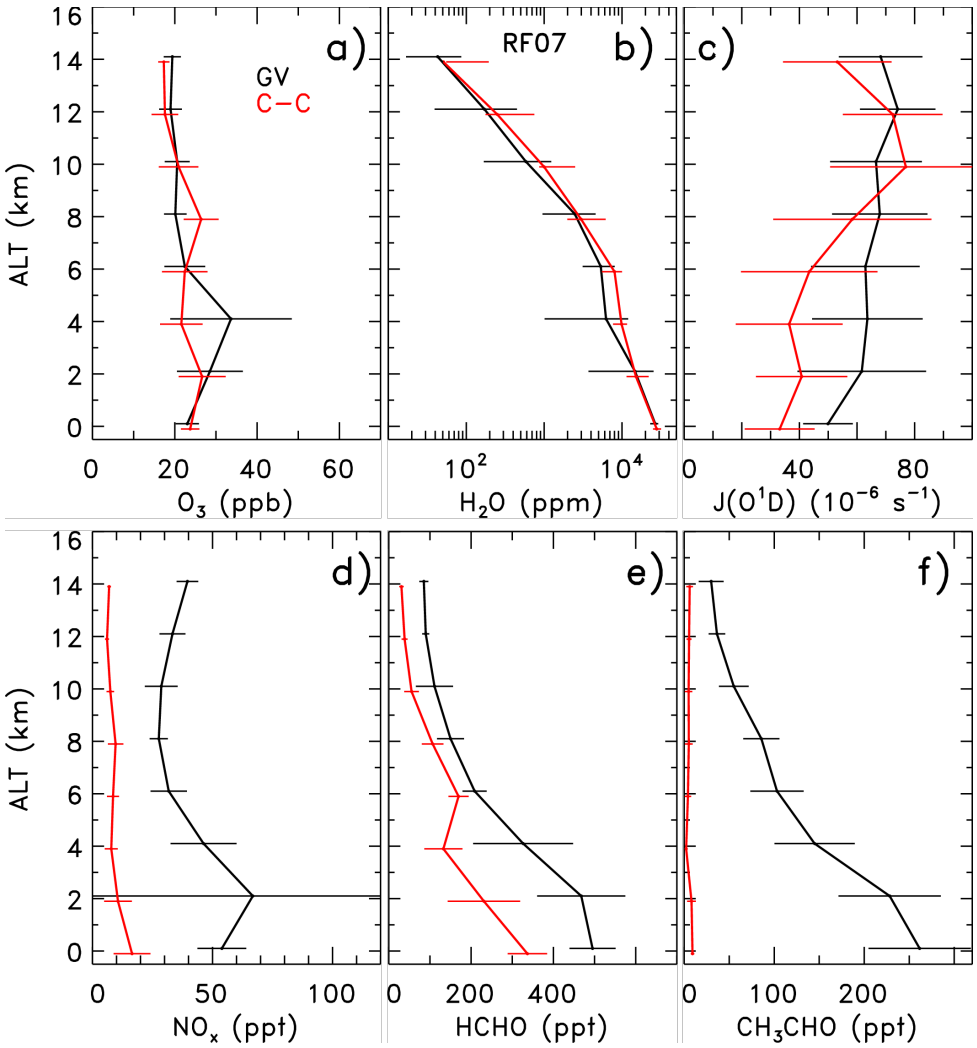

Figure 4. Vertical profiles of mean O_3 (panel a), H_2O (b), $J(O^1D)$ (c), NO_x (d), HCHO (e), and CH_3CHO (f) mixing ratios, averaged for CONTRAST RF07, subject to the selection filter for daytime TWP conditions described in Methods. GV observations are shown in black for all species except NO_x; output from the CAM-Chem CTM, extracted along the flight track to match the time and location of GV observations, is shown in red. The GV NO_x is calculated using observed NO and box modeled NO_2, where the box model was constrained to GV observations of NO, O_3, and hydrocarbons. Data and model output are averaged within 2 km altitude bins. Error bars show the standard deviation about the mean except for H_2O, where error bars show the 5th and 95th percentiles.

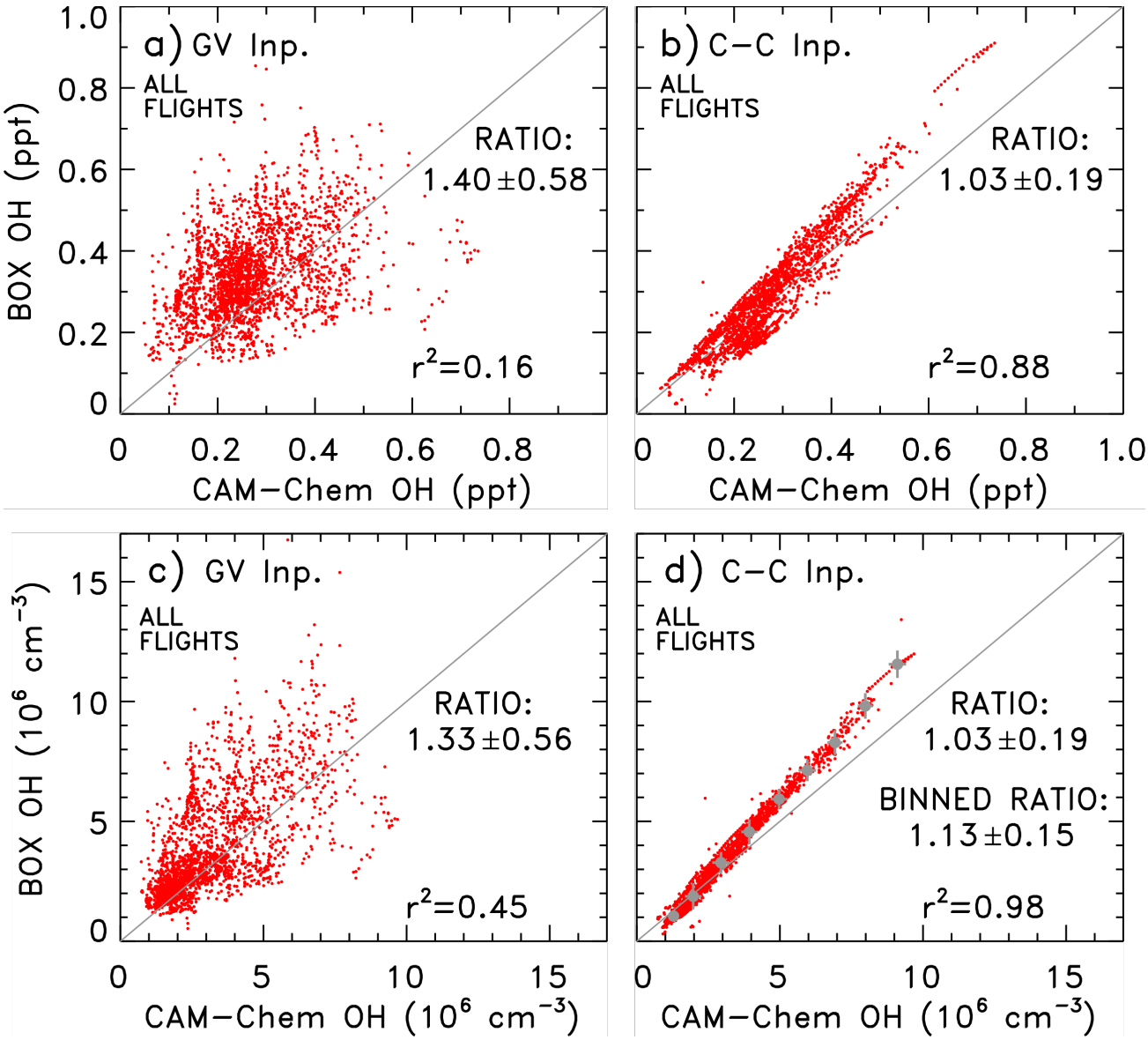

Figure 5. Correlation plots of box modeled OH versus CAM-Chem CTM OH for the entire CONTRAST campaign, with application of the filter used to select daytime observations in the TWP (Section 2.1). (a) Box modeled OH found using constraints for OH precursors from the CONTRAST GV observations; (b) box modeled OH found using constraints from CAM-Chem CTM. Panels (c) and (d) are the same as panels (a) and (b), respectively, except OH is represented as number density instead of mixing ratio. The square of the correlation coefficient (r^2) and the mean and standard deviation of the ratio (BOX OH)/(CAM-Chem OH) are indicated. Panel (d) also shows statistics performed by averaging the CAM-Chem OH values within 1×10^6 cm^{-3} interval bins; the mean BOX OH values are determined for those bins and the resulting mean and standard deviations are shown in grey. The ratio of (BOX OH)/(CAM-Chem OH) for the grey points is indicated as the "binned ratio".

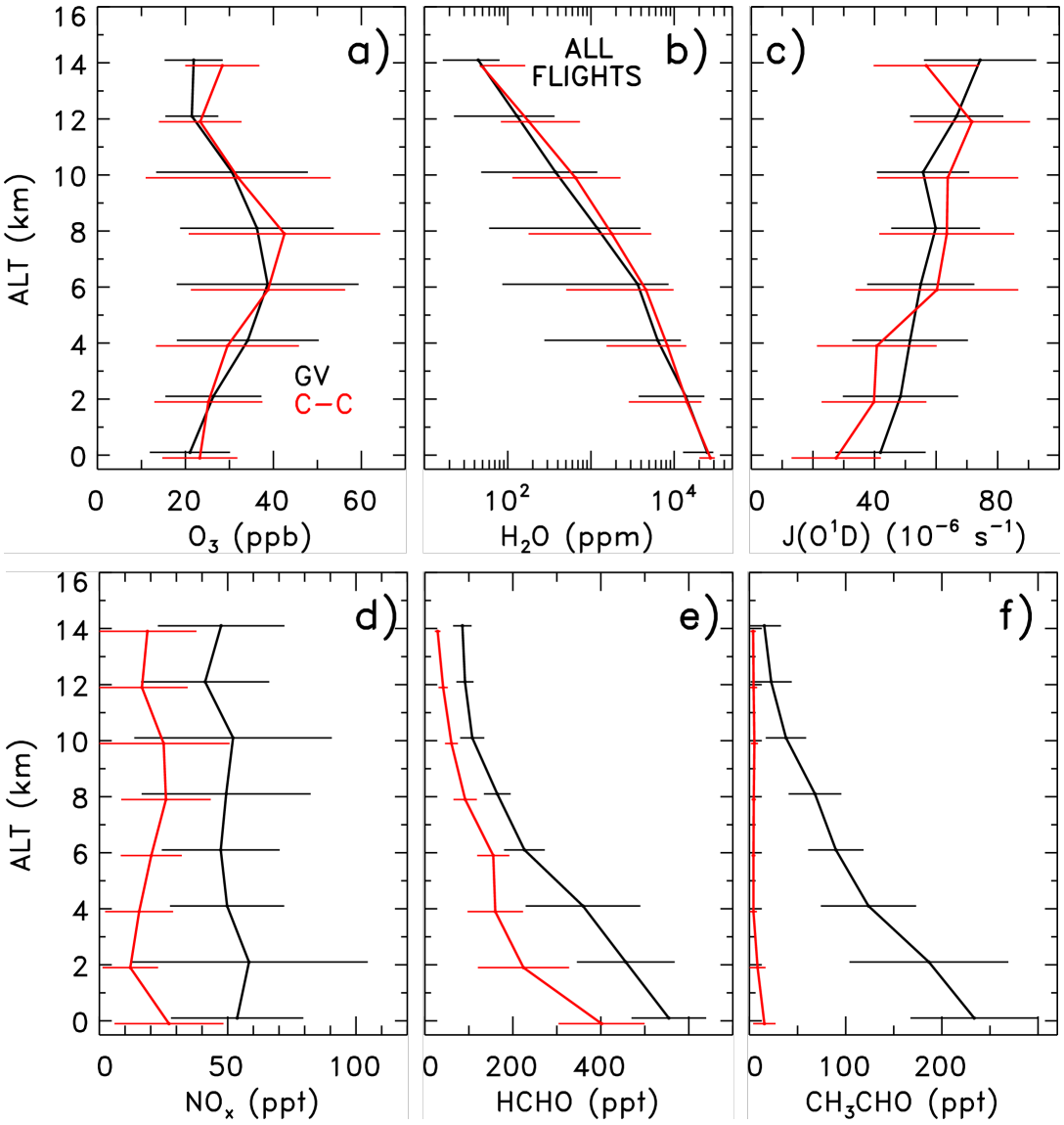

Figure 6. Same as Figure 4 except vertical profiles are calculated for the entire CONTRAST campaign, subject to the time and location filter described in Section 2.1.

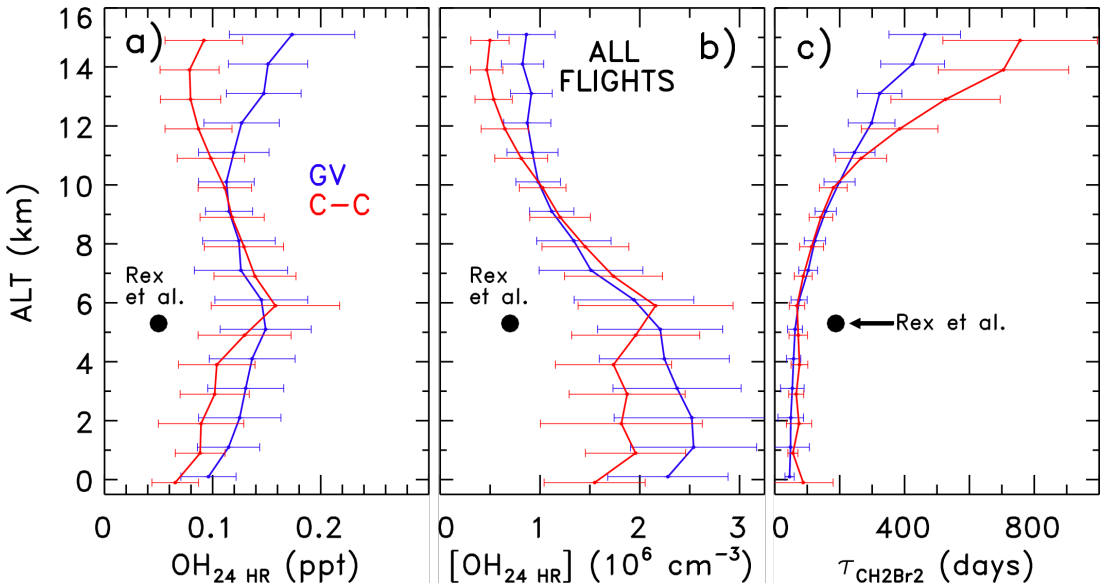

Figure 7. 24-hour average OH ($OH_{24\ HR}$) and lifetime of CH_2Br_2 (τ_{CH2Br2}) from the DSMACC box model for the entire CONTRAST campaign, subject to the time and location filter described in Section 2.1, separated into 1 km altitude bins. Panel a) shows $OH_{24\ HR}$ mixing ratio; panel b) shows $OH_{24\ HR}$ number density; panel c) shows τ_{CH2Br2} with respect to loss by OH. Blue line denotes box model $OH_{24\ HR}$ and τ_{CH2Br2} for runs constrained to GV measurements; red line denotes box model $OH_{24\ HR}$ for runs constrained to CAM-Chem output. Error bars signify standard deviation about the mean of $OH_{24\ HR}$ and τ_{CH2Br2}, for each altitude bin. Error bars are offset slightly in altitude for clarity. We also show $OH_{24\ HR}$ and τ_{CH2Br2} at 500 hPa (which we place at 5.3 km altitude) reported by *Rex et al.* [2014] above the equator on 1 October 2009.

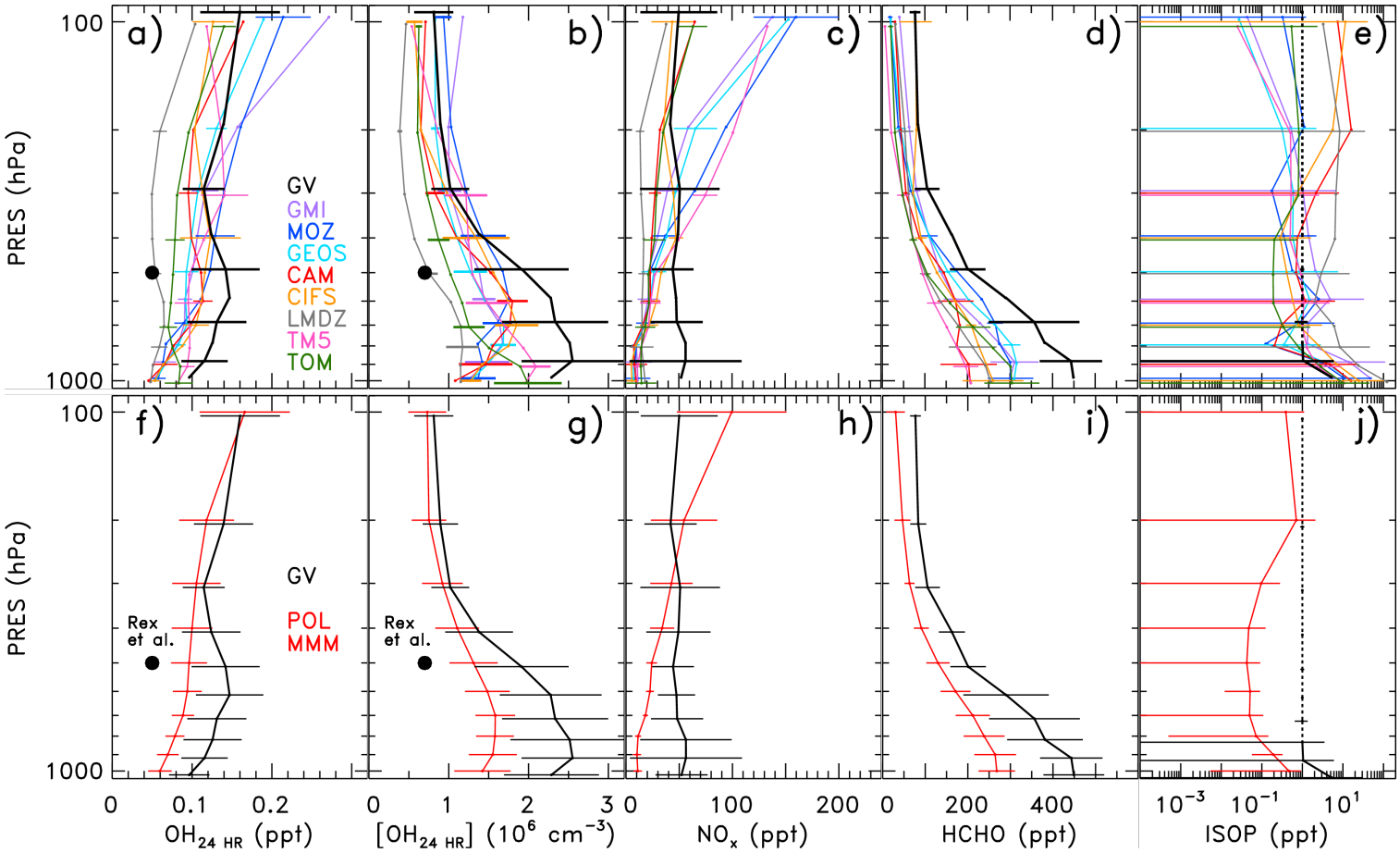

Figure 8. Vertical profiles of monthly mean OH mixing ratio (panels a and f), OH concentration (b, g), NO_x (c, h), HCHO (d, i), and C_5H_8 (e, j) from the POLMIP archive for eight CTMs (colored lines) for January and February 2008 averaged within the TWP region shown in Figure 1. The black solid lines, described in greater detail below, represent either inferred OH or GV observations. The upper set of panels shows profiles from each POLMIP CTM, while the lower set shows the POLMIP multi-model mean. Error bars show 1 standard deviation about the mean of the various quantities, in 100 hPa pressure bins; they are offset slightly in the vertical for clarity. For the top panels, some of the error bars are omitted to avoid clutter. The black solid lines show 24-hour mean OH mixing ratio (panels a and f) and OH concentration (b, g) output from the DSMACC box model constrained by GV inputs. The same latitude/longitude filter, specific to the TWP, has been applied to the POLMIP archive and inferred OH values. In addition, the inference of $OH_{24\ HR}$ is based only on daytime data. The OH panels also show the October 2009 value at 500 hPa in the TWP from *Rex et al.* [2014]. The black solid lines for NO_x are 24 hour averages of the diel output (15 minute grid) of NO plus NO_2 from DSMACC, for calculations constrained to match observed NO at the SZA of observation. The black solid lines for HCHO also represent 24-hour average values, which in this case are found by scaling the observed HCHO to $HCHO_{24\ HR}$ using the UWCM chemical box model (see text). The scaling for HCHO is close to unity at all altitudes because the photochemical lifetime of HCHO is on the order of a few hours (see supplement). The CTM/observation comparison for C_5H_8 (ISOP) is handled in a different manner. The top plot (panel e) compares the mean and standard deviation from each CTM to the observed mean and standard deviation; often, C_5H_8 was below the limit of detection of the TOGA instrument, 1 ppt, because our analysis is focused on the remote TWP. The black dotted line depicts the instrument limit of detection for pressure bins where this is the case. C_5H_8 from the POLMIP CTMs in panel j) (red line) is represented as the multi-model mean of the median values, due to the non-Gaussian distribution of values in the TWP region.

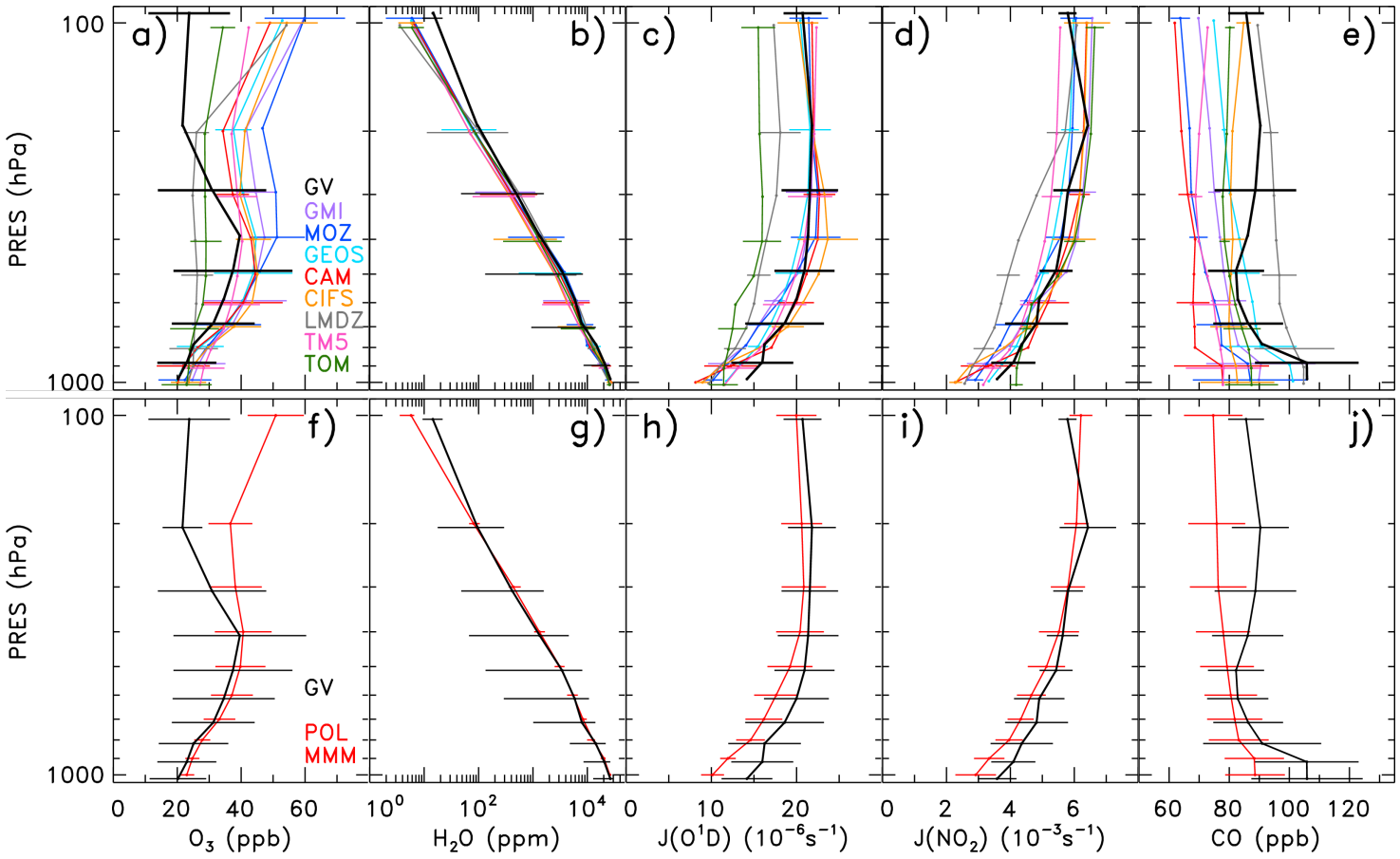

Figure 9. Same as Figure 8, except for O_3 (panels a and f), H_2O (b, g), $J(O^1D)$ (c, h), $J(NO_2)$ (d, i), and CO (e, j) from observations and from the 8 POLMIP CTMs. The comparisons for O_3, H_2O, and CO show the monthly mean values from the POLMIP archive for January and February 2008 and the mean profiles observed during CONTRAST, since all of these quantities have long photochemical lifetimes. The plots for $J(O^1D)$ and $J(NO_2)$ compare monthly mean values from the POLMIP archive to 24 hour averages of the diel output (15 minute grid) of $J(O^1D)$ and $J(NO_2)$ from DSMACC, for calculations constrained to match observed $J(O^1D)$ and $J(NO_2)$ at the SZA of observation. Error bars show 1 standard deviation about the mean, except for H_2O, where error bars represent the 5th and 95th percentiles.

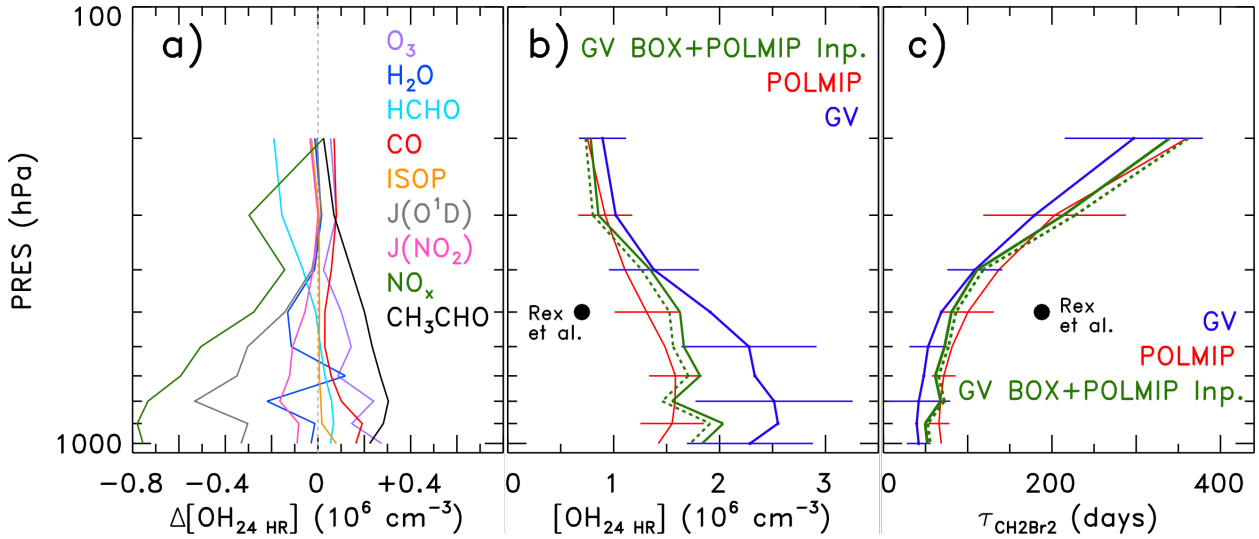

Figure 10. Panel a) shows the difference in $[OH_{24\ HR}]$ between a run of the DSMACC box model constrained to GV observations of all OH precursors with the exception of the indicated species and another run of the model constrained to GV observations of all OH precursors, where indicated species refers to the POLMIP multi-model mean value. These box model difference plots have been conducted at 100 hPa intervals. Panel b) shows the mean and standard deviation $[OH_{24\ HR}]$ profile calculated by the DSMACC box model constrained to GV observations of OH precursors (blue) compared to the multi-model mean and standard deviation of monthly mean [OH] in the POLMIP archive from eight CTMs (red). The solid green line represents $[OH_{24\ HR}]^{CONTRAST}$ (blue) + $\Delta[OH_{24\ HR}]^{ALL}$, where $\Delta[OH_{24\ HR}]^{ALL}$ represents the difference between a run of the DSMACC box model constrained to POLMIP multi-model mean values of all nine OH precursors and another run of the model constrained to GV observations of all nine OH precursors. The profile of $\Delta[OH_{24\ HR}]^{ALL}$ is nearly identical to the sum of the nine terms shown in panel a) (see supplement). The dashed green line is adjusted to account for the 13% high bias in daytime OH calculated by the box model, or ~6.5% high bias in $OH_{24\ HR}$, attributable to the box model chemical mechanism (from Figure 5d). The calculation of the dashed green line is identical to the solid green line except that values of $[OH_{24\ HR}]$ are multiplied by $^1/_{1.065}$. Panel c) shows lifetime of CH_2Br_2 (τ_{CH2Br2}) with respect to loss by OH for $[OH_{24\ HR}]$ from the box model constrained to GV measurements (blue), for the multi-model monthly mean [OH] from the POLMIP CTMs (red), and for $[OH_{24\ HR}]$ from the box model constrained to the nine OH precursors from POLMIP (solid green). The dashed green line in panel c) shows τ_{CH2Br2} calculated for adjusted values of $[OH_{24\ HR}]$ in panel b) represented by the green dashed line. Values of $[OH_{24\ HR}]$ and τ_{CH2Br2} reported by *Rex et al.* [2014] at 500 hPa for October 2009 in the TWP are shown in panels b) and c).

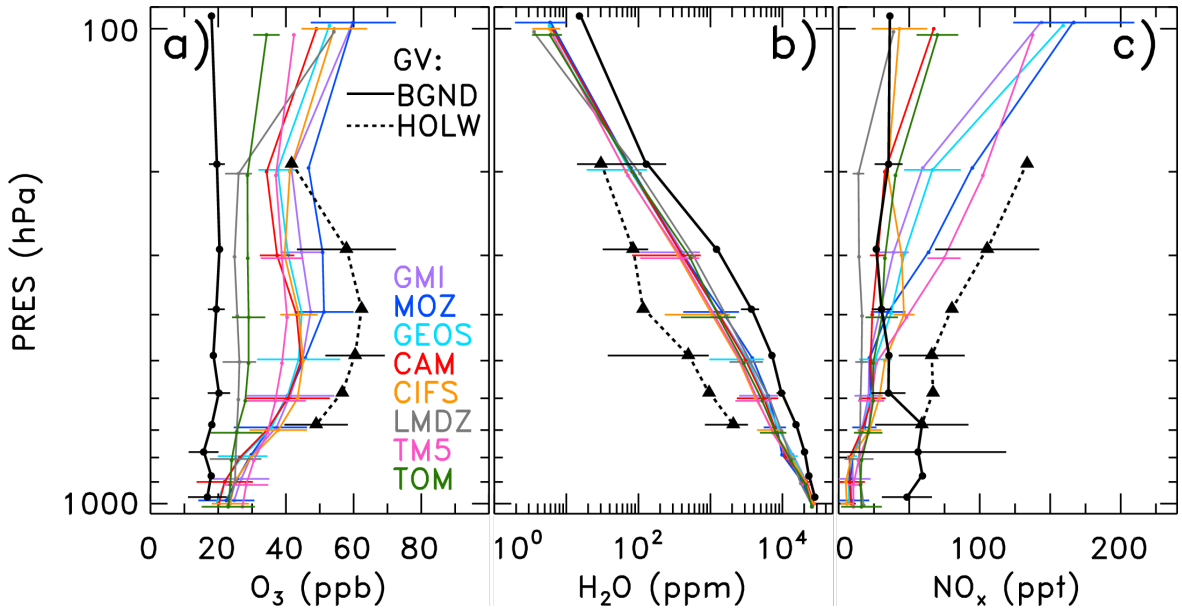

Figure 11. Vertical profiles of monthly mean O_3 (panel a), H_2O (b), and NO_x (c) mixing ratio from the POLMIP archive for 8 CTMs (colored lines) for January and February 2008 compared to profiles of these 3 species measured by the GV during CONTRAST for background conditions (BGND) and well-defined high O_3, low H_2O (HOLW) structures. Criteria for BGND are simultaneous RH > 70%, O_3 < 25 ppb; criteria for HOLW are simultaneous RH < 20%, O_3 > 40 ppb. Relative humidity (RH) is calculated from observed H_2O and temperature (T), with respect to liquid water for T > 0°C and with respect to ice for T < 0°C. The GV profiles of NO_x are the sum of measured NO and box modeled NO_2 at the time of observation. Since we are showing GV profiles obtained only during daylight conditions, the POLMIP NO_x profile (archived as monthly mean) has been scaled by the mean profile of ($[NO_{INST}]+[NO_{2\ INST}]$) / ($[NO_{24\,HR}]+[[NO_{2\ 24\,HR}]$) calculated from the box model simulations of the GV data. A profile of this ratio, which is close to unity is shown in the supplement. Error bars represent 1 standard deviation about the mean for 100 hPa pressure bins; they are offset slightly in the vertical for clarity. Some of the error bars are omitted to avoid clutter.

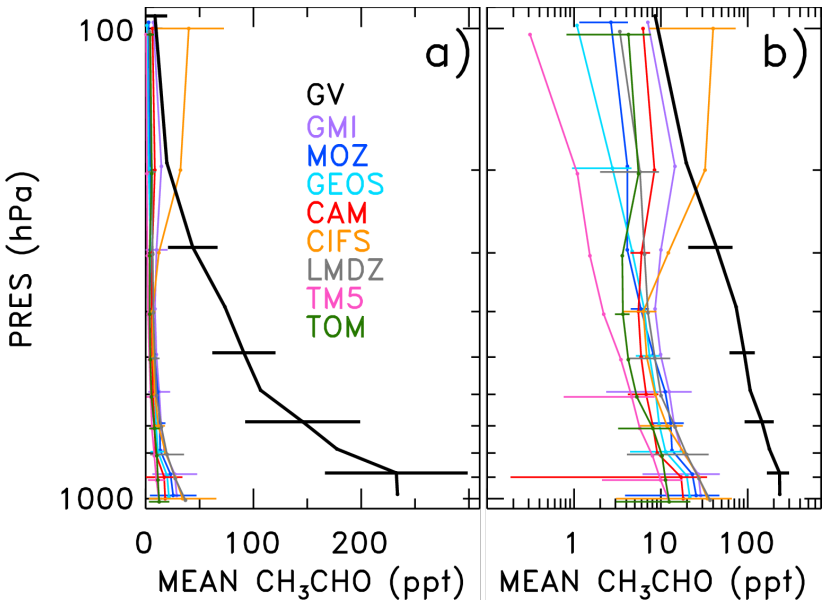

Figure 12. Same as Figure 8, except only showing monthly mean CH_3CHO values from individual POLMIP CTMs (colors) and from CONTRAST campaign (black) using a linear scale (panel a) and a log scale (panel b).

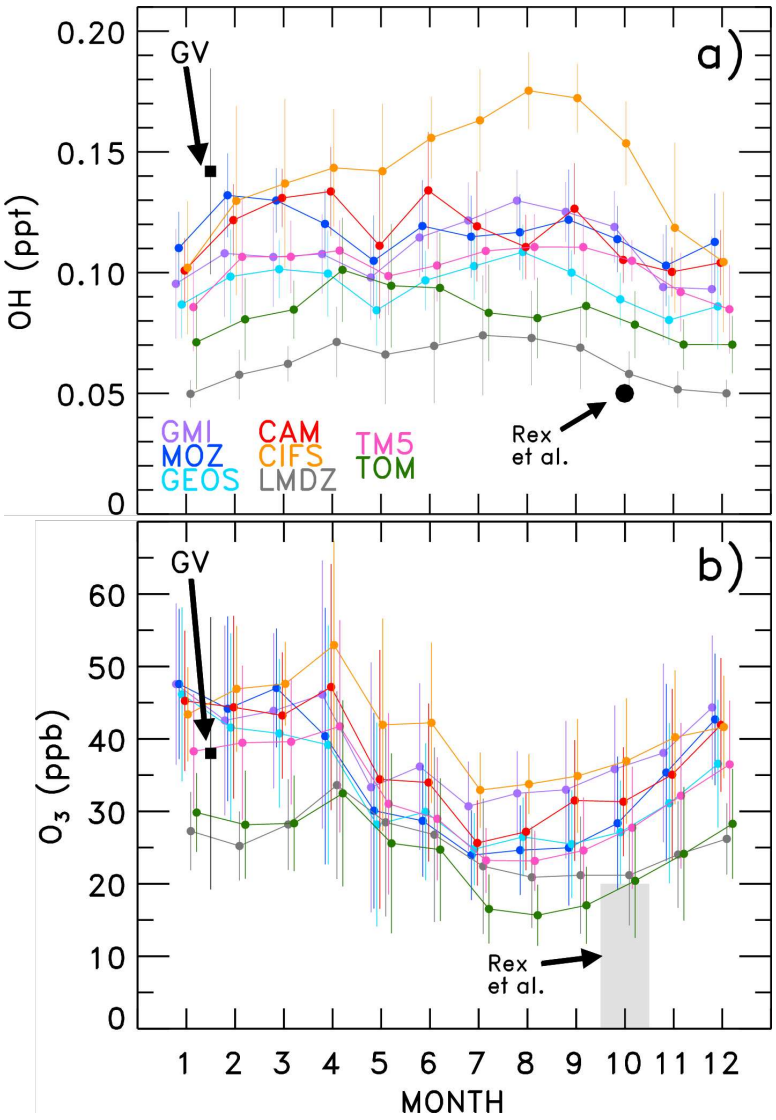

Figure 13. Seasonal variation of monthly mean OH mixing ratio (panel a) and O_3 mixing ratio (b) from the 8 POLMIP CTMs, for the pressure level closest to 500 hPa. The black squares show the mean and standard deviation of $OH_{24\ HR}$ (panel a) and O_3 (panel b) inferred from the CONTRAST GV observations of OH precursors, both at 500±50 hPa. The black circle shows $OH_{24\ HR}$ (a) at 500 hPa for October 2009 from Rex *et al.* [2014]. The grey box in panel b) shows the range of O_3 reported by *Rex et al*. [2014] in the TWP at 500 hPa for October 2009.

Journal of Geophysical Research – Atmospheres

Supporting Information for

An Observationally Constrained Evaluation of the Oxidative Capacity in the Tropical Western Pacific Troposphere

Julie M. Nicely[1,*], Daniel C. Anderson[1], Timothy P. Canty[1], Ross J. Salawitch[1], Glenn M. Wolfe[2,3], Eric C. Apel[4], Steve R. Arnold[5], Elliot L. Atlas[6], Nicola J. Blake[7], James F. Bresch[4], Teresa L. Campos[4], Russell R. Dickerson[1], Bryan Duncan[3], Louisa K. Emmons[4], Mathew J. Evans[8,9] , Rafael P. Fernandez[10,11], Johannes Flemming[12], Samuel R. Hall[4], Thomas F. Hanisco[3], Shawn B. Honomichl[4], Rebecca S. Hornbrook[4], Vincent Huijnen[13], Lisa Kaser[4], Douglas E. Kinnison[4], Jean-Francois Lamarque[4], Jingqiu Mao[14], Sarah A. Monks[5,**,***], Denise D. Montzka[4], Laura L. Pan[4], Daniel D. Riemer[6], Alfonso Saiz-Lopez[10], Stephen D. Steenrod[3,15], Meghan H. Stell[4,16], Simone Tilmes[4], Solene Turquety[17], Kirk Ullmann[4], Andrew J. Weinheimer[4]

1. University of Maryland, College Park, MD, USA.
2. University of Maryland Baltimore County, Baltimore, MD, USA.
3. NASA Goddard Space Flight Center, Atmospheric Chemistry and Dynamics Laboratory, Greenbelt, MD, USA.
4. National Center for Atmospheric Research, Boulder, CO, USA.
5. Institute for Climate and Atmospheric Science, University of Leeds, Leeds, UK.
6. University of Miami, Miami, FL, USA.
7. University of California, Irvine, CA, USA.
8. National Centre for Atmospheric Science, University of York, York, UK.
9. Department of Chemistry, University of York, York, UK.
10. Department of Atmospheric Chemistry and Climate, Institute of Physical Chemistry Rocasolano, CSIC, Madrid, Spain.
11. National Research Council (CONICET), Mendoza, Argentina.
12. European Centre for Medium-Range Weather Forecasts, Reading, UK.
13. Royal Netherlands Meteorological Institute, De Bilt, the Netherlands.
14. Princeton University, Princeton, NJ, USA.
15. Universities Space Research Association, Columbia, MD, USA.
16. Metropolitan State University of Denver, Denver, CO, USA.
17. Laboratoire de Météorologie Dynamique, IPSL, Sorbonne Universités, UPMC Univ Paris 06, Paris, France.

*now at: *NASA Goddard Space Flight Center, Atmospheric Chemistry and Dynamics Laboratory, Greenbelt, MD, USA.*
**now at: *Chemical Sciences Division, Earth System Research Laboratory, National Oceanic and Atmospheric Administration, Boulder, CO, USA.*
***now at: *Cooperative Institute for Research in Environmental Sciences, University of Colorado, Boulder, CO, USA*.

Contents of this file

Figures S1 to S14

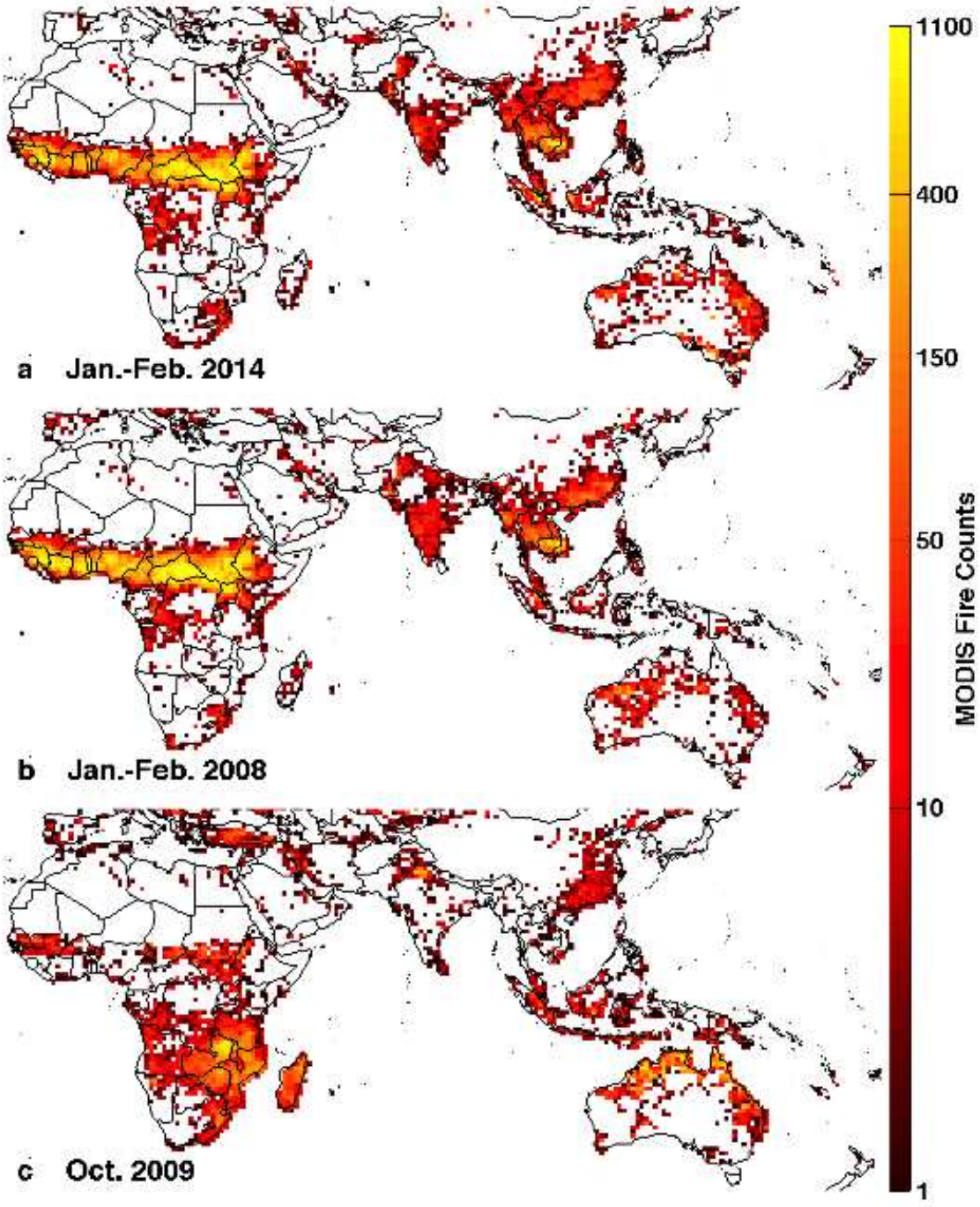

Figure S1. Total fire counts from MODIS in January and February for the years 2014 (panel a) and 2008 (b) and October for the year 2009 (c).

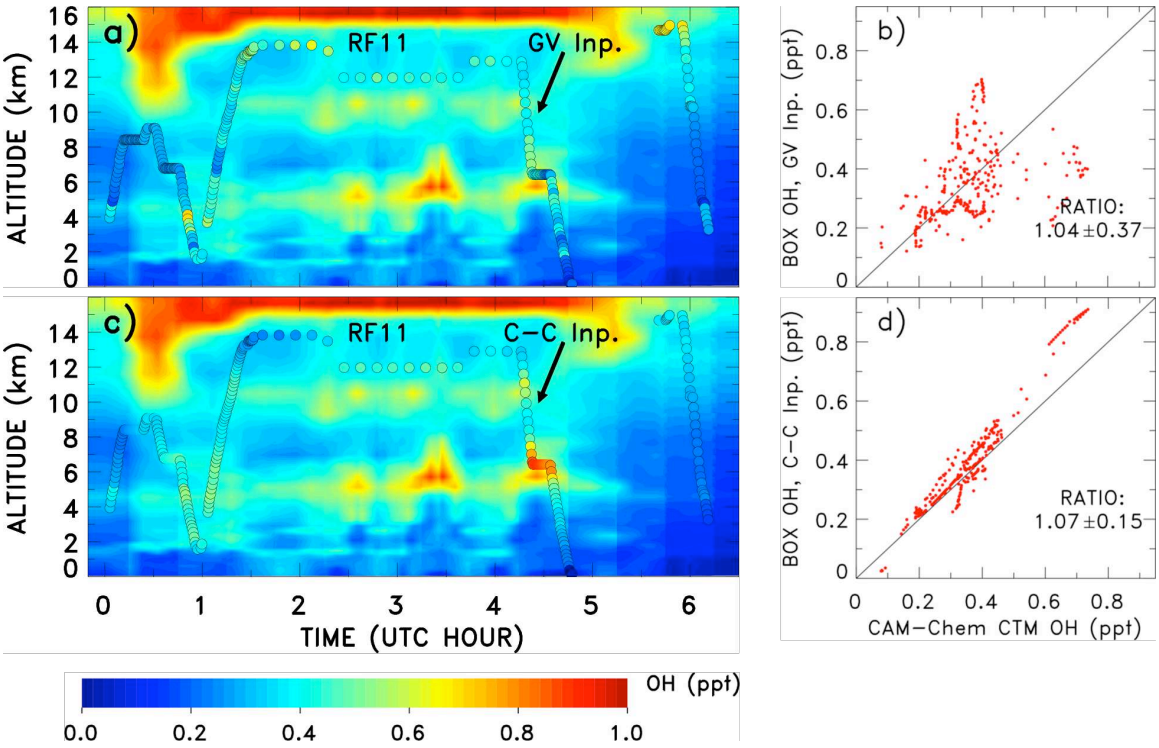

Figure S2. Same as Fig. 2, except for RF11 (13 February 2014). The r^2 for panel b) is 0.12 and the r^2 for panel d) is 0.93.

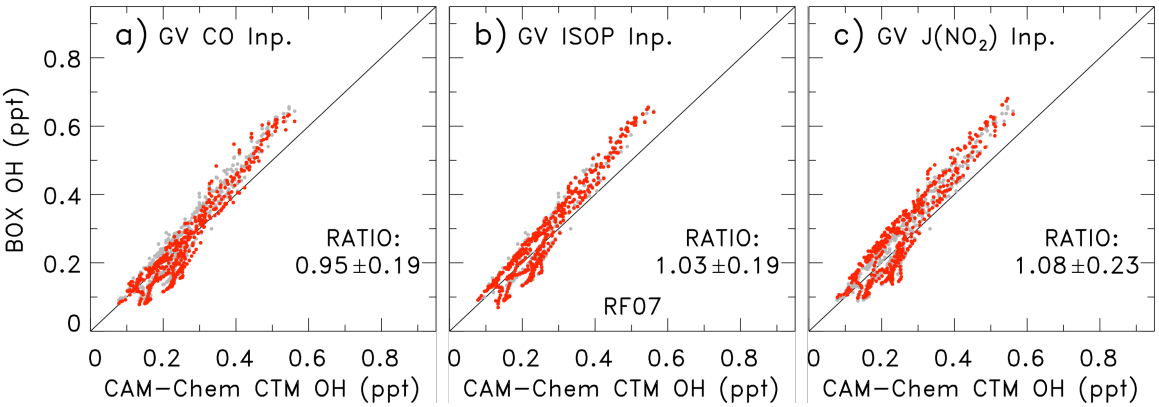

Figure S3. Same as Fig. 3 except variables used to constrain box model from CONTRAST measurements are CO (panel a), C_5H_8 (b), and $J(NO_2)$ (c).

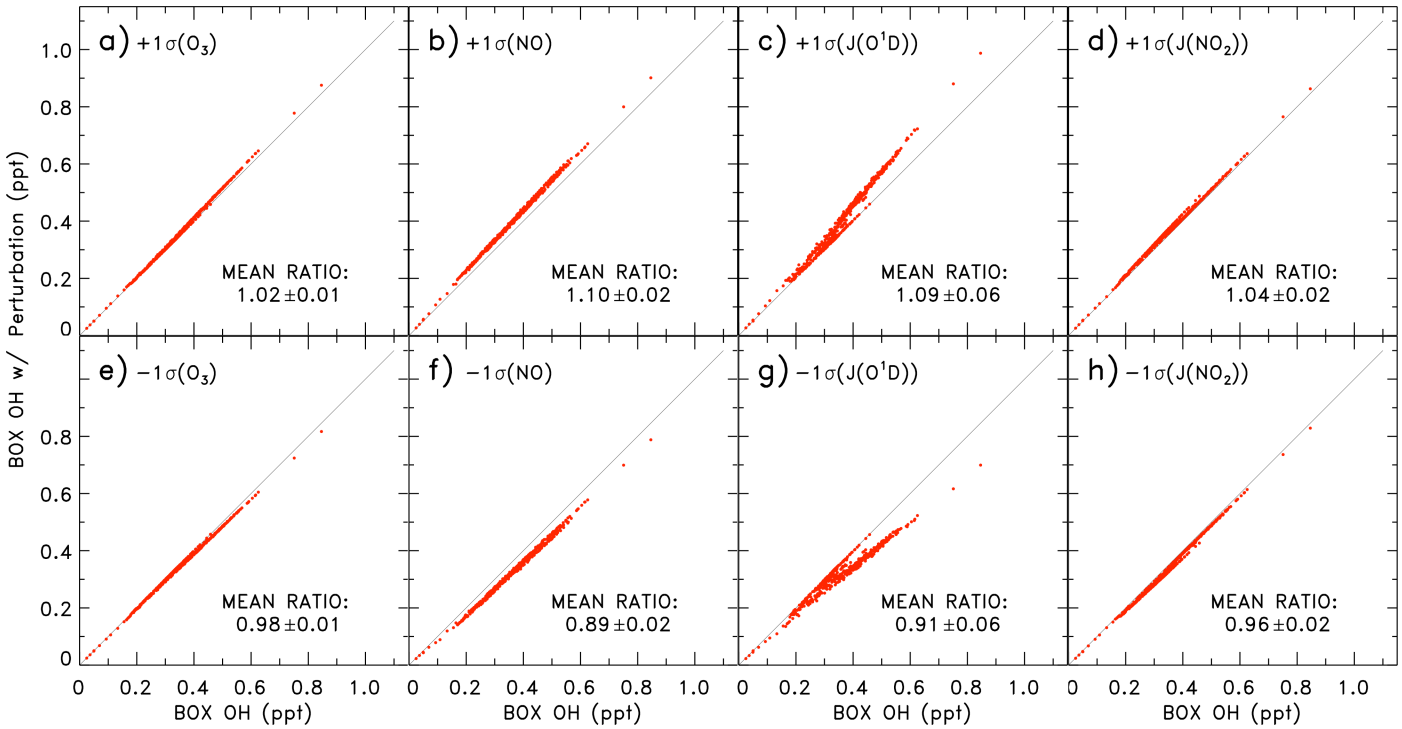

Figure S4. OH mixing ratios at the time of aircraft observation from sensitivity runs of the DSMACC box model constrained to CONTRAST GV observations, using measurement uncertainties to perturb a single variable in a positive (panels a, b, c, and d) or negative (panels e, f, g, and h) direction, versus OH from the base run of the box model constrained to GV observations for RF07. Panels a) and e) show 1σ perturbations applied to O_3, b) and f) show 1σ perturbations applied to NO, c) and g) show 1σ (±25%) perturbations applied to $J(O^1D)$, and d) and h) show 1σ (±12%) perturbations applied to $J(NO_2)$. The black line on the scatter plot is the 1:1 line. The mean ratio and standard deviation of $OH_{PERTURBED}$:OH_{BASE} is noted on each plot.

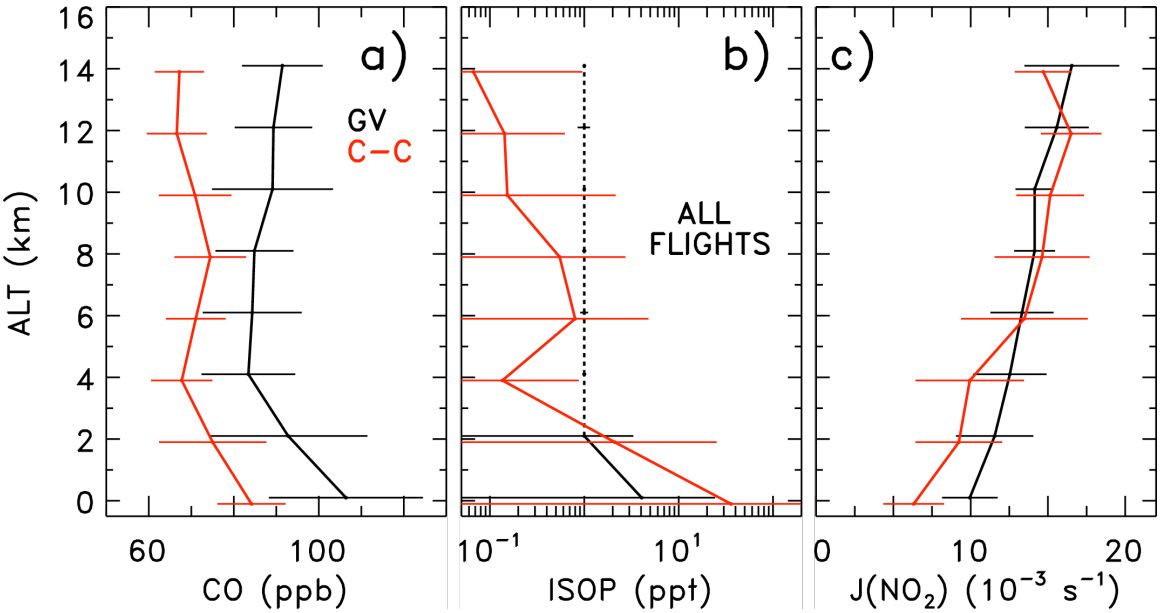

Figure S5. Same as Fig. 6 except for the variables CO (panel a), C_5H_8 (panel b), and $J(NO_2)$ (panel c). In the isoprene (ISOP) panel, the black dotted line depicts the instrument limit of detection (1 ppt) for altitude bins at which C_5H_8 remained below this threshold.

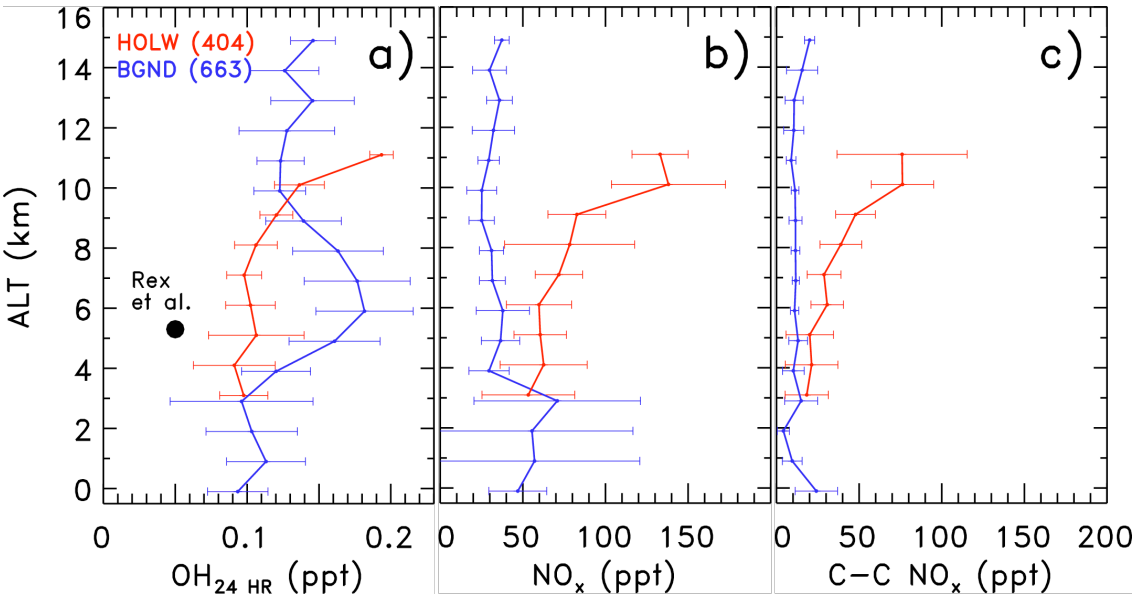

Figure S6. Profiles of $OH_{24\ HR}$ (panel a) and NO_x (panel b from GV and c from C-C) mixing ratios for all examined flights, separated by occurrence (red) and absence (blue) of high O_3/low H_2O (HOLW) structures. $OH_{24\ HR}$ is calculated by the DSMACC box model constrained to CONTRAST measurements within the same modeling domain as all of the prior figures, with the additional constraint that data are acquired either for background conditions (i.e. the low O_3, high H_2O mode) or for HOLW structures. NO_x is found using box model calculation of 24-hour average NO and NO_2 based on GV observations of NO, O_3, $J(NO_2)$, and hydrocarbons. Criteria for these two modes are O_3 < 25 ppb, RH > 70% (background) and O_3 > 40 ppb, RH < 20% (HOLW structure). Again, error bars represent 1 standard deviation about the mean of the respective $OH_{24\ HR}$ values within 1 km altitude bins and are offset slightly with respect to altitude for clarity. The parenthetical numbers represent the number of model simulations that went into each profile.

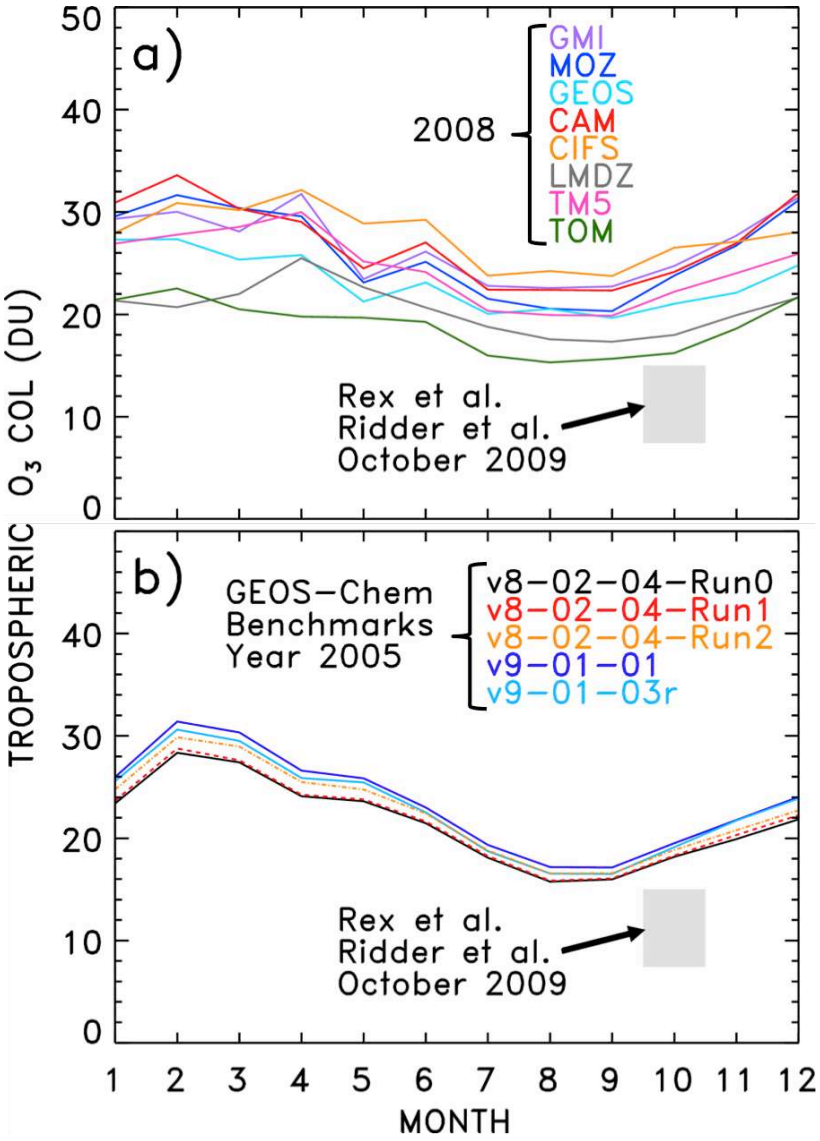

Figure S7. Tropospheric O_3 columns, calculated for each POLMIP CTM for the TWP region examined in this study (Fig. 1), plotted versus month. Panel a) shows tropospheric O_3 columns calculated for the 8 POLMIP CTMs for year 2008. Panel b) shows tropospheric O_3 columns calculated for 5 benchmark simulations from various versions of the GEOS-Chem model for year 2005. On both panels, the range of tropospheric O_3 column values shown in Rex et al. [2014] and Ridder et al. [2012], measured by ozonesonde during the TransBrom cruise in October 2009 and simulated by GEOS-Chem v8-02-04 for the same month and year, is highlighted by the shaded grey box. The chemical tropopause is found for each POLMIP model in panel a) using the relationship between O_3 and CO, following the method of *Pan et al.* [2012]; columns are integrated from the surface to the tropopause. The same tropopause pressures found for the POLMIP simulation of GEOS-Chem (v9-01-03) are used to calculate tropospheric columns from the benchmark runs of GEOS-Chem (panel b) for year 2005.

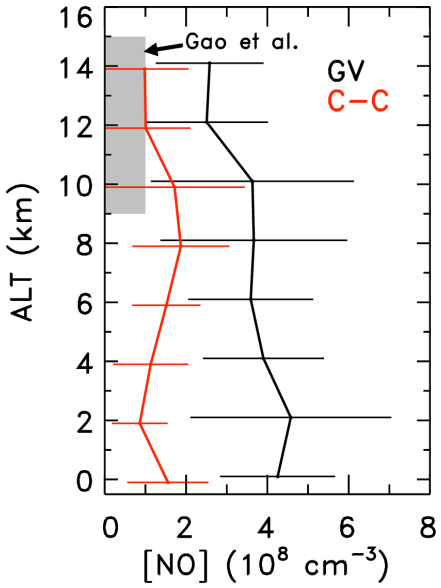

Figure S8. Profiles of [NO] averaged in 2 km altitude bins from all observations in the CONTRAST campaign, subject to the daytime TWP filter described in Methods (black line) and extracted from the CAM-Chem CTM for the times and locations of observation (red). The grey shaded region depicts the values of [NO] observed by *Gao et al.* [2014]. About 3.5% of measurements of [NO] made between 9 and 15 km during CONTRAST fall within the *Gao et al.* [2014] range.

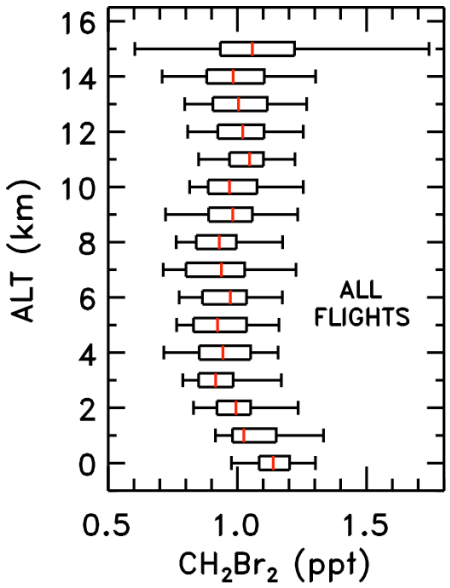

Figure S9. Vertical profile of CH_2Br_2 mixing ratio observations from the TOGA instrument for the entire CONTRAST campaign, subject to the time and location filter (sunlit conditions in the TWP) described in Section 2.1. Box and whiskers represent the 5th, 25th, 50th, 75th, and 95th percentiles, calculated within 1 km altitude bins.

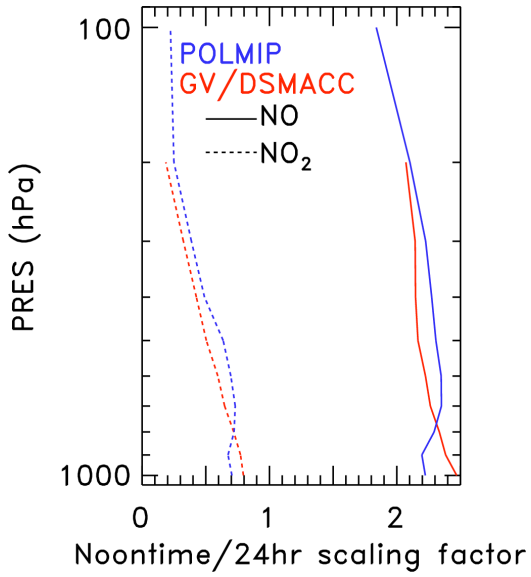

Figure S10. The scaling factors for NO and NO_2 used to convert monthly mean POLMIP mixing ratios of NO and NO_2 to mixing ratios representative of noon-time conditions, calculated from DSMACC box model results (red) and hourly POLMIP output (blue). The scaling factors calculated by the box model are applied in Figure 11c such that POLMIP values of NO_x can be directly compared with the daytime NO_x values, from NO observed during CONTRAST and NO_2 calculated by the box model; the NO scaling factor is also used in the POLMIP box modeling analysis, where POLMIP values of NO are input to the DSMACC box model initialized at local solar noon. Scaling factors are calculated for 100 hPa bins using the DSMACC box model, which simulates diurnally varying NO and NO_2. Scaling factors are calculated for NO and NO_2 as $(NO_{INST}) / (NO_{24\ HR})$ and $(NO_{2\ INST}) / (NO_{2\ 24\ HR})$, respectively, for all CONTRAST GV observations that meet the latitude/longitude filter discussed in the methods section and occurred within 1 hour of Guam local solar noon (2:00 UTC). The scaling factors calculated from POLMIP hourly output are derived from the 3 CTMs (CAM4-Chem, GMI, and LMDZ) that provided hourly output for the TWP region for April (neither January nor February hourly output was available) and are calculated as $(NO_{INST}) / (NO_{24\ HR})$ and $(NO_{2\ INST}) / (NO_{2\ 24\ HR})$, where NO_{INST} and $NO_{2\ INST}$ are the hourly means for 1:00, 2:00, and 3:00 UTC (local solar noon at Guam ±1 hour).

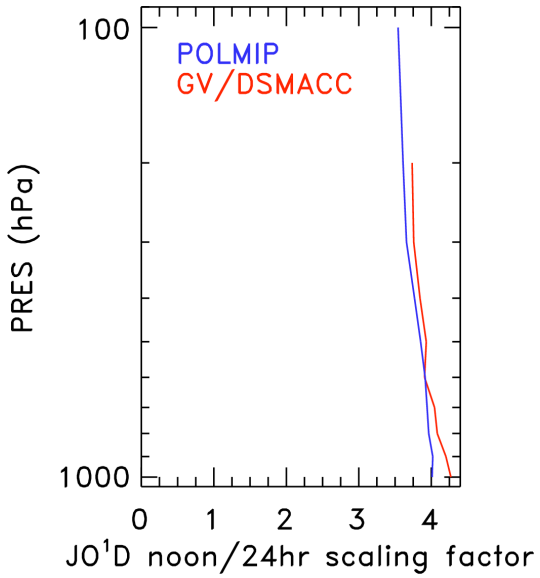

Figure S11. The scaling factors for $J(O^1D)$ used to convert monthly mean POLMIP values of $J(O^1D)$ to values representative of noon-time conditions, calculated from DSMACC box model results (red) and hourly POLMIP output (blue). The method for calculating these scaling factors follows the same method used for NO and NO_2 in Figure S10, except that the POLMIP value was calculated from hourly output only from POLMIP output of the CAM4-Chem model due to lack of availability of J-values from the other POLMIP models.

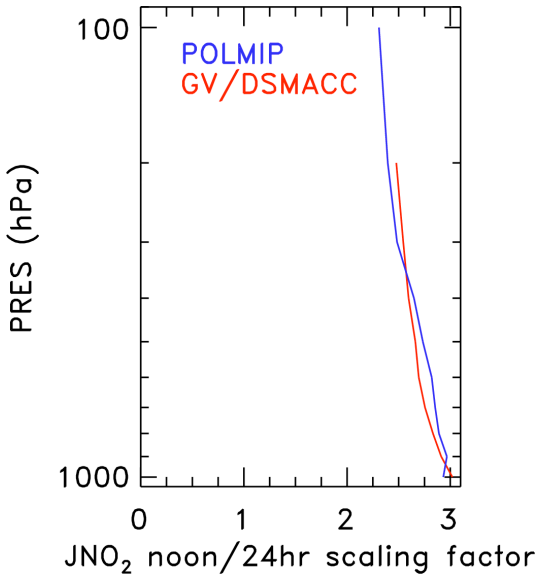

Figure S12. The scaling factors for J(NO_2) used to convert monthly mean POLMIP values of J(NO_2) to values representative of noon-time conditions, calculated from DSMACC box model results (red) and hourly POLMIP output (blue). The method for calculating these scaling factors follows the same method used for NO and NO_2 in Figure S10, except that the POLMIP value was calculated from hourly output only from POLMIP output of the CAM4-Chem model due to lack of availability of J-values from the other POLMIP models.

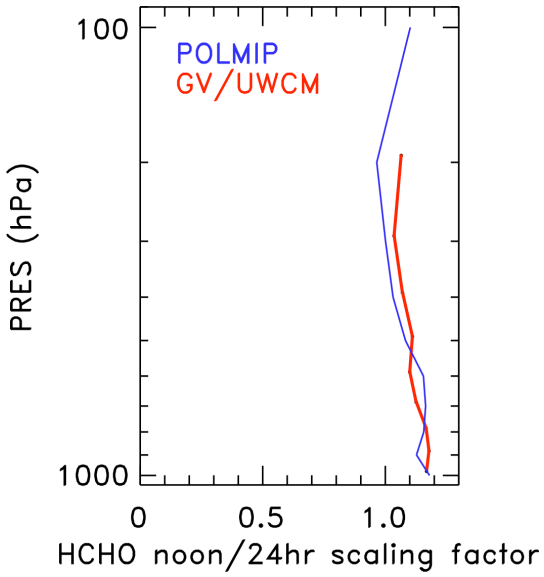

Figure S13. The scaling factor for HCHO used to convert observed mixing ratios of HCHO to mixing ratios representative of 24 hour average HCHO, calculated from GV observations and calculations by the UWCM box model (red) and from hourly output from the POLMIP CTMs (blue). The GV/UWCM scaling factors are applied in Figures 10e and 10j such that the HCHO measurements made during CONTRAST can be compared directly to the POLMIP monthly mean values of HCHO. Scaling factors are calculated for 100 hPa bins using the UWCM box model, which simulates diurnally varying HCHO. Scaling factors are calculated as ($HCHO_{INST}$) / ($HCHO_{24\ HR}$) for all CONTRAST GV observations that meet the latitude/longitude/SZA filter discussed in the methods section and fall within 2 hours of local solar noon. The same calculation is performed to derive the POLMIP scaling factors using the hourly output from CAM4-Chem, GMI, and LMDZ from April (January and February hourly output was unavailable).

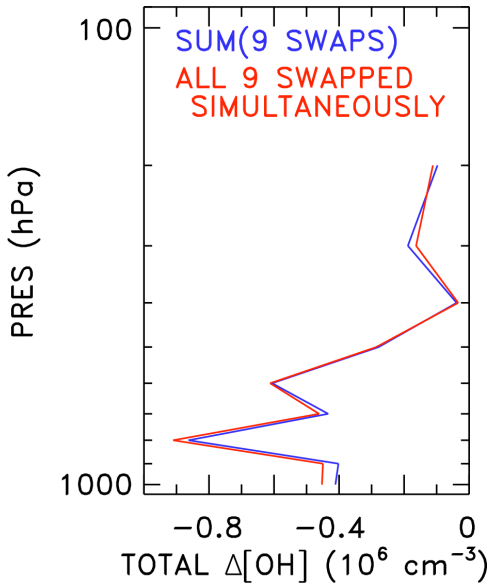

Figure S14. The total $\Delta[OH_{24\ HR}]$ from two sets of box model analyses of OH. The first is from nine separate runs of the DSMACC box model constrained to GV observations of all OH precursors except for the substitution, individually, of monthly mean POLMIP values of O_3, H_2O, NO_x, $J(O^1D)$, CO, C_5H_8, HCHO, $J(NO_2)$, and CH_3CHO. A difference in $[OH_{24\ HR}]$ is calculated between each of these runs and a base run of the DSMACC box model constrained only to GV observations of all OH precursors. The sum of these nine values of $\Delta[OH_{24\ HR}]$ are plotted (blue). The second box model analysis involves only one additional run of the DSMACC box model, where it is constrained to all nine species listed above simultaneously. A $\Delta[OH_{24\ HR}]$ is calculated between this run and the base run of the DSMACC box model constrained only to GV observations of OH precursors (red). Box model runs were conducted, and total $\Delta[OH_{24\ HR}]$ values calculated, at 100 hPa intervals.